In-Situ Diagnostics for Metalorganic Chemical Vapor Deposition of YBCO

Thesis by

Ashok Burton Tripathi

In Partial Fulfillment of the Requirements

for the Degree of

Doctor of Philosophy

California Institute of Technology

Pasadena, California

2001

(Submitted February 26, 2001)

Acknowledgments

This work was generously supported by DARPA/NSF grant DMS-9615858, and to a lesser extent by the US Air Force under contracts AFOSR-F549620-95-1-0419 and AFOSR-F549620-96-1-0471.

I would not have made it through Caltech, and this thesis would not exist without my advisor, Professor David Goodwin. Thank you for the virtually unending support, interest in and encouragement of my research, guidance, patience, and advice. I will forever be in your debt.

No one has contributed more actual content to this thesis than my good friend and colleague, Dr. David Boyd. Thank you for all of your efforts, insights, late nights, and long discussions. Of all my experiences at Caltech, I will miss our day to day interactions the most.

I would like to thank my officemate, collaborator, and friend Martha Gallivan for all of her exhaustive efforts in getting the reactor up and running. Especially worthy of mention is the work she did on the control software, heater assemblies, and thermal modeling of our reactor.

For teaching me all about CGS, oxygen diffusion, and how to navigate the traffic on the 110 freeway, I am deeply indebted to Dr. David Owen. Dave is always my best source of motivation, encouragement, and – when occasionally needed – sympathy.

Jurgen Musolf, of Superconductor Technologies Inc., provided the necessary materials, instructions, services, and support to make this project possible. Always ready and willing to help our cause, he has been a gracious stalwart in all of our efforts.

Professors Laxminarayan Raja and Bob Kee of the Colorado School of Mines lent their advice and assistance to all of the modeling phases of this reactor, and the gas chemistry considerations presented in Chapter 4 are based on their work.

For his help with our film characterizations, and input at all stages of this work, Professor Harry Atwater is greatly appreciated as are all the members of the Virtual Integrated Prototyping (VIP) project.

Professor Richard Murray helped keep our project organized and focused at the beginning, and helped keep me fed and clothed at the end. Thanks for all of the many forms of your support.

In addition, I need to thank Professor Rosakis for introducing CGS to our group, Professor Bhattacharya for his helpful discussions about phase transitions and stress analysis, and former undergraduates Sam Chung and Anna Iwaniec for the long hours and hard work they provided in our lab.

Professor Melany Hunt has been a supportive and helpful member of my advisory committee, and during my years as Residence Associate for Page House she was always involved and available in the lives of all Pages House residents, myself included, as our Faculty Associate.

Thanks also go out to Professor Marc Nicolet and his group who supplied access to and assistance with the RBS system, an integral part of our research results.

The people closest to me during the toughest part of writing this thesis have been my Grandparents, Charles and Rose Marie Evans, who quite literally put a roof over my head and food in my belly. Clearly there would be no thesis without my parents (there would be no me!). Thanks Mom, Dad, Margaret, and Wayne for helping me all along. I love you a lot. Always there when I need to move some furniture (even in the lab), my brother Dan is my best friend and closest ally.

Despite being last on this list, my beautiful wife, Iona Tripathi, is first and foremost in my heart, mind, and spirit. Having put up with me through it all, and surviving the past nine months that we've been apart, she will forever receive my love, thanks and adoration.

Abstract

A new stagnation flow MOCVD research reactor is described that is designed to serve as a testbed to develop tools for "intelligent" thin film deposition, such as *in-situ* sensors and diagnostics, control algorithms, and thin film growth models. The reactor is designed in particular for the deposition of epitaxial $YBa_2Cu_3O_{7-\delta}$ on MgO, although with minor modifications it would be suitable for deposition of any metal-oxide thin films.

The reactor is specifically designed to permit closed-loop thermal and stoichiometric control of the film growth process. Closed-loop control of precursor flow rates is accomplished by using ultraviolet absorption spectroscopy on each precursor line. Also integrated into the design is a Fourier Transform Infrared (FTIR) spectroscopy system which collects real-time, *in-situ* infrared polarized reflectance spectra of the film as it grows. Numerical simulation was used extensively to optimize the fluid dynamics and heat transfer to provide uniform fluxes to the substrate. As a result, thickness uniformity across the substrate is typically within 3% from the center to the edge of the substrate.

Experimental studies of thin films grown in the Y/Ba/Cu/O system have been carried out. The films have been characterized by Rutherford Backscattering Spectrometry and X-ray Diffraction. Results indicate c-axis oriented grains with pure 1:2:3 phase YBCO, good spatial uniformity, and a low degree of c-axis wobble. Experimental growth data is used in a gas phase and surface chemistry model to calculate sticking coefficients for yttrium oxide, barium oxide, and copper oxide on YBCO.

In-situ FTIR and Coherent Gradient Sensing (CGS) analysis of growing films has been performed, yielding accurate substrate temperature, film thickness monitoring, and full-field, real-time curvature maps of the films. In addition, we have implemented CGS to obtain full-field *in-situ* images of local curvature during oxygenation and deoxygenation of YBCO films. An analysis of the oxygen diffusion is performed, and diffusivity constants are presented for a variety of temperature and film conditions.

Contents

List of Tables

List of Figures

Chapter 1 Introduction

1.1 Background

Thin film deposition by metalorganic chemical vapor deposition (MOCVD) is an industrially important but complex process, involving the interplay of vapor-phase precursor transport and chemistry, surface reaction, and crystal growth. Largely due to the complexity of the process, the development of a new MOCVD reactor or process is done for the most part empirically through a long process of careful experimentation, prototyping, and testing. Numerical simulation is making inroads, however, and is already shortening development time by allowing optimization of reactor-scale flow and temperature distributions.

Closed-loop control has also begun to play an increasing role in CVD processes, as ever thinner films must be deposited uniformly over ever larger areas. This will require the development of inexpensive, robust *in-situ* sensors that can directly or indirectly monitor important film properties such as temperature, composition, thickness, and stress.

The combination of simulation, control, and *in-situ* sensors (known as "intelligent" thin film deposition) may enable new processes not currently possible, in which process parameters are varied continuously and deliberately during deposition to achieve specified film properties while minimizing some measure of cost (for example, total deposition time, or precursor consumption, or any other appropriate metric).

While the promise of intelligent thin film deposition is great, so are the challenges. A great deal of attention is now focusing on the modeling challenge of simulating processes across length scales. Of equal importance is experimental work to validate and test models of film growth and process control strategies and develop and validate suitable sensors.

In this thesis, we describe a research reactor designed to be a testbed for intelligent thin film deposition of epitaxial $YBa_2Cu_3O_{7-\delta}$ (YBCO) on single crystal MgO (001) substrates. This material system is of interest for the development of compact, high-performance microwave filters using superconducting passive resonators [105].

1.1.1 High Temperature Superconductors (YBCO)

Superconductivity, the presence of zero electrical resistance[1], was discovered in 1911 by H. K. Onnes [109] in mercury at a temperature of 4 K. This temperature, T_c, is known as the critical or transition temperature for superconductors. For the next 75 years, a variety of niobium compounds pushed the T_c as high as 23.3 K [53, 140]. In 1986, at IBM research labs in Zurich, Bednorz and Müller shocked the world with an entirely new class of superconductors [10]. They discovered the Ba-La-Cu-O system and $BaLa_4Cu_5O_5$ in particular with a T_c of 30 K. A few months later, in early 1987, Wu and Chu *et al.* discovered $YBa_2Cu_3O_7$ which has a transition temperature of up to 93 K [167, 62]. YBCO changed the realm of applications for superconductivity because it raised the critical temperature above the boiling point of liquid nitrogen, a substance readily available throughout the world.

The atomic structure of YBCO is illustrated in Figure 1.1. The copper-oxide planes are shown with chemical bonds to illustrate the charge carriers which are believed to be the source of the superconductivity [73]. The unit cell and lattice spacings are depicted in Figure 1.2.

YBCO is manufactured in bulk via a sintering and annealing process; however, YBCO has more potential applications in the form-factor of a thin film. Our partners

---

[1] A superconductor, by definition, has at least 10^{17} times less resistance than copper at room temperature [94].

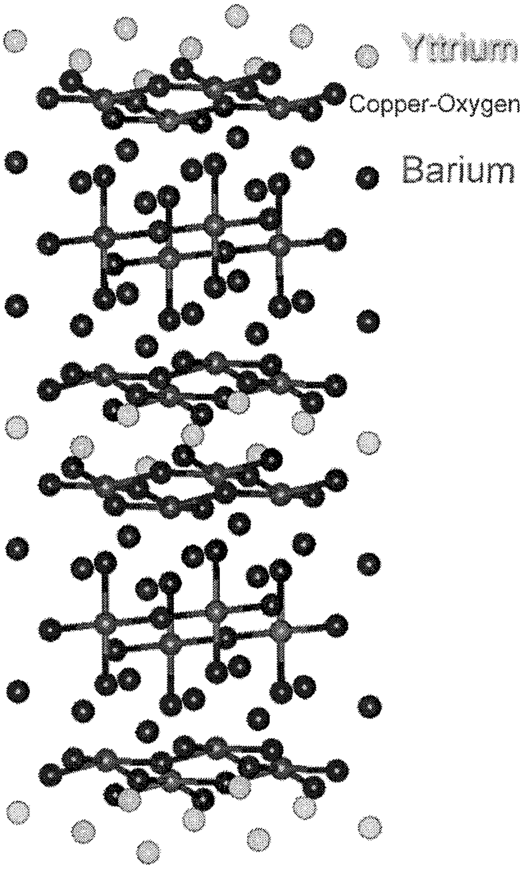

Figure 1.1: Atomic representation of $YBa_2Cu_3O_7$. The plane of atoms at the bottom, top and center of the structure is the yttrium, while all of the copper atoms are shown bonded to neighboring oxygen atoms.

at Superconductor Technologies Inc. (STI) construct passive microwave filters using YBCO thin films [105]. Other potential applications include interconnects for microelectronics, superconducting quantum interference devices (SQUIDS), and Josephson devices [91]. SQUIDS, manufactured from YBCO thin films, are capable of detecting extremely small magnetic fields and have potential applications in medicine and computers.

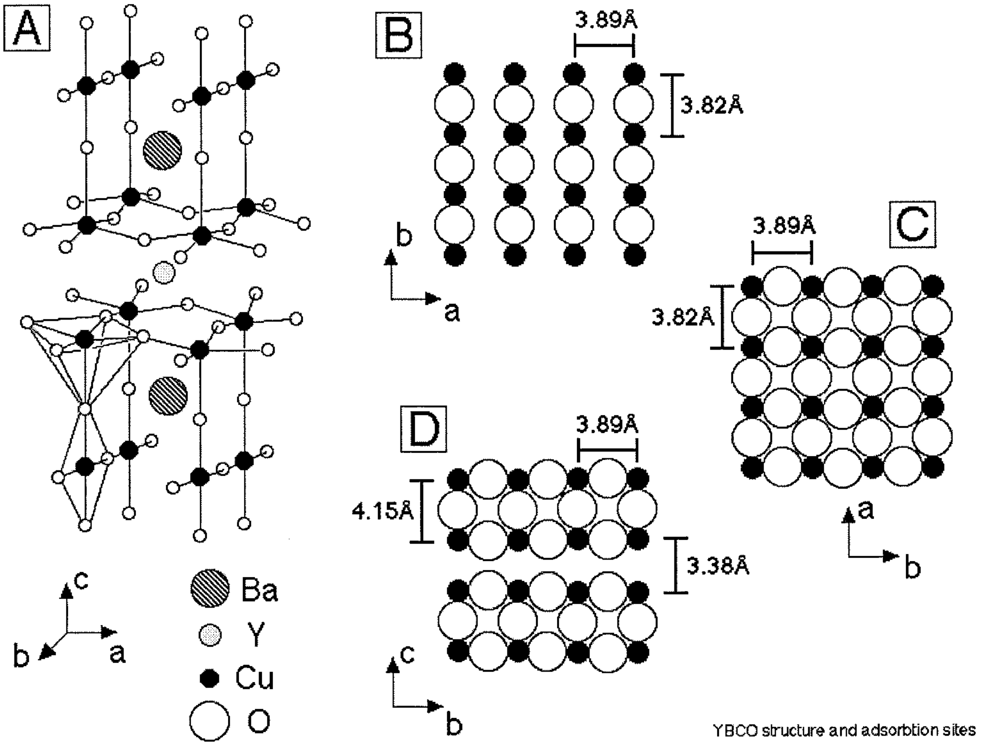

Figure 1.2: YBCO lattice spacing and orientation.

1.1.2 Chemical Vapor Deposition of YBCO

Most high temperature superconducting thin films are grown using physical vapor deposition (PVD) techniques such as electron beam evaporation [3, 87], sputtering [64, 127], laser ablation [35, 117], and molecular beam epitaxy [84, 164]. Unlike PVD techniques, CVD does not require high vacuum or line-of-sight access to the substrate, which translates to high growth rates and the ability to coat large areas and complex shapes [32]. CVD is also highly adaptable to a wide range of oxygen partial pressures [171] and is capable of scaling to even larger deposition areas [142].

MOCVD of YBCO was first demonstrated at the Naval Research Laboratories by Berry *et al.* in early 1988 [11] followed later that year by Dickinson *et al.* at Stanford [34]. By 1993 over 39 research groups from around the world were producing YBCO using CVD techniques [91]. Nonetheless, *in-situ* diagnostics and closed-loop thermal and stoichiometric control are quite rare. Most CVD systems are based on off-the-shelf reactors which have been modified for use with YBCO precursors. Many are hot wall, vertical-flow reactors which are incapable of optical access to the growing film [91] due to the requirement that all surfaces be maintained at the growth temperature.

Our reactor is a stagnation flow design [28, 50]. This choice was made to allow optical access for sensors and diagnostics and to promote uniform thickness film deposition [72]. Two-dimensional axisymmetric reacting-flow simulations were used to optimize the reactor dimensions and gas flowrates to give a uniform thickness boundary layer above the substrate [75].

The need for optical ports and our desire to vary the deposition temperature during a run precluded a hot wall design; accordingly the reactor is "warm wall" — the walls are maintained with a circulating oil bath at a temperature just sufficient to keep precursor material from condensing on the walls. This warm wall design enables the unique application of two valuable *in-situ* diagnostic techniques, Fourier transform infrared (FTIR) spectroscopy and coherent gradient sensing (CGS).

In-situ diagnostics are of great interest due to the ever increasing wafer size, and ever decreasing feature size of semiconductor electronics. For many years, high vacuum techniques have enjoyed the advantage of in-situ diagnostics such as RHEED to determine substrate surface conditions and measure growth rates [143]. Although limited, a few optical techniques have begun to show promise [5]. Specifically, optical reflectance [141], ellipsometry [114], and emission spectrometry [57] have been used to measure growth rate [141], wafer temperature [57], and sample composition [114]. However, the last two results require suitable calibration for a given material system.

FTIR, in particular, has been used extensively to investigate CVD processes *in-situ.* For example, Kobayashi *et al.* have used FTIR to study CVD growth of tungsten [81], and many groups have used FTIR as an *in-situ* diagnostic for CVD of silicon [13, 104, 147]. Our implementation of FTIR is consistent with other *in-situ* research efforts, and appears to be the first use of FTIR to study the growth of YBCO. Most uses FTIR involve analysis of chemical bond energies, shedding light on surface chemistry and composition. In contrast, our use of infrared spectrometry permits real-time feedback of substrate temperature and film thickness information.

1.1.3 Coherent Gradient Sensing

A material configuration of central importance in microelectronics is a thin film of one material deposited onto a substrate. Fabrication of such a structure inevitably gives rise to stress in the film due to lattice mismatch, differing coefficients of thermal expansion, chemical reactions, or other physical effects [89].

Current experimental techniques for measuring stresses are based on either direct measurements of lattice distortion using X-ray Diffraction (XRD) [31, 157] or on the measurements of substrate curvature or deflection [44, 108]. XRD analysis involves repeated measurements of the lattice spacings in a crystalline material [31] to evaluate stress and strain. XRD is difficult or impossible to use *in-situ*, and moreover, the method is strictly point-wise; full-field instantaneous measurement of film stress is not possible.

Curvature measurement techniques include XRD rocking curve analysis, laser scanning, and interferometric techniques [45, 46, 47]. XRD rocking curve analysis involves the same limitations listed above. Laser scanning is the most commonly used technique for measuring curvature changes of the substrate. Although very sensitive, laser scanning is also point-wise [44]. While raster scanning is possible for full-field measurements, it involves considerable complexity and cost, and because of the time based requirements, it is not appropriate for transient non-uniform phenomena.

Techniques based on optical interferometry offer much promise as a means for real-time, remote, high resolution, full-field measurements of curvature and curvature changes. However, standard interferometric techniques (*e.g.,* Twyman-Green interferometer) [15, 59] are sensitive to rigid body rotation and displacement of the specimen surface and thus are very vibration sensitive. Because these interferometric techniques measure the surface topography, two successive differentiations of the experimental data are required to obtain curvature. The results often include unacceptable error levels, which limit the usefulness of traditional interferometric techniques for accurate stress measurement in thin films.

A new interferometric technique, coherent gradient sensing (CGS), has been developed at Caltech by Rosakis *et al.* [120, 121] to measure the entire curvature tensor fields in thin film and micromechanical structures. The CGS technique offers significant advantages over other currently used curvature measurement techniques. These advantages include rigid body motion insensitivity (and the associated vibration insensitivity), accurate and full-field measurement of all components of the curvature tensor, as well as *in-situ* and real-time capabilities. In Chapter 5, we will present the first application of CGS to a thin film deposition chamber for *in-situ,* real-time analyses.

Although laser diagnostic techniques for CVD have existed for many years in the form of Raman spectroscopy [18, 61] and laser induced fluorescence (LIF) [4, 95, 126], these are used almost exclusively for gas phase measurements. In the rare instance where laser diagnostics are applied to thin films, they are not capable of measuring stress. Through the use of CGS, our facility has the first *in-situ* diagnostic capable of real-time film stress analysis, for any CVD system.

1.2 Chapter Outline

Chapter 2 presents a full description of the MOCVD facility constructed at Caltech as a part of this research project. In addition to disclosure of the operating hardware, the design of many of the individual components is presented in detail. Numerous design calculations are reported including flow analysis of the showerhead, thermal analyses of several components, and an analysis of precursor absorbance for stoichiometry control.

Chapter 3 provides procedural details concerning thin film growth of YBCO by MOCVD. In addition to specific operational instructions, Chapter 3 also provides an account of the film characterization experiments carried out on our thin films which include x-ray diffraction, Rutherford backscattering spectrometry, and energy dispersive x-ray analysis.

Chapter 4 details the results gathered from operation of the MOCVD reactor. Film growth results are detailed along with additional film analyses by x-ray photoelectron spectrometry and electron microprobe analysis. Reactor characterizations are presented including film uniformity, temperature calibration, and gas composition evaluations. Contributions of the growth results to CVD modeling efforts are also discussed at length.

Chapter 5 expounds on the application of coherent gradient sensing to our MOCVD reactor. The theory of operation for CGS is explored, and experimental results are provided. Along with film growth investigations, thermal processing results are presented which illustrate the stress effects of a phase transition in the YBCO system. Stress analyses of the YBCO films are presented for heating and cooling of the film/substrate at different operating conditions.

Chapter 6 describes our investigations into oxygen diffusion in YBCO thin films. CGS is utilized to measure the relaxation time constant as oxygen concentrations are changed in the gas and film. In addition to a detailed analysis of diffusion theory, oxygen diffusion constants are presented for a variety of experimental conditions. Ultraviolet spectrometry of YBCO thin films, which provides further insight into the oxygen concentration, is also presented in this chapter.

Chapter 7 offers concluding remarks and possibilities for future research. Appendix A is a list of often used abbreviations. Appendix B details the design of the showerhead oven, including thermal calculations and computer aided drafting (CAD) drawings. Appendix C contains additional CAD drawings of the reactor body and showerhead. Finally, Appendix D presents the raw CGS data from Chapter 6 (oxygen diffusion experiments) in graphical form.

Chapter 2 Experimental Apparatus

Design and construction of our chemical vapor deposition system began in the summer of 1997, reaching a rough operational status in the spring of 1999. Due to the inherent nature of such a complex experimental system, the reactor is never truly complete. Even to this day, modifications and adaptations are being made.

Final design of each component involved many levels of concept prototyping, modeling, and analysis. The following chapter discusses the challenges, compromises, and process whereby the final system design was arrived upon, as well as the lessons learned during the construction and operation of this CVD reactor.

2.1 The Gas Handling System

In order to supply the requisite metalorganic species to the film in a vapor phase (hence the V in CVD), a gas handling system was designed and constructed around the constraints of these materials. Schematically, the gas handling system is represented in Figure 2.1. Our discussion roughly follows the path of these precursors from source to thin film.

2.1.1 Bubblers

Small stainless steel ball bearings (5mm diameter) are coated with the organometallic powder of each precursor. Details of the precursor materials, $Ba(tmhd)_2$, $Cu(tmhd)_2$, and $Y(tmhd)_3$, are discussed in Chapter 3. The coated ball bearings are then poured into a "bubbler," Figure 2.2. Our design is similar to that of many CVD systems.

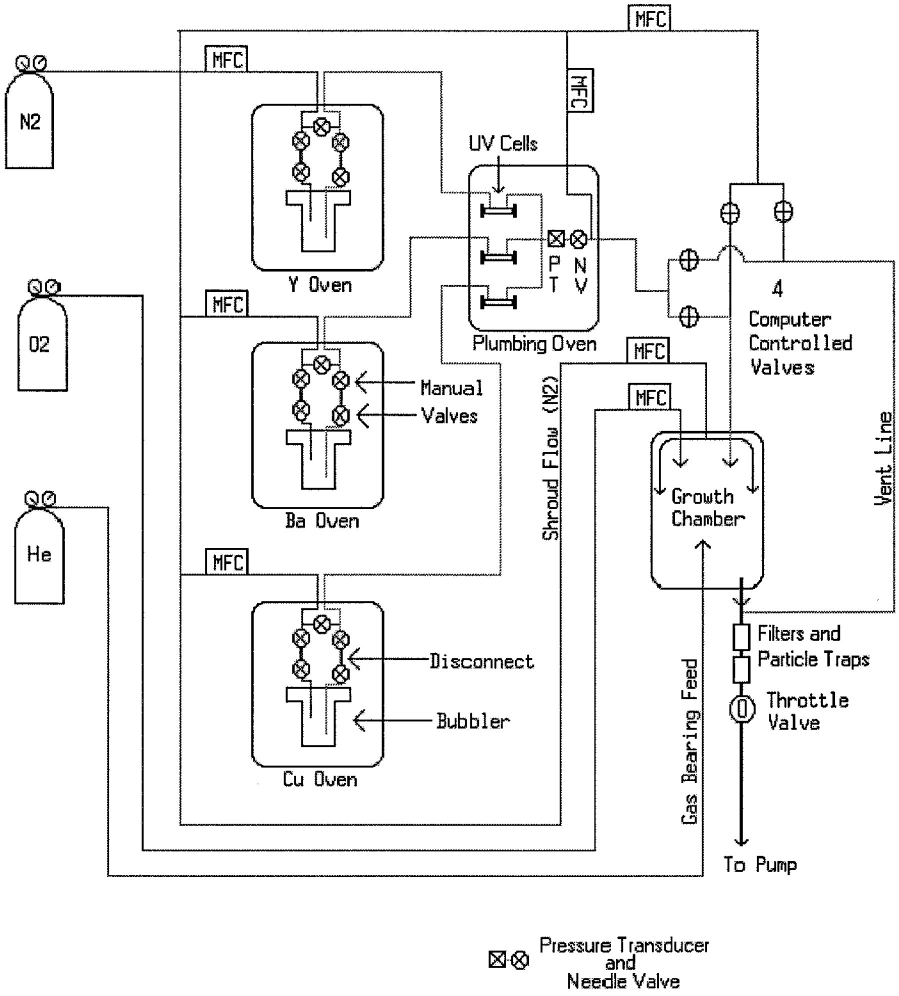

Figure 2.1: A schematic diagrom of the gas handling system.

A cylindrical canister (5 in depth, 1.75 in diameter) is topped by a 3 3/8 in Conflat vacuum flange. The lid includes a gas inlet tube that extends down 4.69 in. A second 3 in long, sealed tube houses a thermocouple probe for accurate measurement of the precursor temperature. Also on the lid is a large outlet port for evaporated precursors. Because of the different temperature regimes of each precursor and in order to accurately control film stoichiometry, each material has its own bubbler.

In order to prevent clogging of the gas lines with condensed or decomposed precursor, all lines carrying precursors are constructed of 1/2 in diameter stainless steel

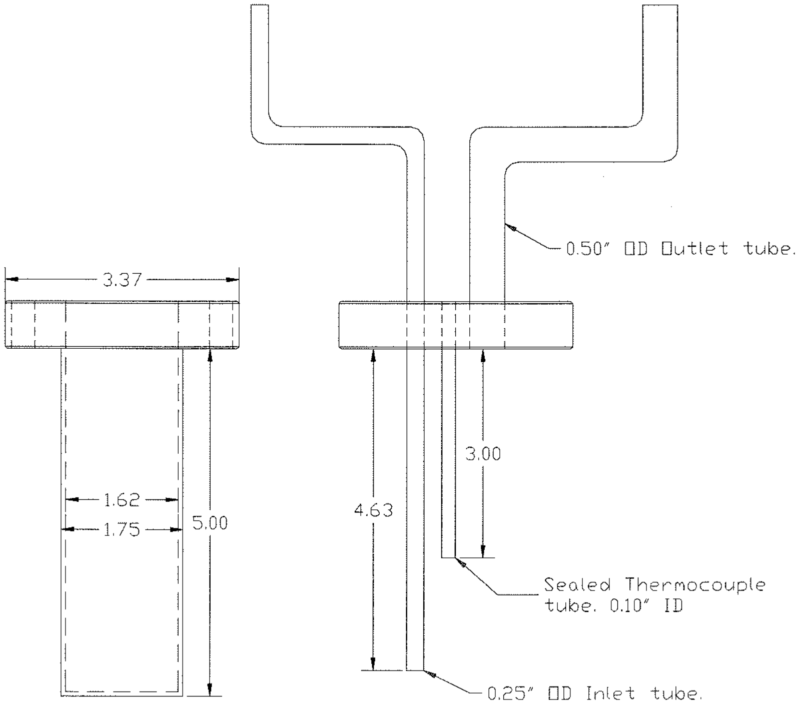

Figure 2.2: Schematic drawing of the bubbler depicts the canister and lid assembly.

tubing. Gas lines which carry pure oxygen, nitrogen, argon, and helium are made of 1/4 in stainless steel tubing.

Flow rates are metered by a bank of MKS mass flow controllers (type 1259, 10 slm full range), all of which are connected to a Pentium class data acquisition PC running *Sparrow* laboratory control software which was developed at Caltech by Professor Richard Murray. All tubing connections are made with VCR brand vacuum fittings welded directly to the tubes.

Each bubbler is flanked by 4 manual valves which serve three purposes. They control the flow of the carrier gas (either sending it through the bubbler or through a separate bypass line); they allow the bubbler to be closed off and isolated from the rest of the system; and they allow the gas system to be sealed off when the bubbler

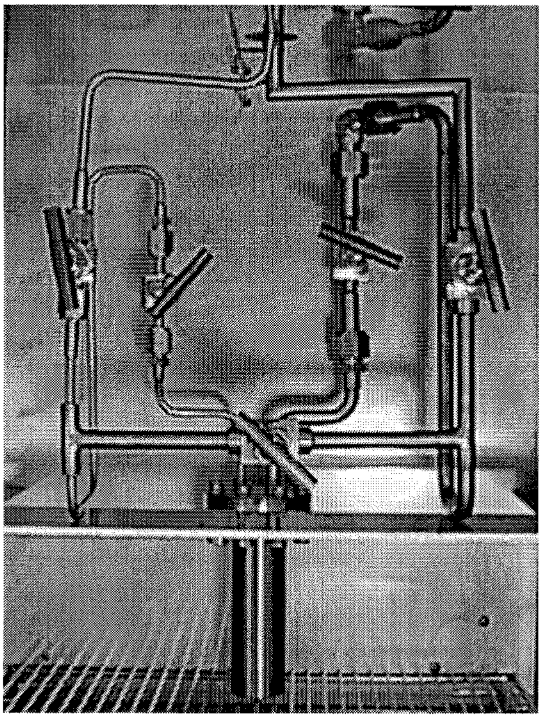

Figure 2.3: Photograph of one of the bubblers containing metalorganic precursors; also visible are the 4 flow control valves.

is removed for cleaning and filling. All 4 valves and a bubbler are present inside a bubbler-oven as shown in Figure 2.3.

In order to optimize sublimation of the precursors, each bubbler is housed in a separate oven. Oven temperatures are set manually, but monitored through the use of thermocouples placed in the lid of the bubblers.

2.1.2 Thermal Regulation

Once the carrier gas contains organometallic species, it must be maintained at a temperature above that of the bubbler ovens, so as to prevent re-condensation of the precursors. On the other hand, the precursors can not be exposed to temperatures above 300 °C, or they will begin to decompose [23, 21]. The requisite thermal regulation is accomplished in three ways.

As the metal-organic species leave the bubbler ovens they enter heated lines. The tubes are encased in silicone rubber insulation jackets within which are resistive electrical heat tapes and J type thermocouples. The thermocouples act as sensors for two Watlow PID (proportional, integral, and differential) based controllers. These heated lines bring the carrier gases and precursors into a plumbing oven, which is the second method of maintaining proper temperature.

The plumbing oven is a Fisher Scientific ISOTEMP laboratory oven which has been modified to house all the valves, switching gear, manifolds, and plenums which are required to route the gas flows appropriately.

Inside the plumbing oven each metal species goes through an optical cell. Three distinct optical cells are required due to the overlapping nature of the ultraviolet absorption peaks of barium, yttrium, and copper tmhd's [33]. From the cells, the three gas streams combine inside a plenum, at which point the pressure is measured using an MKS Baratron type 121A capacitance manometer. This pressure signal is also fed into the data acquisition PC, and is used in calculating the total flowrates of each precursor.

The plumbing oven also contains four pneumatic computer controlled valves which allows the operator to switch the reactor from "Run" to "Vent" mode, Figure 2.4. While in Vent mode, the reactive precursors are sent to a vent line which bypasses the reactor and a "dummy" flow of nitrogen is sent through the reactor to stabilize the flow patterns and bring the reactor into a steady state condition. Run mode switches the flows so that the reactive metal species go directly into the reactor, and the dummy flow exits through the vent line. In case of emergency, a toggle switch has been installed which allows the operator to redirect all flow to the vent line [1].

---

[1] One example where the emergency switch proved useful was when one of the chamber windows imploded during a growth run. By re-routing all reactant flows to the vent line, we were able to prevent potentially harmful gases from escaping into the lab.

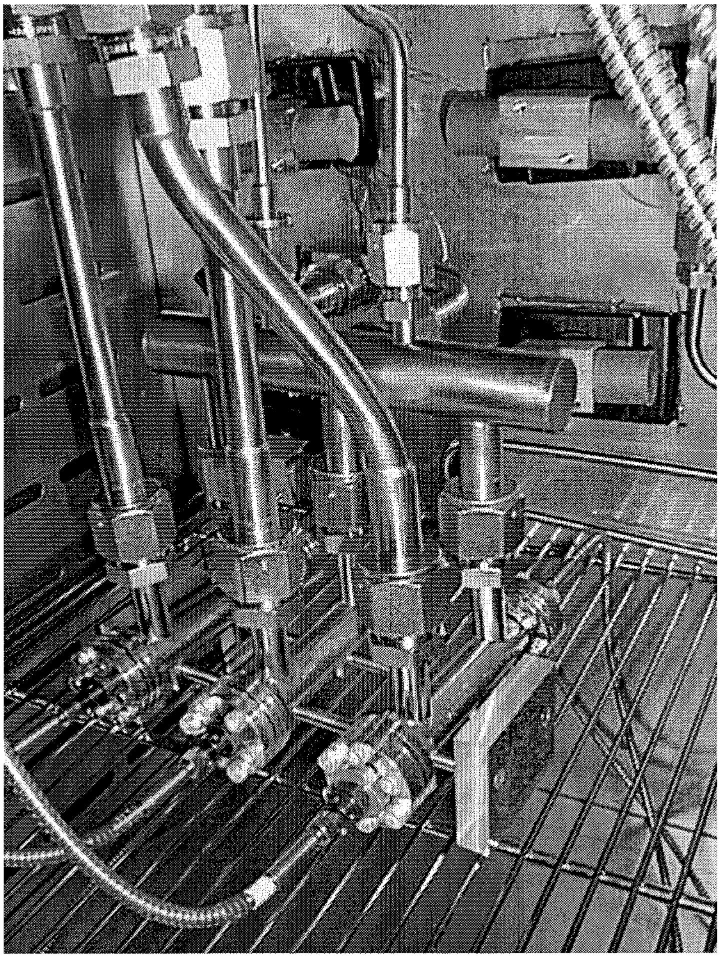

Figure 2.4: Photograph illustrating the three optical cells for UV spectroscopy and four pneumatic vavles (not connected) for Run-Vent selection (see text for further description).

The oxygen flow, when present, always travels directly into the reactor. As such, the plumbing oven contains three long 1/4 in tubes which serve to heat the oxygen, the remaining bulk nitrogen flow, and the dummy nitrogen flow. The tube length was calculated using fully developed, laminar tube flow theory [165], with constant wall temperature equal to that of the plumbing oven ($T_w = 250\,^{\circ}\mathrm{C}$). To be certain of laminar flow, we require a Reynold's number based on diameter, Re_D, to be less than 2000. In our case,

$$\mathrm{Re}_D = \frac{\rho \overline{u} D}{\mu} = 1643 \;, \tag{2.1}$$

where D is the inner tube diameter, 0.18 in, gas velocity, $\overline{u}$, can be calculated from the a maximum flowrate of 10 slm (where slm represents Standard Liters per Minute) to be 308 m / s, density is $\rho = 0.028\,\mathrm{kg}\,/\,\mathrm{m}^3$ for nitrogen, and viscosity, $\mu = 2.4 \times 10^{-5} \frac{\mathrm{kg}}{\mathrm{m\,s}}$, is for the operating pressure in the lines of 25 torr.

For fully developed laminar tube flow with a constant wall temperature we know from [1] that the Nusselt number is

$$Nu_D = \frac{hD}{k} = 3.66 \;, \tag{2.2}$$

where h is the heat transfer coefficient and $k = 0.038 \frac{\mathrm{W}}{\mathrm{m\,K}}$ is the thermal conductivity of the gas. From [165] we find the following relation for gas temperature at the outlet of the tube,

$$T_{out} = T_w + (T_{inlet} - T_w) * e^{-\frac{\pi D}{\dot{m} C_p} \int_0^L h \cdot dx} \;, \tag{2.3}$$

where $\dot{m} = 2.08 \times 10^{-4} \frac{\mathrm{kg}}{\mathrm{s}}$ is the mass flow rate of nitrogen and $C_p = 1050 \frac{\mathrm{J}}{\mathrm{kg\,K}}$ is the specific heat of nitrogen. Thermally, the gases must reach a sufficient temperature to not permit the recondensation of the barium precursor. Because the barium bubbler oven operates at 240 °C, we require the gases to reach this temperature at the outlet of the tube (i.e. $T_{out} = 240\,^\circ\mathrm{C}$). Integrating, and solving for L yields

$$L = \frac{\dot{m}\; Cp}{3.66 \pi k} \ln \left[\frac{T_i - T_w}{T_o - T_w} \right] = 1.6\,\mathrm{m} \;. \tag{2.4}$$

With an allowance of 0.4 m for the flow to fully develop, heating tubes 2 meters

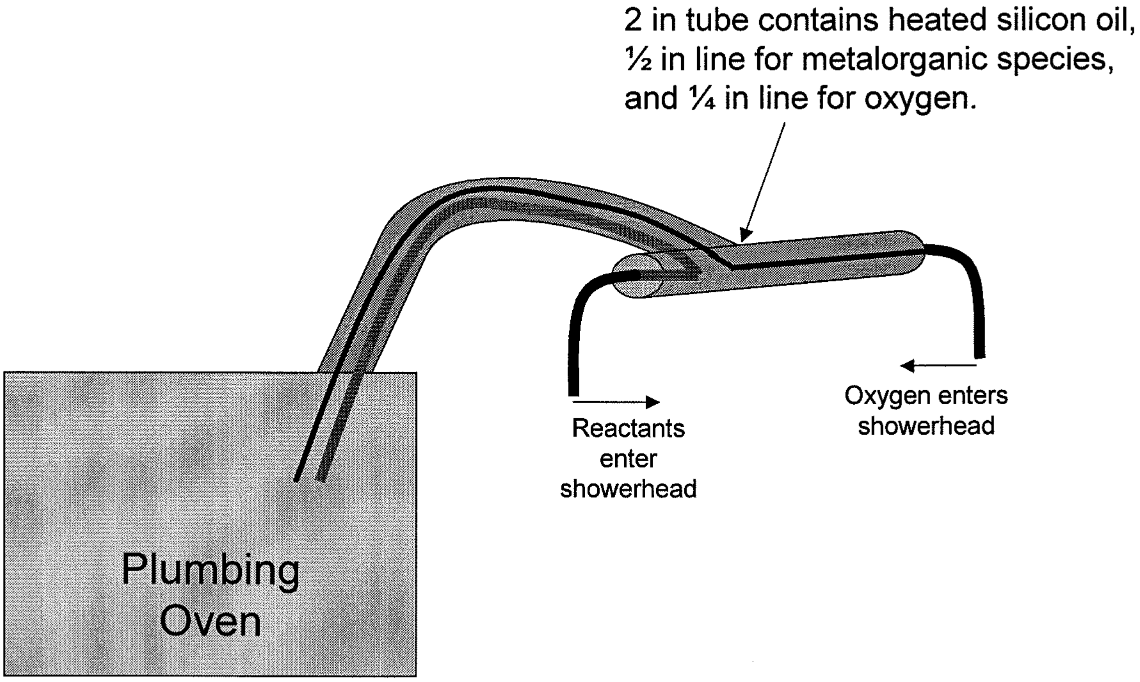

Figure 2.5: Triple-walled pipe maintains 255°C temperature for the incoming reactant and oxygen flows.

in length were constructed for each of the three gas lines (bulk nitrogen, dummy nitrogen, and oxygen).

The third means of maintaining proper temperature is through the use of a heated silicon oil. As the gases exit the plumbing oven, they enter a specially-made triple walled pipe, Figure 2.5. Inside an outer 2 in stainless steel tube reside: a 1/2 in pipe which contains all three metal-organics and the bulk nitrogen flow, a 1/4 in pipe which carries oxygen to the reactor, and lastly flowing around the previous two pipes is silicon oil which is maintained at an elevated temperature (200 – 250 °C). A Neslab EXACAL EX-250HT high temperature oil bath and circulator provides a continuous flow of oil to this assembly as well as the showerhead and reactor body, as will be discussed in subsequent sections.

Initially, there was excessive heat loss from the outer 2 in tube, so the entire

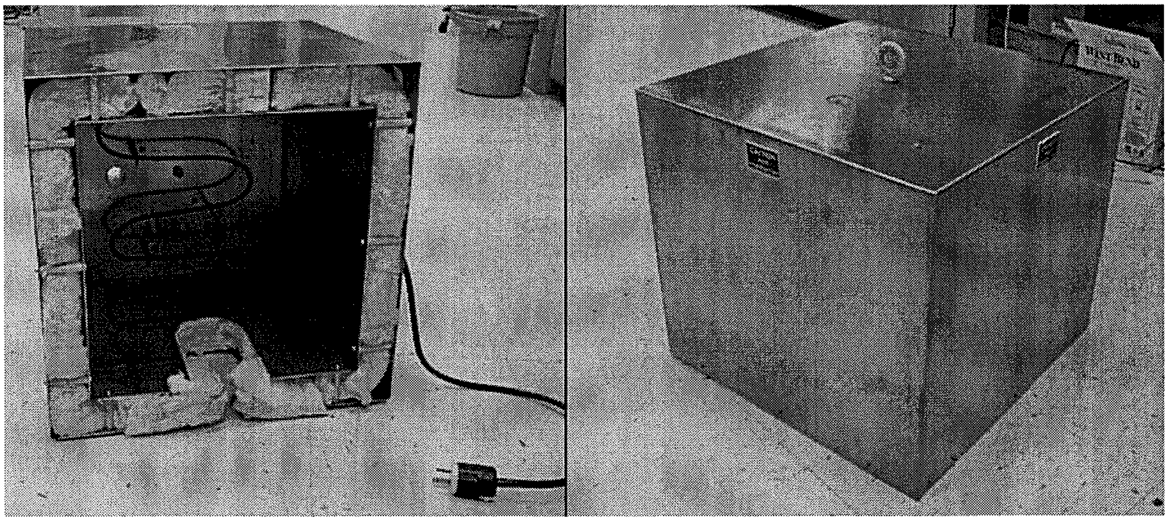

Figure 2.6: Two photographs of the showerhead oven show the heating element and insulation layer (left) and an external view including the opening for thermocouple access and eye-hook for mounting (right).

assembly has been wrapped in a Variac controlled heat tape and fiberglass insulation. Downstream of this assembly, the individual 1/2 in and 1/4 in pipes break out and enter directly into the showerhead.

A fifth oven has also been added, which drops down from the ceiling to enclose the upper portion of the showerhead (discussed later in this chapter), the 1/2 and 1/4 in pipes mentioned above, and all of the associated fittings. Originally these parts were wrapped in heat tape and insulation similar to the tripled walled pipe, but the erratic and unrepeatable concentrations of barium in our films indicated the need for more substantial thermal control over all portions of the gas handling system. The showerhead and its incoming lines had consistently exhibited barium condensation when disassembled and inspected. Once the new showerhead oven was operational, nearly all barium variability ceased.

Due to physical constraints of the existing plumbing and optical diagnostics, the geometrical shape was limited. For ease of assembly, a basic rectangular shape was used; see Figure 2.6. The internal volume of the oven is actually a cube with the dimension of 14 inches in length. For rigidity, the oven is built out of 0.030 in thick stainless steel. Ceramic wool insulation fills a two inch gap around five sides of the oven (the bottom is open in order to envelope the showerhead). The resultant outer dimensions are 18 x 18 x 16 inches.

The heat transfer calculation to determine the thermal power requirements of the oven can be found in Appendix A, along with CAD (computer aided design) drawings of the oven components.

2.1.3 Exhaust Lines

Gasses coming from the plumbing oven which do not travel to the reactor exit through a heated vent line. The vent line contains unreacted precursors immediately prior to and subsequent to a film growth. The vent line connects to the main exhaust line coming out of the reactor.

Downstream of the junction between the vent and exhaust lines, the flow enters a cooling tube. The cooling tube has an inner wall made of brass to enhance thermal conduction. Outside the brass is a water cooling jacket which brings the temperature of the flow down from the extremely hot 800 °C reactor temperature. Immediately downstream of the cooling tube is a liquid nitrogen particulate trap which is filled with stainless steel wool. The cooling tube helps to quell the need for constant LN_2 refilling, while the liquid nitrogen trap prevents the unused metal species from contaminating the vacuum pump or the atmosphere.

At this point, the flow passes through an MKS type 153 exhaust throttle valve which is commanded by an MKS type 146 flow controller. The 146 wraps a PID control loop around the throttle valve and a Baritron type 221 capacitance manometer pressure transducer to control the upstream pressure inside the reactor chamber. The 146 also controls a shroud flow of nitrogen inside the reactor which is discussed further

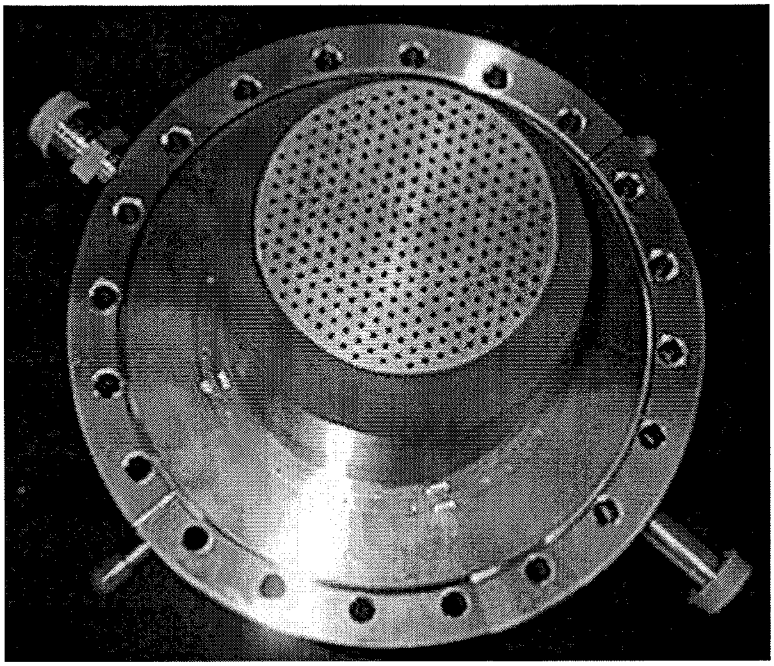

Figure 2.7: Photograph showing the face of the showerhead. Also visible are the incoming gas tubes (large diameter, 5 and 10 o'clock), the oil circulation tubes (small diameter, 2 and 8 o'clock), and the shroud injection holes.

in the next section. Lastly, the gases are expelled through a dual stage Leybold RUVAC vacuum pump which exhausts to a fume hood.

2.2 The Showerhead

Of central importance to a stagnation flow CVD reactor is the showerhead. Our design for a showerhead focused on two major aspects, fluid flow requirements, and thermal restrictions, although desired material properties also impacted the final specifications.

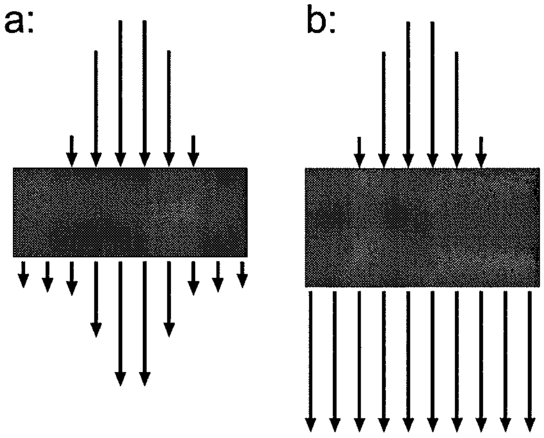

Figure 2.8: Non-uniform flow can result from insufficient pressure drop across the showerhead.

2.2.1 Flow Uniformity

In order to insure smooth homogeneous uniform films, the showerhead must provide a uniform flow pattern across the entire face. Since the incoming gases emerge from small tubing (1/2 in and 1/4 in) they impinge on the inside face of the showerhead as jets. To prevent the emergence of a similar jet-type pattern on the outlet of the showerhead, the showerhead orifices must have a pressure drop greater than that of the dynamic pressure of the incident jet. Conceptually, this is illustrated in Figure 2.8.

Analytically, the dynamic pressure of the incoming flow and the pressure drop across the face of the reactor must be calculated. First the dynamic pressure,

$$P_D = \frac{1}{2}\rho_p v_{in}^2 , \tag{2.5}$$

where ρ_p is the density of gas in the plenum and v_{in} is the velocity of the incoming gas,

$$v_{in} = \frac{Q}{\pi r^2}\left(\frac{760\,\mathrm{torr}}{P_p}\right)\left(\frac{T_p}{298\,\mathrm{K}}\right) . \tag{2.6}$$

In this case, Q is the volume flowrate of gas entering the showerhead's plenum at standard temperature and pressure, and πr^2 is the area of the incoming gas tube. We designed for a maximum Q of 10 slm and 1/2 in O.D. inlet pipe with 0.035 in thick walls, $r = \frac{1}{2}/2 - 0.035 = 0.215\,\mathrm{in} = 0.546\,\mathrm{cm}$. Solving for v_{in} yields

$$P_D = \frac{1}{2\pi^2}\frac{\rho_p Q^2}{r^4}\left(\frac{760\,\mathrm{torr}}{P_p}\right)^2\left(\frac{T_p}{298\,\mathrm{K}}\right)^2 . \tag{2.7}$$

For the pressure drop across the showerhead, a few basic parameters of the showerhead are required. These include N_h, the number of holes in the showerhead, L_h, the length of the holes, D_h, the diameter of the holes, D_{sh}, the diameter of the showerhead, and μ, the viscosity of the gas in the holes. In addition, v_{out}, the average velocity of the gas across the full showerhead diameter, must be calculated:

$$v_{out} = \frac{Q}{\frac{\pi}{4}D_{sh}^2}\left(\frac{760\,\mathrm{torr}}{P_{out}}\right)\left(\frac{T_{out}}{298\,\mathrm{K}}\right) . \tag{2.8}$$

As we will show the density of gas in the showerhead, ρ_p, is a function of the pressure drop through the showerhead, Δp. Using the above parameters,

$$\Delta p = \frac{v_{out}}{C_{sh}} \tag{2.9}$$

and it is clear that

$$P_{out} = P_p + \Delta p . \tag{2.10}$$

The showerhead parameter, C_{sh}, is defined by Vosen [156] as

$$C_{sh} = \frac{N_h D_h^4}{32 \mu D_{sh}^2 L_h} \,. \tag{2.11}$$

Thus

$$\Delta p = \frac{Q}{\pi} \left(\frac{760\,\mathrm{torr}}{P_{out}} \right) \left(\frac{T_{out}}{298\,\mathrm{K}} \right) \frac{128 \mu L_h}{N_h D_h^4} \,. \tag{2.12}$$

The operating pressure inside the reactor, downstream of the showerhead, is P_{out}. Plugging into the ideal gas law yields

$$\rho_p = \frac{P_p}{RT} = \frac{P_{out} + \Delta p}{RT} \,. \tag{2.13}$$

Since the dynamic pressure depends on the plenum density, ρ_p, and the plenum density is dependent on the showerhead parameters, we iteratively selected showerhead parameters N_h, D_h, and L_h such that the dynamic pressure was significantly less than the pressure drop across the showerhead (*i.e.*, $\Delta p > P_D$) and the final design was manufacturable. Ultimately we arrived upon a showerhead design of $N_h = 313$ holes, with hole diameters of $D_h = 1/16\,\mathrm{in}$, a showerhead diameter of $D_{sh} = 3\,\mathrm{in}$, and a showerhead thickness, $L_h = 1\,\mathrm{in}$, as depicted in Figure 2.9.

Combining equation (2.12), with process parameters of chamber pressure, $P_{out} = 10\,\mathrm{torr}$, temperature of the plenum and showerhead, $T_{out} = T_p = 250\,^\circ\mathrm{C}$, viscosity of $2.850 \times 10^{-5}\,\mathrm{Pa \cdot s}$, and recalling that $Q = 10$ slm $= 1.67 \times 10^{-4} S \frac{\mathrm{m}^3}{\mathrm{s}}$, we arrive at

$$\Delta p = 330\,\mathrm{Pa} = 2.5\,\mathrm{torr} \tag{2.14}$$

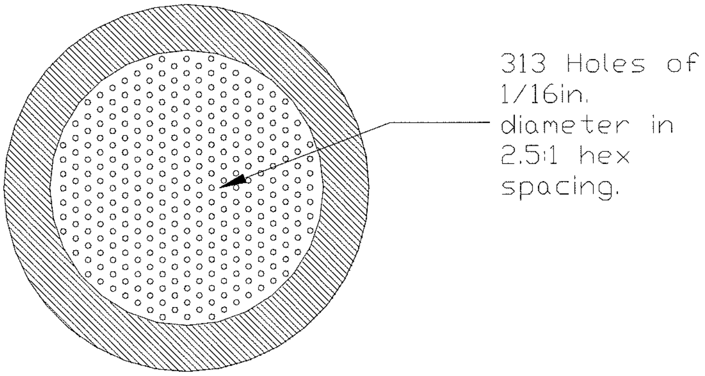

Figure 2.9: Scale drawing of the bottom face of the showerhead.

which yields

$$\rho_p = 1.1345 \times 10^{-2} \frac{\mathrm{kg}}{\mathrm{m}^3} \tag{2.15}$$

and hence

$$P_D = 205.36\,\mathrm{Pa} = 1.5\,\mathrm{torr} < 2.5\,\mathrm{torr} = \Delta p \tag{2.16}$$

Since the dynamic pressure is significantly less than the pressure drop across the showerhead, we are reassured that the flow will be uniform across the full width of the substrate.

2.2.2 Jet Convergence

The second flow-related showerhead design constraint involves the convergence of the jets emerging from the downstream side of the showerhead. If the jets have not sufficiently converged, the film growth will not be uniform. Rather, the film will have a spacial non-uniformity which mimics the array pattern of the showerhead holes. In

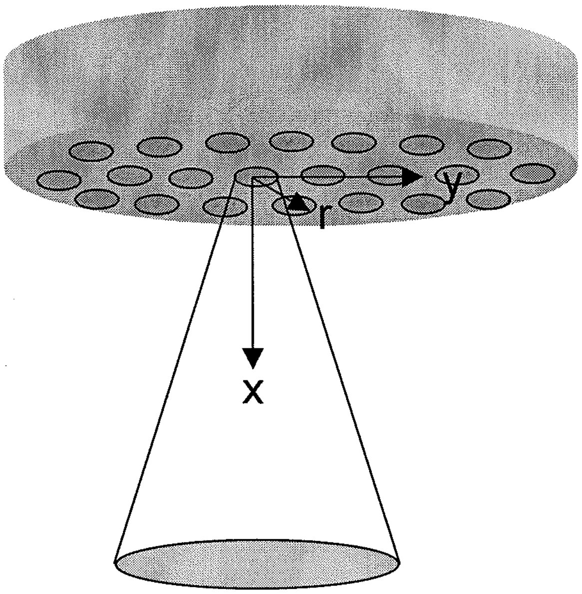

Figure 2.10: Expanding laminar axisymmetric jet emmanating from the face of the showerhead.

order to assure jet convergence, we consulted [166]. In 1933, Schlichting found an exact solution to the Navier-Stokes equations for a laminar axisymmetric narrow jet.

He defined a stream function

$$\Psi(r,x) = \nu x F(\eta) \qquad \eta = \frac{r}{x} \; . \tag{2.17}$$

For this calculation, we define the following variables: ν is the kinematic viscosity of the gas ($3.02\times10^{-3}\frac{\mathrm{m}^2}{\mathrm{s}}$ at a pressure of P=10torr and temperature of T=250°C), x and y are as defined in Figure 2.10, r is defined as $r = \sqrt{x^2+y^2}$, u is the velocity in the x direction, and v is the velocity in the y direction. Solving the momentum and continuity equations

$$\frac{\partial u}{\partial x} + \frac{1}{r}\frac{\partial}{\partial r}(rv) = 0 \tag{2.18}$$

$$u\frac{\partial u}{\partial x} + v\frac{\partial u}{\partial y} = \frac{\nu}{r}\frac{\partial}{\partial r}\left(r\frac{\partial u}{\partial r}\right) \tag{2.19}$$

yields

$$F = \frac{(C\eta)^2}{1 + (C\eta/2)^2} \tag{2.20}$$

where the constant C can be found from the momentum of the jet,

$$J = \rho \int_0^\infty u^2 2\pi r \; dr = \frac{16\pi}{3} \rho C^2 \nu^2 \; . \tag{2.21}$$

Thus,

$$C = \left(\frac{3J}{16\pi\rho\nu^2} \right)^{1/2} \; . \tag{2.22}$$

From the definition of a stream function, we know that the normal velocity is

$$u = \frac{1}{r}\frac{\partial\Psi}{\partial r} = \frac{\nu F'}{r} = \frac{\nu}{r} 2C^2\eta \left(1 + \frac{(C\eta)^2}{4} \right)^{-2} \; . \tag{2.23}$$

In terms of (x, r), u becomes

$$u(x,r) = \frac{2\nu C^2}{x} \left(1 + \left(\frac{Cr}{2x} \right)^2 \right)^{-2} \; . \tag{2.24}$$

In this showerhead, there are over 300 neighboring jets. Although the presence of multiple jets undoubtedly alters the flow patterns of each jet, we can still use the single jet calculation to assure convergence, because it represents the extreme case. We also imposed the requirement that the velocity of each jet be reduced by no more than 50% at the center of a neighboring jet. In other words,

$$u(x,R) = \frac{1}{2} u_{max} = \frac{u(x,0)}{2} \tag{2.25}$$

where R is the distance between neighboring jets (0.397cm in our case). Hence,

$$\frac{2\nu C^2}{x}\left(1+\left(\frac{CR}{2x}\right)^2\right)^{-2}=\frac{1}{2}\cdot\frac{2\nu C^2}{x}\ . \tag{2.26}$$

Solving for x gives us the distance below the showerhead at which point the jets have converged:

$$x=\frac{CR}{2\sqrt{\sqrt{2}-1}}\ . \tag{2.27}$$

In order to calculate C, we need to know the momentum of the jet through each hole,

$$J=\dot{m}_{hole}\,\overline{u}_{hole}\ . \tag{2.28}$$

Recalling that

$$\overline{u}_{hole}=\frac{Q}{\frac{\pi}{4}D_h^2N_h}\left(\frac{760\,\text{torr}}{P_{out}}\right)\left(\frac{T_{out}}{298\,\text{K}}\right)=36.0\frac{\text{m}}{\text{s}} \tag{2.29}$$

and

$$\dot{m}_{hole}=\frac{Q*\rho_{STP}}{N_h}=6.0718\times10^{-7}\frac{\text{kg}}{\text{s}} \tag{2.30}$$

yields

$$J=2.185\times10^{-5}\frac{\text{kg}\,\text{m}}{\text{s}^2}\ . \tag{2.31}$$

Substituting into equation (2.22) and calculating x from equation (2.27) results in

$$x=1.26\,\text{cm}\ . \tag{2.32}$$

In the final design, the distance between the showerhead and substrate is 1.5 inches (3.8 cm) which is more than sufficient for proper convergence of the jets.

2.2.3 Physical Constraints

Having worked out the numerical aspects of the fluid flow within the showerhead, we next had to work out the logistical aspects of building and sealing such a complex and crucial component of the CVD system.

From prior experience with building showerheads for CVD of diamond we knew tellurium doped copper offered the best compromise between machinability (Te-copper is much less malleable than pure oxygen free copper), thermal conductivity, and inertness (the actual showerhead resists both oxidation and reaction with the precursors). In addition we required stainless steel components at each of the seal points. (Conflat vacuum hardware use an oxygen free pure copper o-ring sandwiched between two stainless steel flanges with annular knife edges that bite down into the copper gasket for sealing. In order to assure proper mating, the sealing face must have sufficient hardness to bite into the copper.) We designed the Te-copper to reside entirely within the reaction chamber, and as such did not require a vacuum seal between the copper and stainless steel portions of the showerhead.

Designing passages which ensure proper flow of the silicon oil was particularly challenging. The oil heats the stainless steel portion of the showerhead (to prevent precursor condensation) and cools the copper portion of the showerhead (which is heated by radiation from the substrate and inconel can).

The final design for the copper portion of the showerhead involves an outer cylinder which was bored out of solid Te-copper rod stock (the end of which became the face of the showerhead). Inside of this cylinder, there is a second cylinder which has a helical groove machined into its outer surface. The two cylinders were then furnace

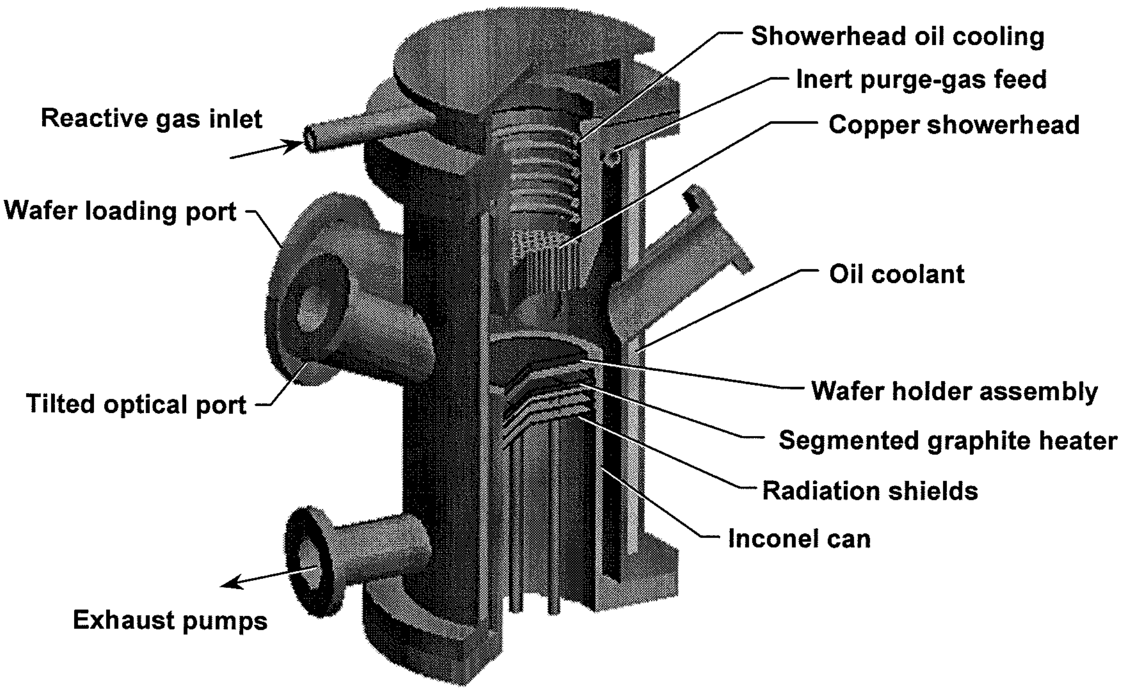

Figure 2.11: Cutaway view of the reactor. (Not to scale.) Courtesy of Robert J. Kee, Colorado School of Mines.

brazed together. The oil enters at the bottom of the helical groove and travels up the inside between the two cylinders until it exits through a 1/4 inch copper tube. Before entering the helical groove, the oil circulates through a double walled stainless steel jacketing in the top portion of the showerhead. Appendix B contains detailed CAD drawings of four different views of the showerhead.

2.3 The CVD Chamber

The heart of our CVD reactor is the reacting zone near the substrate; see Figure 2.11. Three components govern the geometry of this zone, the showerhead, the chamber body, and the inconel can.

2.3.1 Wafer Support Assembly

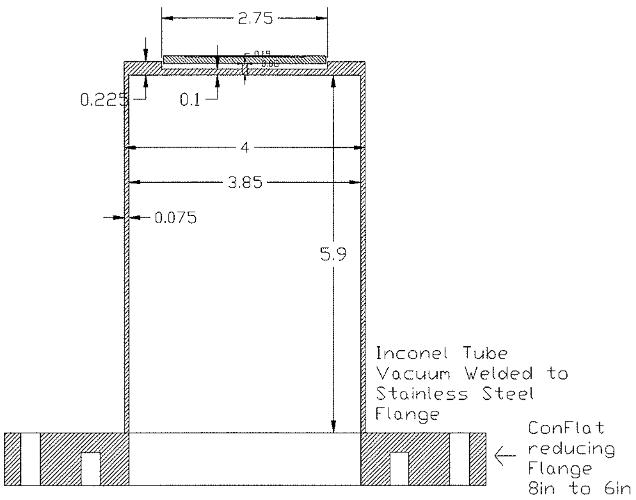

Figure 2.12: Inconel can with susceptor and substrate on top.

The "wafer holder assembly" consists of a substrate resting on a susceptor[2] made of silicon carbide (Carborundum Corporation's Hexaloy brand material) which in turn rests on a can made of inconel metal. This inconel can serves to encase the heaters and support the substrate; see Figure 2.12.

The susceptor levitates on top of a gas bearing. The gas bearing consists of several small holes which allow gas to escape from the inconel can. As the gas travels out of the holes, it enters radial grooves which circularly accelerate the gas. This rotational momentum of the gas is then imparted to the susceptor which is floating on top of the gas cushion. A photograph of the grooves as machined is shown in Figure 2.13. The schematic in Figure 2.14 depicts the splines as they were cut into the inconel to form the grooves in which the gas travels. In the center of the figure is the round pin on which the susceptor spins. The six small black dots represent 1mm holes through

---

[2] It may be worth noting that in our case the name "susceptor" is not entirely appropriate. In many CVD reactors, the substrate is heated by RF induction, in which case, the susceptor is the focal point of the electro-magnetic radiation which in turn heats the substrate. As such, the traditional susceptor directly holds the substrate and heats it electromagnetically, while our susceptor holds the substrate and heats it conductively.

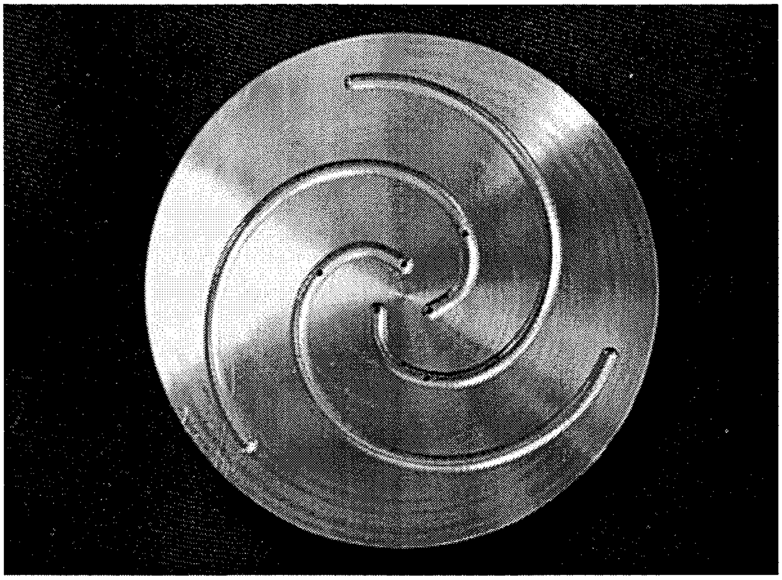

Figure 2.13: Photograph of the gas bearing as machined into the top of the inconel can.

which the gas travels.

We experimented with several different spline geometries and two different gases, helium and nitrogen, before settling on the final design. Because of greater thermal conductivity, helium is the preferred gas. Additionally, the helium gas, which is injected into the inconel can below the heaters, serves to purge the inconel can and heater assembly, keeping it free from oxygen, which would destroy the graphite heaters through oxidation.

Attached to the bottom of the inconel can is a six way cross as illustrated in Figure 2.15. Typically a standard vacuum hardware component, this cross was modified to fit comfortably inside the frame which supports our reactor. Of the six openings, one is blank while the others connect to: the inconel can, a gas feedthrough which supplies helium for purge and gas bearing use, a thermocouple feedthrough which allows internal instrumentation of the inconel can, a vacuum exhaust port which connects to a second pump (allowing us to pump down the cross and chamber

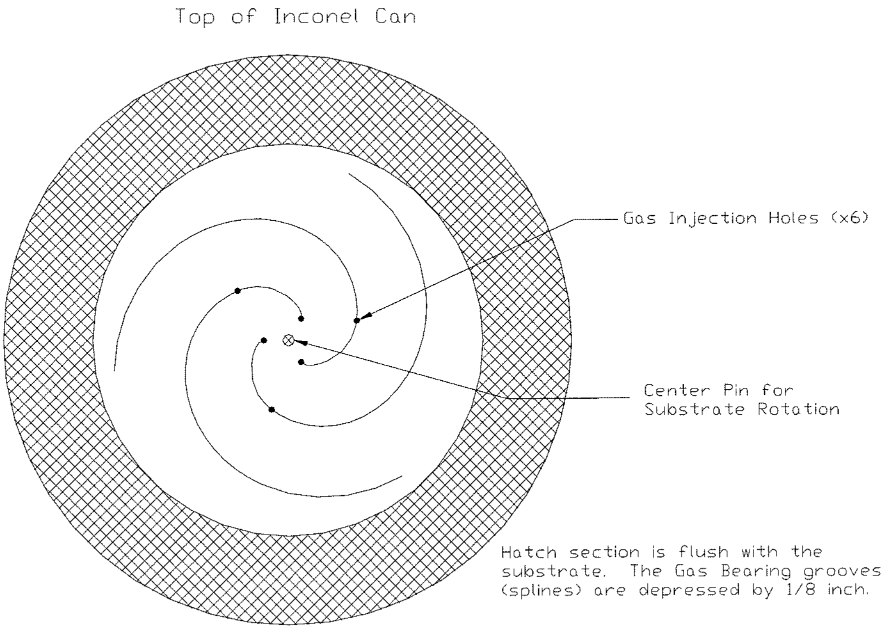

Figure 2.14: Pictured is a schematic of the gas bearing, as machined into the top of the can.

simultaneously, without resulting in a pressure difference capable of launching the susceptor off the inconel can and shattering the substrate), and finally an electrical power feedthrough with four independent connecting copper rods (this allows us to potentially run 3 heater zones, although our heater design incorporates a 2 zone system).

2.3.2 The Chamber Body

The design of the main body of the reactor focused on three major constraints: fluid dynamics, optical diagnostics / sensors, and thermal requirements. Our initial diagnostic goals involved the use of Fourier Transform Infrared spectroscopy (FTIR). In order to use FTIR to study both the film and gas phase *in-situ*, the chamber body requires two sets of viewports. The first set is designed for analyzing the gas phase

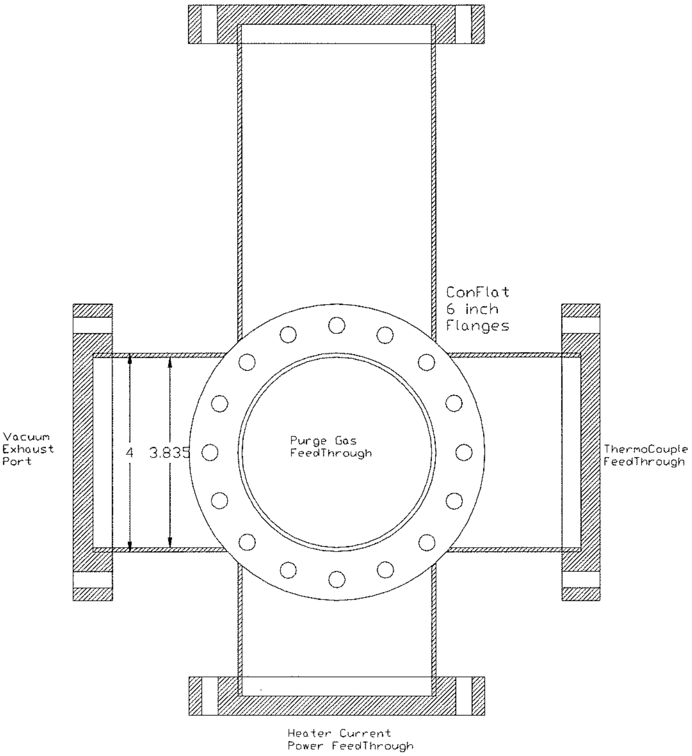

Figure 2.15: Six-way cross connects to the bottom of the inconel can.

chemistry and decomposition of the precursors. As such, this set of ports is aimed at the midpoint between the showerhead and the substrate. Because we have designed these viewports around a 2 inch IR beam (and a similarly sized set of zinc selenide windows) and the space between the substrate and showerhead is only 1.5 inches, these straight through ports allow optical access to the face of the showerhead and the top of the substrate at a glancing angle of incidence. Notice the alignment in Figure 2.16.

The second set of FTIR viewports is angled at 60 ° relative to the surface normal of the substrate, which allows the FTIR to see the substrate in reflection as the film is deposited (Figure 2.17). In the following photograph, Figure 2.18, a view down into one of the angled viewports is presented. Immediately to the left is one of the straight

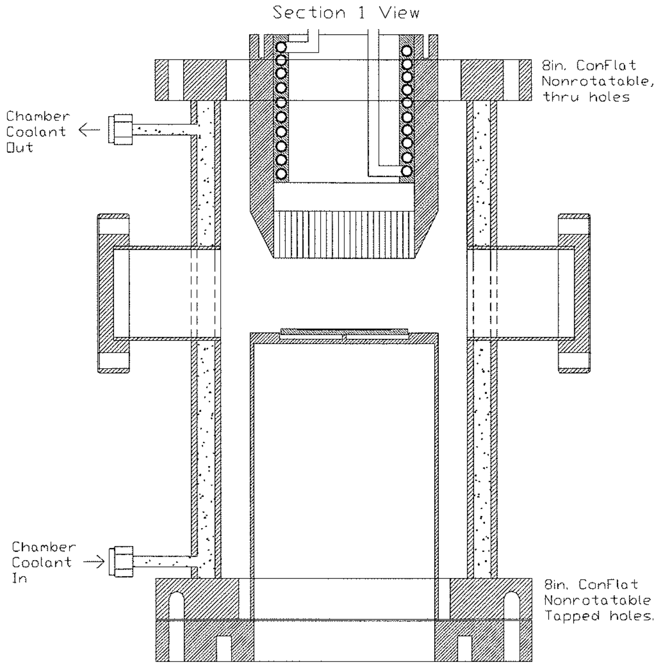

Figure 2.16: Cross-sectional view of the chamber body illustrating the straight through viewports.

through ports, and further to the left is the door. Finally towards the left, the heating oil input and output connections are clearly visible. As mentioned previously, the optics (and hence the viewports) are designed for a 2 in beam. Conflat flanges of 3 3/8 in OD are intended to mate with 2 in tubes. Thus both our angled viewports and straight-through viewports are terminated with Conflat 3 3/8 in flanges.

The final set of viewports are not a matched pair, as the two previous sets have been. First of all, we needed a door for loading and unloading samples into and out of our chamber. Because the entire silicon carbide susceptor needs to be removed for cleaning after each run, an inner diameter of 3 inches was required. In consideration of a possible Reflected High Energy Electron Dispersion (RHEED) system to measure film thickness *in-situ* as the film is being deposited, we have incorporated a sixth port which, when matched with the door, allows for the potential to adapt a RHEED

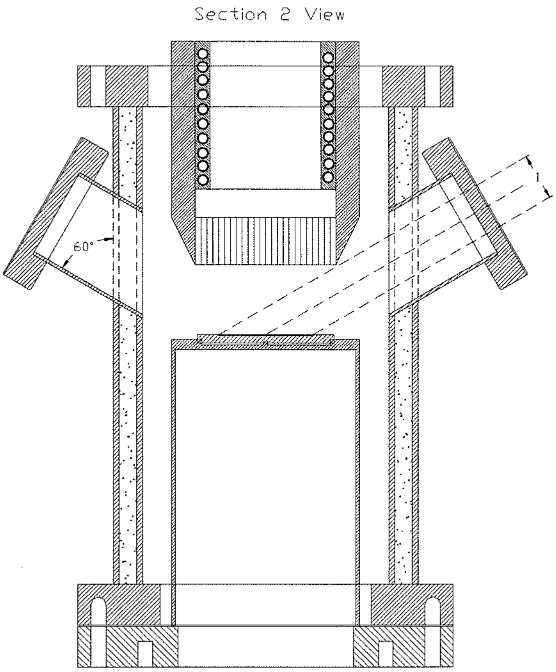

Figure 2.17: Cross-sectional view of the chamber body illustrating the angled viewports. Notice how the showerhead corner was beveled to allow full field scanning of the substrate.

system in the future. A view through the door and out of the RHEED port is presented in Figure 2.19. Additionally, the top section of the inconel can is clearly visible in the doorway. On top of the inconel can is a blank aluminum disc resting in the susceptor depression. Fortunately, since RHEED requires a glancing angle of incidence onto the substrate, we were able to align both the RHEED port and the door with the vertical centerline of the substrate.

The door is designed around a 3 in tube (so that the substrate which has an outer diameter of 2.75 in can pass safely through), which necessitates termination with a Conflat 4 5/8 in flange. The RHEED port which only needs to pass a narrow electrical beam is built around a smaller 1.5 in tube and is terminated with a 2 3/4 in Conflat flange.

Also clearly present in Figure 2.19 are the two angled vacuum flanges at the

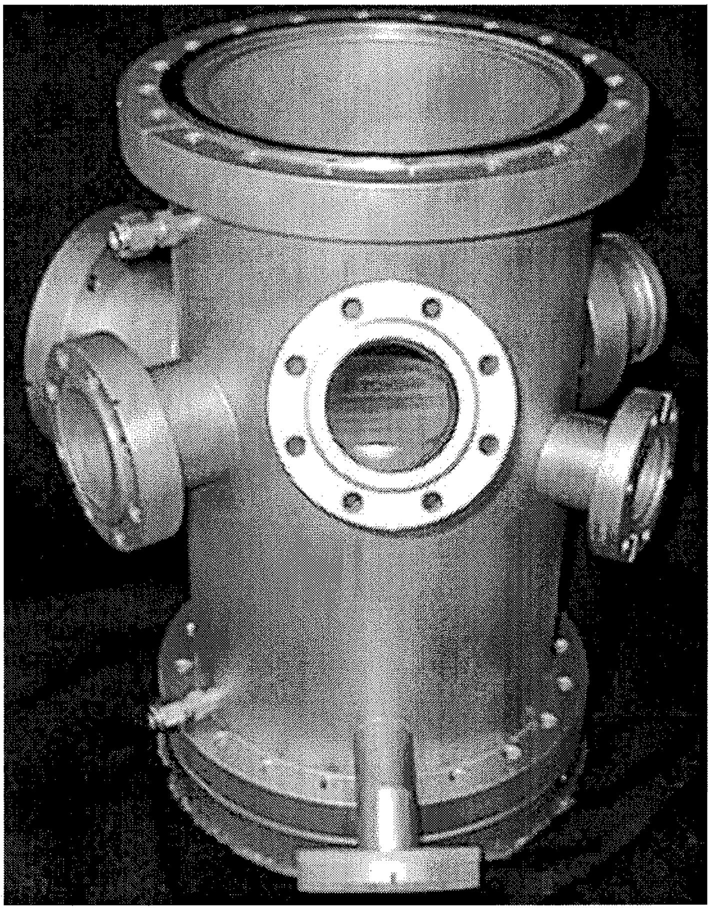

Figure 2.18: Chamber body as viewed along the axis of one of the angled viewports. Inside the viewport would be a substrate, although in this picture there is an aluminum blank.

bottom of the chamber. These two angled vacuum ports (2 3/4 inch Conflat) are provided for pumping and sensing the vacuum. The right port is attached to a capacitance manometer from MKS which feeds the PID loop built into the exhaust throttle valve mentioned in the Gas Handling System section. The left port is attached to the particle trap and then finally to the vacuum pump.

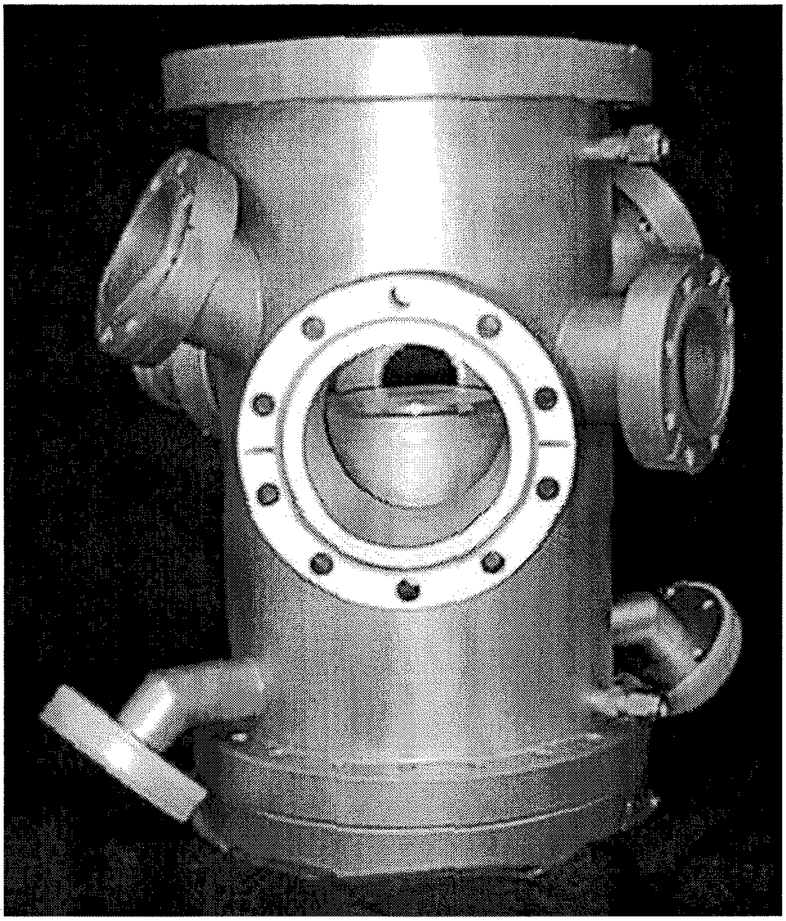

Figure 2.19: Chamber body as viewed along the axis of the door. Note how the door and RHEED port are aligned for glancing angle of incidence onto the substrate.

2.3.3 CVD Modeling Efforts

The task of determining precise dimensions for the inconel can, showerhead and chamber body fell to our modeling team. Professors Robert Kee and Laxminarayan Raja, at The Colorado School of Mines, led the project's modelling efforts [75]. Their flow code was built on a package from Sandia National Labs entitled CURRENT. The solutions are 2-D axisymmetric finite difference results which include nominal gas chemistry and heat transfer. Some of the initial geometries are shown in Figure 2.20; pictured are species concentration or thermal gradients for a reactor with angled

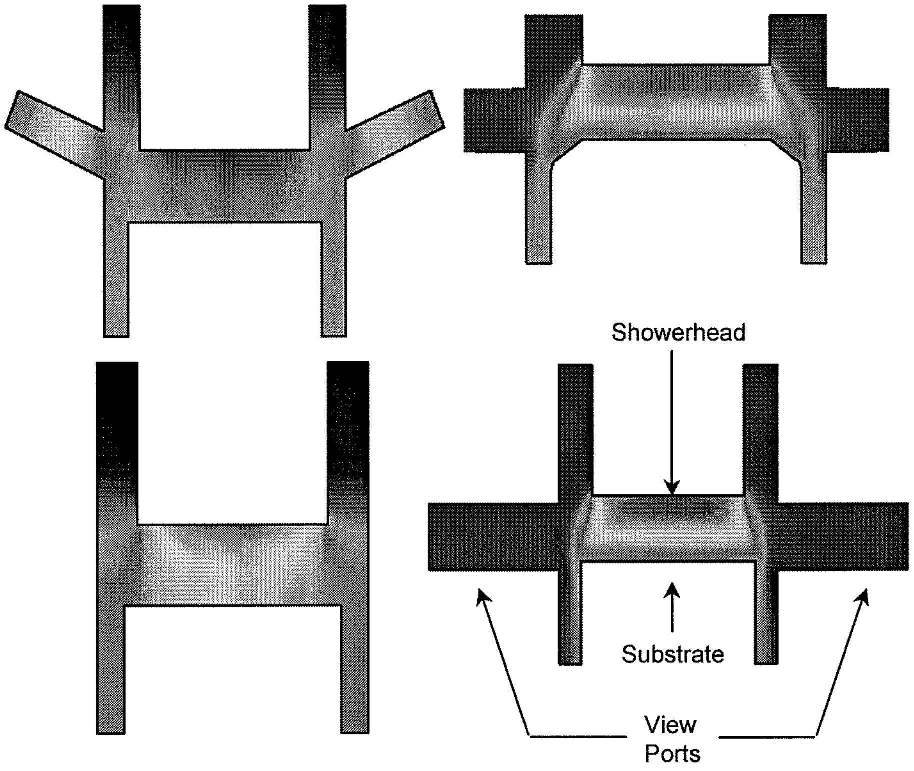

Figure 2.20: Preliminary reaction chamber designs and their corresponding 2-D flow patterns. Courtesy of L.R. Raja and R.J. Kee of the Colorado School of Mines.

viewports, short and long straight viewports, no viewports, and a beveled can.

The final design incorporated a beveled showerhead for full film visibility and a flat surfaced inconel can, as shown in Figure 2.21. In addition, the design proved to be very robust to changes in process conditions. The composite results of numerous simulations is depicted in Figure 2.22. Despite varying the showerhead diameter, showerhead to substrate distance, operating pressure, showerhead flowrate, and viewport purge flowrate, the uniformity of deposition was never off by more than 2.5%.

Thermally, the chamber walls have similar requirements to the face of the showerhead. The inner walls of the chamber body need to be warm enough to prevent condensation of the precursor gases (at least 235 °C). However, if they become too hot, YBCO could potentially deposit onto the walls. Once the decision to use the

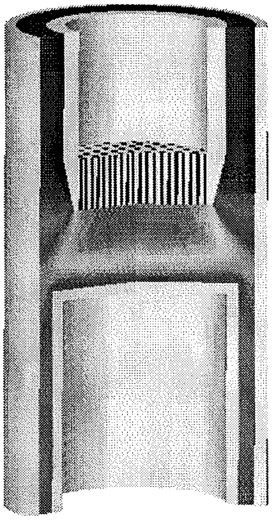

Figure 2.21: Fluid flow model results pasted in a three-dimensional rendering of the reaction chamber. Courtesy of L.R. Raja and R.J. Kee of the Colorado School of Mines.

high temperature silicon oil to stabilize the temperature of the showerhead was made, the addition of some simple plumbing allowed us to use of the same system to regulate the temperature of the chamber body (note the coolant inlet and outlet ports in figures 2.16 and 2.18).

2.3.4 Window Flanges

The incorporation of FTIR spectroscopy necessitates the use of either zinc selenide or potassium bromide windows are sensitive to extreme temperatures. The spectral features of YBCO and MgO are best suited to zinc selenide windows. In addition, the windows are required to remain clean from precursor deposits. The solution to satisfy these requirements was to design and fabricate an adaptable windowed flange; see Figure 2.23.

We began with a 3 3/8 inch Conflat flange for which our FTIR viewports were

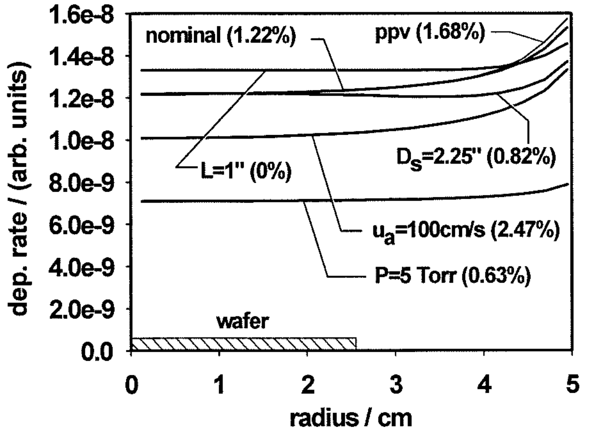

Nominal conditions:

- active flow, u_a = 200 cm/s
- shroud flow, u_p = 100 cm/s
- showerhead dia. D_s = 3"
- shower-to-wafer dist., L = 1.5"
- pressure, P = 10 Torr
- susceptor temp., T_s = 1100 K
- inlet temp., T_i = 500 K

Note:- ppv = perpendicular viewport with 50 cm/s purge

Figure 2.22: Robustness of the reaction chamber design is confirmed by varying process parameters (see text for description). Courtesy of L.R. Raja and R.J. Kee of the Colorado School of Mines.

designed. Inside the flange we machined a trough designed as a cooling water channel. Punching perpendicularly through the trough a 1/8 inch tube was welded in at the ID and OD of the Conflat flange. This tube allows for a purge gas to be injected on the vacuum side of the windows. The purpose of the purge gas is to prevent potential contaminants from coming out of the reaction zone and depositing on the cooled. Finally two 1/8 inch holes were drilled into the flange passing from the outside into the trough at opposite ends of the Conflat flange from each other. Swagelock fittings were welded to the outlet of each of these 1/8 inch holes, and they serve as the inlet and outlet ports for the cooling water.

The final modification to the standard 3 3/8 inch Conflat flange involved the

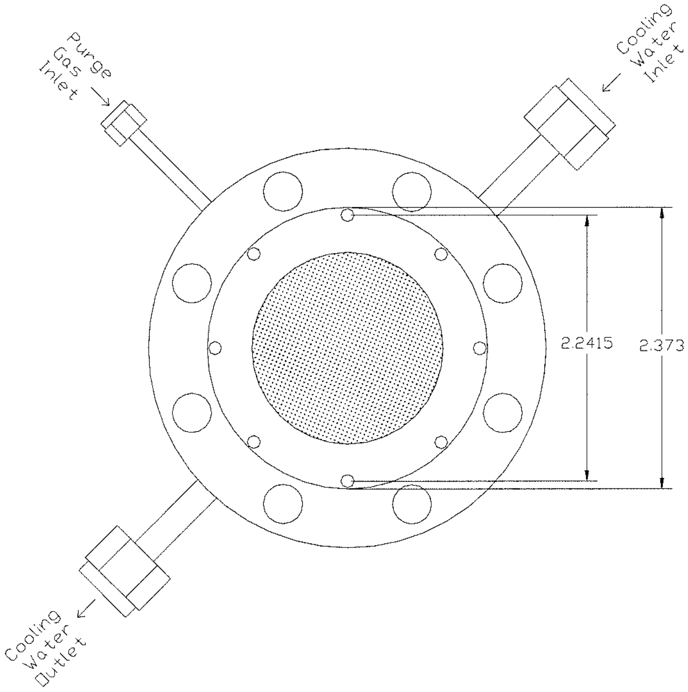

Figure 2.23: Top down view of the adaptable windowed flange.

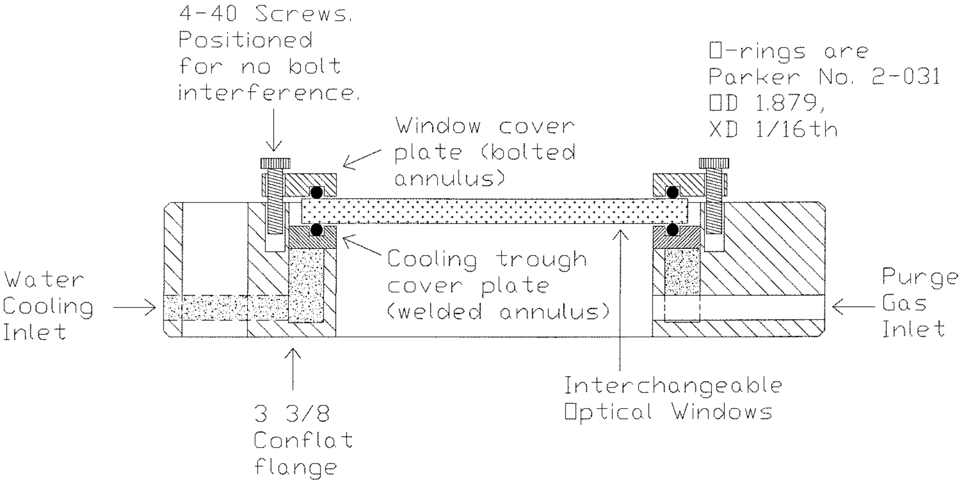

Figure 2.24: Cross-sectional view of the adaptable windowed vacuum flange.

securing ring which holds the window in place. Due to the already limited space between the bolt circle of the flange and the 2 inch opening, we had to design and build an extremely small window fixture. Using small cross-section viton o-rings and small screws, we were able to squeeze in the required hardware to seal the window to our vacuum system; see Figure 2.24.

In its final design (and implementation) the adaptable windowed flanges are quite flexible. They allow us to alternate between zinc selenide, potassium bromide, quartz, fused silica, and sapphire windows (each of which is suited to a different band of light), and to adjust the amount of cooling and purge gas the windows receive.

2.3.5 The Heaters

The entire assembly (heater, can, susceptor, substrate, and showerhead) were modeled for heat transfer, most notably radiation [51]. Many of our material choices were heavily influenced by the results of this work. For example, silicon carbide was chosen for a high thermal conductivity. Other key factors addressed by this choice of material include resistance to oxidation at high temperatures, cost, and emissivity in the infrared (for enhanced radiative heat transfer). In addition the wall thicknesses of the inconel can and the thickness of the silicon carbide susceptor were minimized in order to permit the highest degree of thermal controllability.

Complementing the modeling efforts, we built many prototypes of the heaters, can, and gas bearing. We began with a conceptual design similar to a reactor designed by Breiland [18] as a rough template for our stagnation flow MOCVD reactor. Breiland uses Kanthal brand nickel tungsten wire to resistively heat his sample. Our initial experiments with Kanthal showed that after prolonged exposure to temperatures near the wire's maximum operating temperature, Kanthal became extremely brittle and delicate in nature. Frequently breaking apart, the wire was easily rendered useless

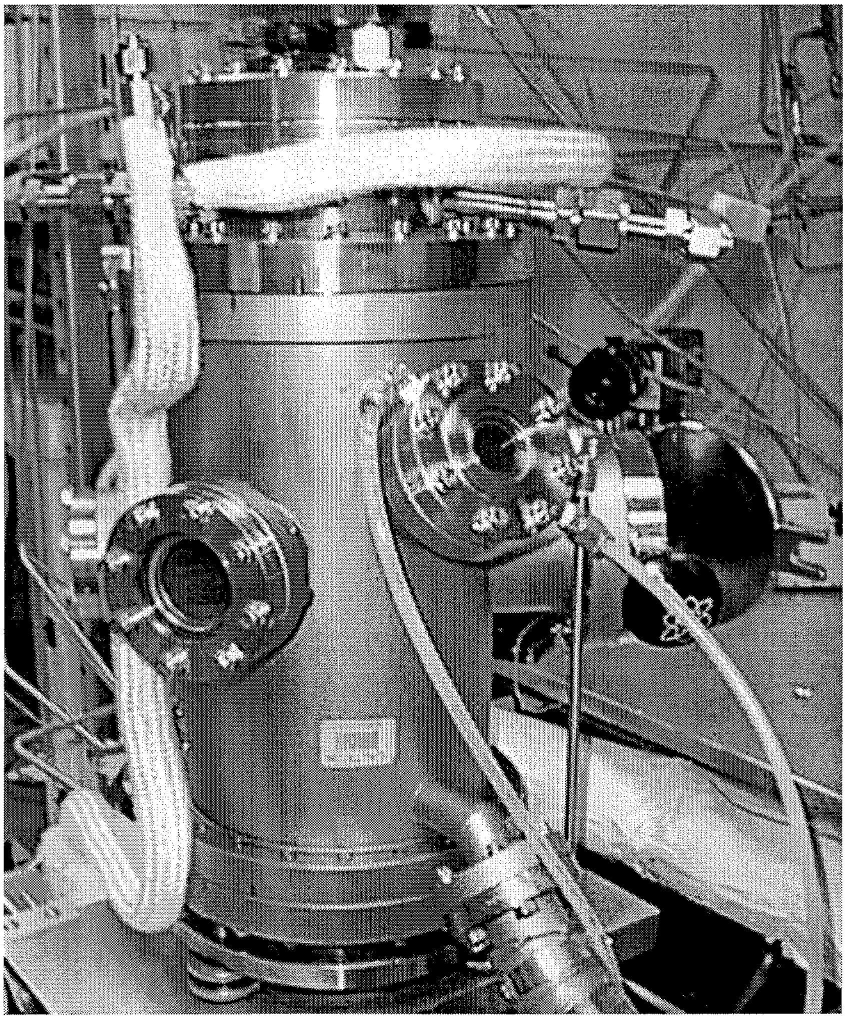

Figure 2.25: The reactor in operation. In the front left is one of the straight-through ports. In the front right is one of adaptable windowed flanges we designed. Note the connections for water (plastic tubing) and nitrogen gas (stainless steel line to the right of the flange).

by our extreme temperature demands.

Using published MOCVD of YBCO results [160] and the assistance of our industrial partners at Superconductor Technologies Incorporated [105], we established a target of 800 °C for our film growth temperature. Preliminary thermal modeling results indicated the necessity of heater temperatures greater than 1500 °C. After the failures of Kanthal, we turned to graphite resistive heaters for our system.

We decided on a 2 zone spiral heater geometry. Using a separate center and outer zone, we can actively vary the radial uniformity (or non-uniformity) of the sample's temperature profile. Compromising between the demands of heater assembly, machinability, and thermal uniformity, we arrived at the design depicted in Figure 2.26. Current flows from the tabs on the outer edge of each spiral through to the center. Hence, the two heaters share a common ground connected through a center post. The large hole on the upper right allows the connecting post for the inner heater (which sits above the outer heater) to pass through the outer heater without shorting out to ground.

The connecting posts (three in all) are made of 4-40 threaded molybdenum rods, nuts and washers. Molybdenum is appropriate because of a high melting temperature and limited resistance to oxidation. The heaters rest on a plate made from boron nitride machinable ceramic. Below the boron nitride is a sequence of heat shields. Two sheets of molybdenum are separated by three sheets of zirconium ceramic felt. The entire assembly rests on a podium constructed of four 20 inch long copper posts; see Figure 2.27. The copper posts are attached to each other using ceramic electrical stand-offs. In addition to structural support, the copper posts also provide the conduction path for the heater current. At the bottom, the posts attach to a standard high current electrical vacuum feedthrough.

At the outlet of the electrical feedthrough 12 gauge copper wiring connects the heater to a bank of three Hewlett Packard 6269B DC power supplies. Although

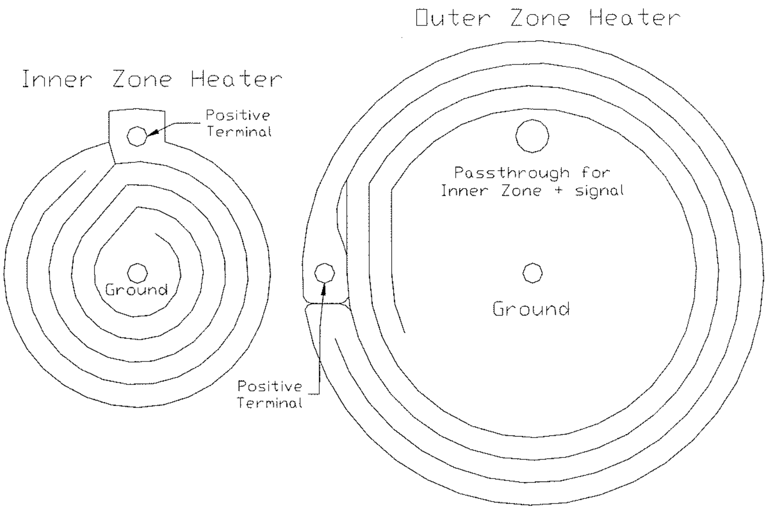

Figure 2.26: Graphite resistive heater. Left image depicts the inner (center) zone, while the right image is of the outer zone.

more expensive to supply than alternating current, direct current power was chosen for its lower electromagnetic noise inside the system. Each power supply is capable of providing nearly 1.5 kilowatts of power through a resistance of 1-2 ohms. Although appropriate for the inner zone (resistance is typically 2 ohms), the outer zone exhibits a typical resistance of 4 ohms. As a result we use two power supplies in series to provide twice the voltage of a single power supply when powering the outer zone. For most of our experimental conditions and maximum uniformity, the outer zone provides all of the heat, which can be as much as 1.8 kilowatts.

The power supplies are wired for external setpoint control and are commanded by the data acquisition PC. Our system control software provides for thermal control of the heaters using a PID loop. The inside of the Inconel can has thermocouple probes which measure the temperature of the can at three different locations. Any of these probes can be set as the control loop sensor for the heaters.

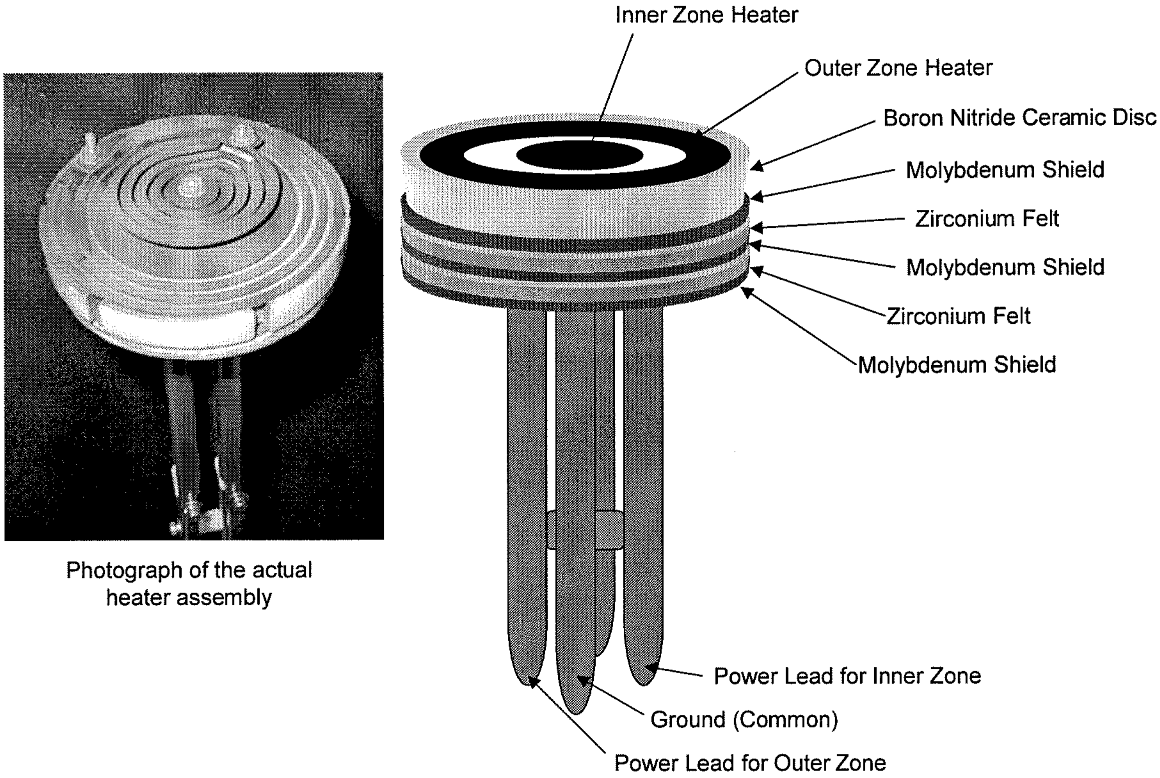
Photograph of the actual heater assembly

Figure 2.27: The heater assembly inserts into the bottom of the six-way cross and slides all the way up into the inconel can in order to provide heat to the substrate.

2.4 Sensing and Diagnostics

2.4.1 Ultraviolet Composition Control

Controlling the stoichiometry of the film is of utmost importance when building a multi-species thin film reactor. The most significant means of adjusting film stoichiometry is through the gas composition of the boundary layer. For our reactor, the amount of yttrium, barium, and copper which reaches the boundary layer is governed by the flowrates through the bubblers. The quantity of precursor delivered could potentially also be controlled by adjusting the temperature of the bubblers; however, for practical reasons our stoichiometry control relies exclusively on changing the flowrates of the carrier gas.

We devised a control loop based on the work of Desisto and Rappoli [33]. They determined that the $Y(tmhd)_3$, $Cu(tmhd)_2$, and $Ba(tmhd)_2$ precursors each have a distinct absorption peak in the ultraviolet spectrum. With this knowledge, we designed a four way ultraviolet spectroscopy system utilizing an Ocean Optics S-2000 spectrometer, Fiberguide aluminized high temperature optical fibers, and an Analytical Instrument Systems Inc. UV-2 deuterium lamp. The spectrometer is attached to a data acquisition card inside of the control PC. Data collection and processing are all handled within the control system software for the reactor.

Unfortunately, the absorption peaks are overlapping, so that we were unable to use a single optical cell for all measurements. Three distinct optical cells measure the precursor quantities, while a fourth optical line is used as a master signal to account for lamp drift, and solarization of the fibers[3].

The cell design incorporates a 10 cm optical path length as pioneered by Desisto and Rappoli. Our design is illustrated in Figure 2.28, while a photograph of the cells as installed can be seen in Figure 2.29. The gases enter and exit through the threaded VCR vacuum fittings located at the top of the figure. Ultraviolet light is delivered by high temperature aluminized fiber optics. The light passes horizontally through the gas, and is collected at the other end by another optical fiber. The left and right ends are capped off with vacuum flanges containing boro-silicate windows which are transparent in the ultraviolet. Additionally, the fibers are terminated with collimating lenses before contact with the optical cells.

Using the ideal gas law and the definition of the concentration of species i,

$$C_i = \frac{n}{V}\ , \tag{2.33}$$

---

[3] Solarization is a gradual clouding of optical fibers caused by extended exposure to high intensity ultraviolet radiation.

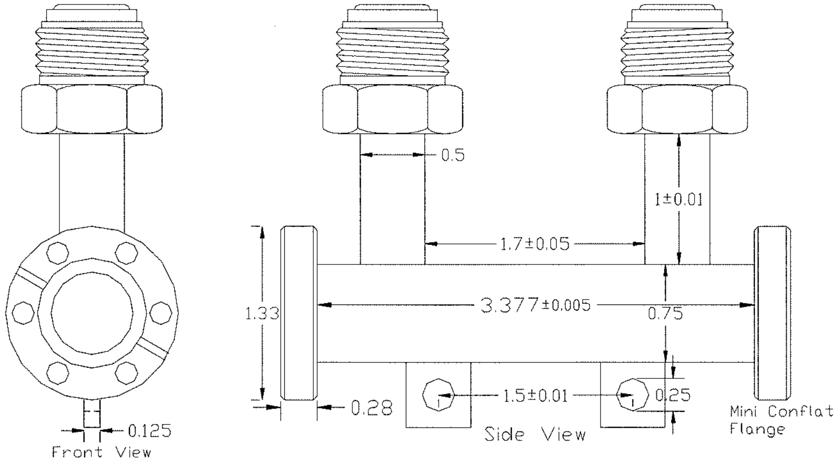

Flow Cell with 10cm Optical Path
Lenght. Features 1/2 in. VCR
fittings and MiniConflat end
Flanges for Optical Access.

Figure 2.28: Optical cell for ultraviolet spectroscopy of precursor gases.

we find

$$P_i = C_i RT \ , \tag{2.34}$$

where P_i is the pressure of the i^{th} species. Beer's Law for a substance, i, absorbing light is

$$A_i = \epsilon b C_i \ , \tag{2.35}$$

where the absorbance, $A_i = f(\lambda)$, is a function of wavelength, ϵ is the molar absorptivity constant, and b is the optical path length. We can derive a relation for the molar flowrate of species i, $\dot{n}_i$, as follows:

$$A_i = \epsilon b \frac{P_i}{RT} \tag{2.36}$$

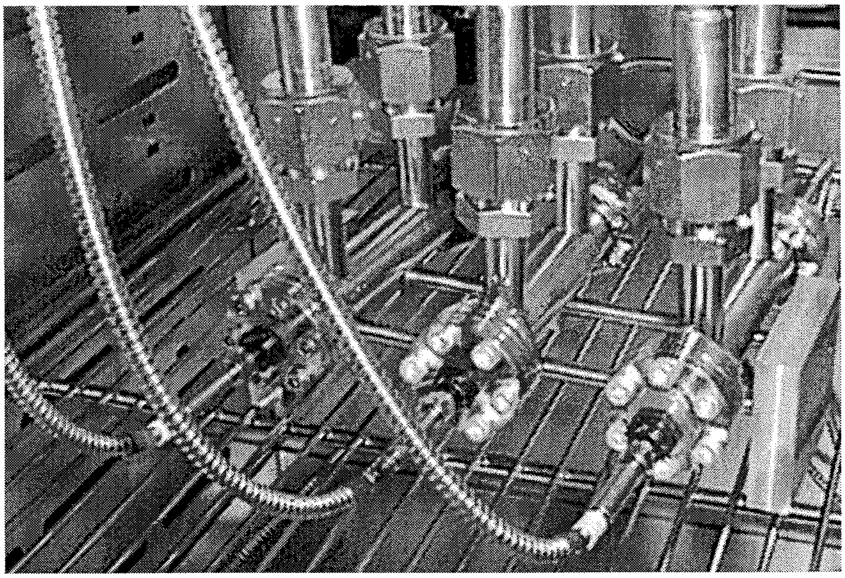

Figure 2.29: Three optical cells shown with attached fibers and gas connections.

and for total pressure in the cell, P, we know

$$P = P_i + P_{N_2} \ , \tag{2.37}$$

since the only materials in the cell are the precursor i, which we want to measure, and the carrier gas, N_2. Similarly, we know

$$\dot{n} = \dot{n}_i + \dot{n}_{N_2} \tag{2.38}$$

and

$$\frac{\dot{n}_i}{\dot{n}_{N_2}} = \frac{P_i}{P_{N_2}} \ . \tag{2.39}$$

Combining equations (2.37) and (2.38) and simplifying:

$$P = P_i \left(\frac{\dot{n}_i}{\dot{n}_i + \dot{n}_{N_2}} \right) . \tag{2.40}$$

Plugging in equation (2.36) yields

$$P = A \frac{RT}{\epsilon b} \left(\frac{\dot{n}_i}{+ \dot{n}_{N_2}} \right) . \tag{2.41}$$

Solving for $\dot{n}_i$, we get

$$\dot{n}_i = \dot{n}_{N_2} \left(\frac{A}{\frac{P}{RT} \epsilon b - A} \right) . \tag{2.42}$$

Thus for our purposes, we can measure absorption, pressure and temperature inside the optical cell, and since ϵ and b are known constants, we can control the flowrate of precursor i by varying the flowrate of carrier gas, $\dot{n}_{N_2}$, through the bubbler. By wrapping the entire process inside a PID control loop, we are able to tightly govern the stoichiometry of precursor gases inside the reaction chamber, all despite gradual decomposition and variability of the organometallics inside the bubblers.

2.4.2 Fourier Transform Infrared Spectrometry

As previously mentioned, the reactor has been designed to include the use of an FTIR spectrometer. Behind the PC which controls and collects data from the spectrometer, in Figure 2.30, is the reactor frame (black beamed structure) which supports the spectrometer and the associated optical components.

Conceptually, an FTIR is a Michelson interferometer, see Figure 2.31, where the light heading for a detector is first reflected off a sample [56]. In an interferometer, the light travels through two separate paths before recombining on route to the de-

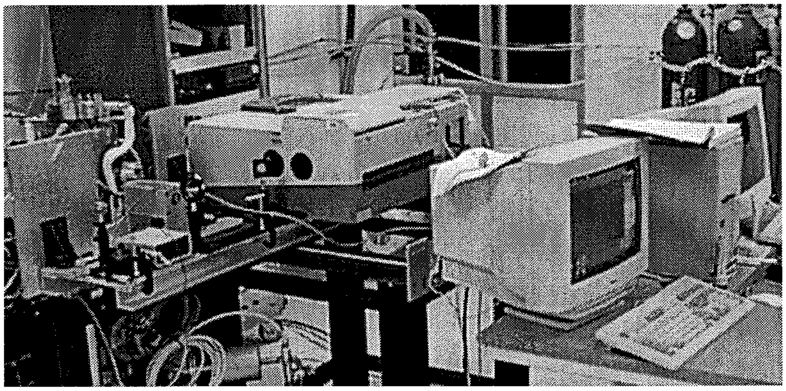

Figure 2.30: Fourier Transform Infrared Spectrometer.

tector/sample. One path is from the source, reflected left off of the beamsplitter, reflected off the stationary mirror, and finally passed through the beamsplitter. The second path also begins at the source, passes through the beamsplitter, reflects off of a moving mirror, reflects to the right off the beamsplitter, and combines with light from the first pathway.

During a scan of the FTIR, the moving mirror passes through a fixed range of travel all while the detector is measuring the intensity of the resultant light; producing an interferogram [56]. A typical interferogram is presented in Figure 2.32. Because the source of light is polychromatic, there are local minima and maxima associated with constructive and destructive interference at each of the many frequencies of light. Of course when the two path lengths are equal, all frequencies constructively interfere resulting in the central peak of Figure 2.32. By taking the Fourier transform of the interferogram, an energy spectra is produced; see Figure 2.33.

All of the optics (mirrors, lenses, detector, mounts, etc.) and the spectrometer itself (Nicolet MagnaIR 560) are attached to a specially designed sliding platform. Built on linear bearings, this platform allows the IR beam to be slid back from the reactor and calibrated with a reference mirror. Additionally, we can slide all of the IR components away from the reactor for beam setup and alignment. When the

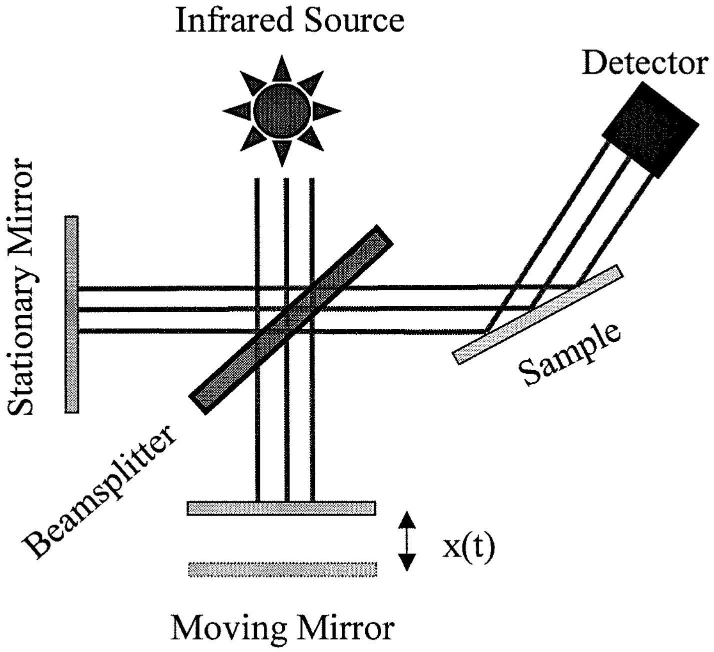

Figure 2.31: Schematic representation of a Michelson interferometer.

beam is removed from the reactor, alternate optical diagnostics can access the angled viewports as well. As an example, we have used a two-color pyrometer to estimate the sample and susceptor temperatures under these conditions.

The spectrometer was specifically ordered and configured for use with an external beam, which allows us to perform *in-situ* spectrometry (all components to the right of the beamsplitter in Figure 2.31 lie outside of the actual spectrometer). The external path of the IR beam is depicted in Figure 2.34. Downstream of the interferometer, the beam emerges from the black opening (upper-left) in the side of the Nicolet spectrometer. The beam is then reflected off three planar mirrors and into a parabolic mirror which focuses the beam onto the substrate through the adaptable windowed flange and zinc selenide window (discussed previously). Although not shown in the photo, the beam passes into the chamber, and onto the substrate. At the outlet of the reactor, Figure 2.35, the beam is again focused by a parabolic mirror onto a

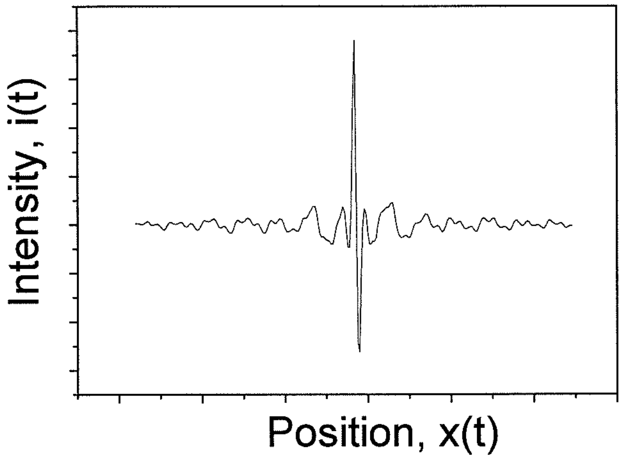

Figure 2.32: Typical interferogram.

Nicolet external FTIR detector. The interferometric data is collected by the PC, shown in Figure 2.30, where it is post-processed into an energy spectrum.

2.4.3 Thermocouples and Mass Spectrometry

Temperature sensing is integral to the reactor control operations. We have implemented Omega brand, K-type, inconel sheathed thermocouples in the face of the showerhead, the silicon oil passages, inside the inconel can, and inside the showerhead oven. Additionally, we have made K-type thermocouple beads using a spot welder for use in each of the three precursor ovens and the plumbing oven. Another of these homemade thermocouples has been epoxied into a 1/4 in stainless steel tube which was inserted through a vacuum feedthrough into the reaction chamber; see Figure 2.36. The feedthrough is attached to one of the straight-through viewports, which unfortunately, precludes any gas phase optical measurements while the probe is in use. The probe allows us to extend the thermocouple and contact the wafer *in-situ* and provides immediate information on the temperature of the wafer. Because of

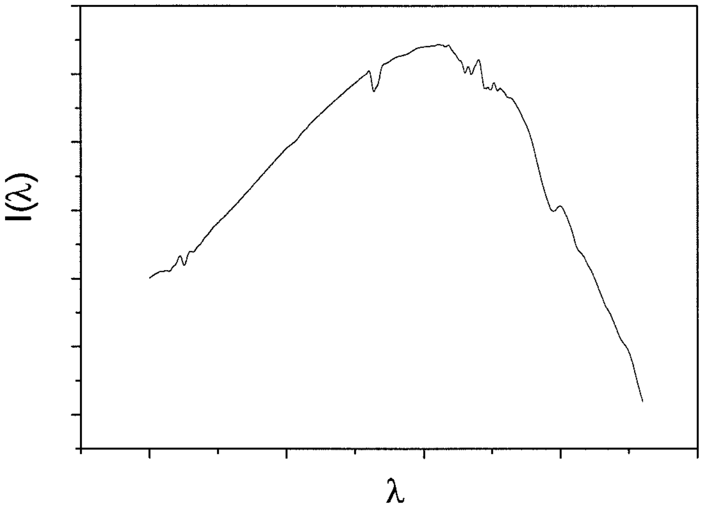

Figure 2.33: An example of an FTIR spectra from a blackbody source.

the intrusive nature of the probe, during growth runs it is retracted back against the vacuum feedthrough to prevent any disturbance to the reactive flow.

Also shown in Figure 2.36 is a sampling probe which we have used for mass spectrometry (MS) analysis. As with the thermocouple probe, the MS sampling probe is retracted from the flow during growth runs. The probe leads to an Inficon Quadrex 200 quadrupole mass spectrometer. Unfortunately, the precursors are too heavy for detection by the mass spectrometer (one tmhd ligand is $183amu$'s). Nonetheless, the mass spectrometer has been used to measure the nitrogen, oxygen, and helium partial pressures in the boundary layer during the growth and cooling procedures.

2.5 Conclusion

Although this concludes the section on the experimental apparatus involved with the CVD system, an additional diagnostic technique is presented in Chapter 5 along with a discussion of the associated hardware. Furthermore, the next chapter describes the

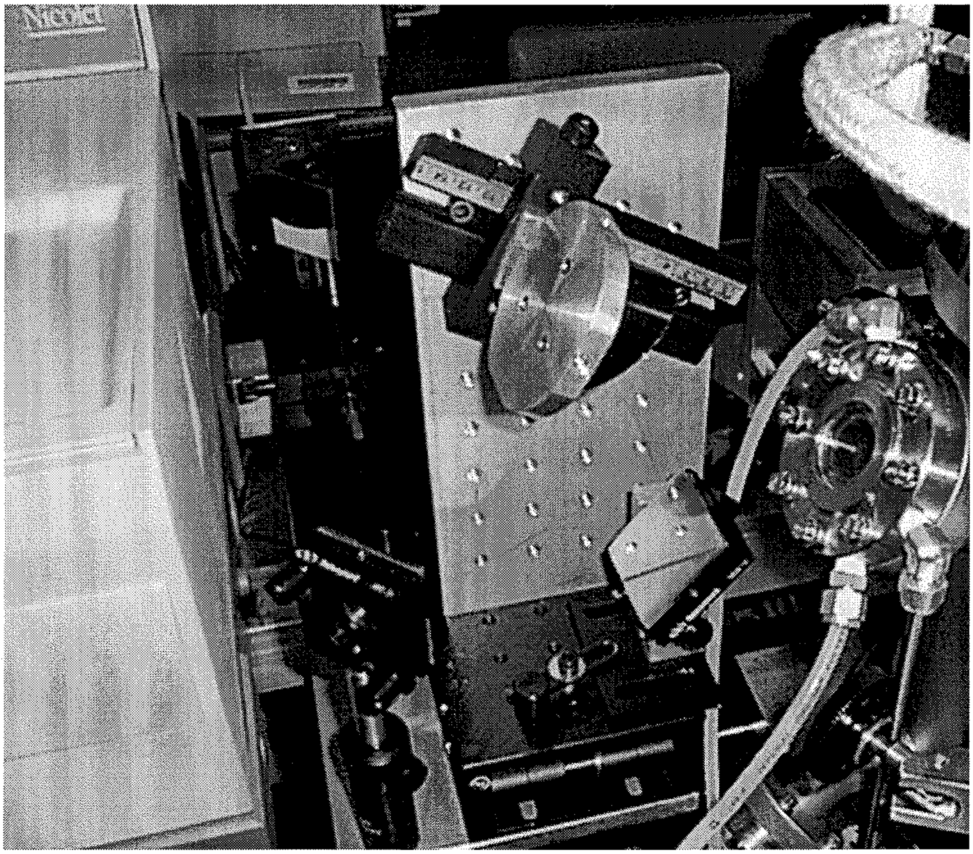

Figure 2.34: The infrared optical beam emerges from the Nicolet spectrometer (left side), reflects off three angled planar mirrors, and finally is focused into the reactor (right side) by a parabolic mirror.

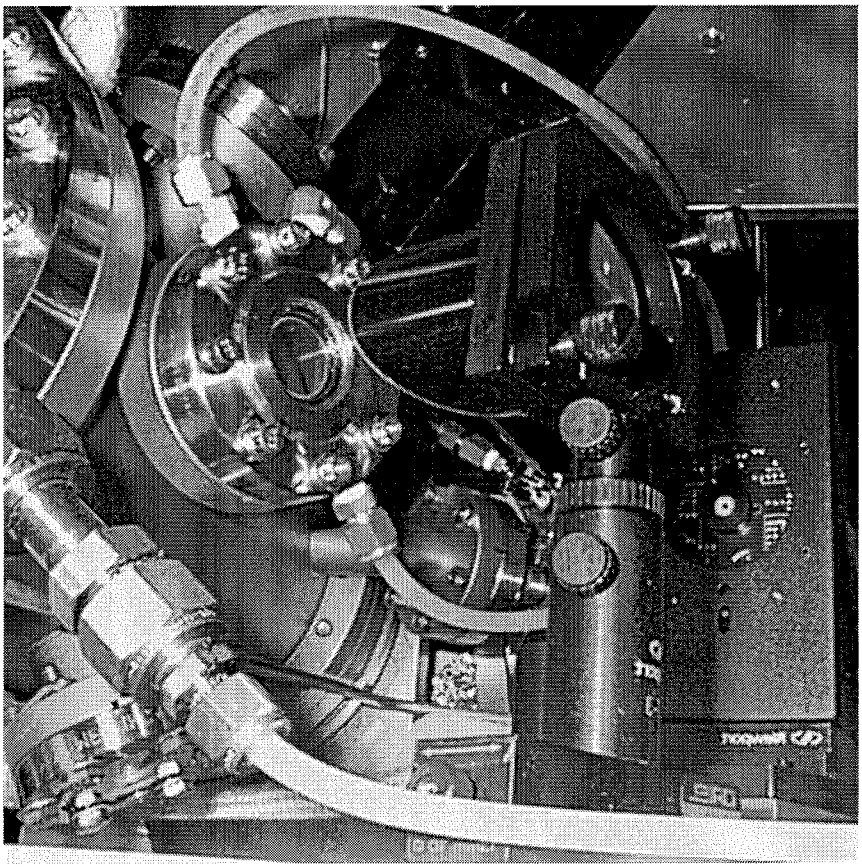

Figure 2.35: The infrared beam exits the reactor (left side) onto the parabolic mirror which focuses the beam down on the external detector (white circle right side).

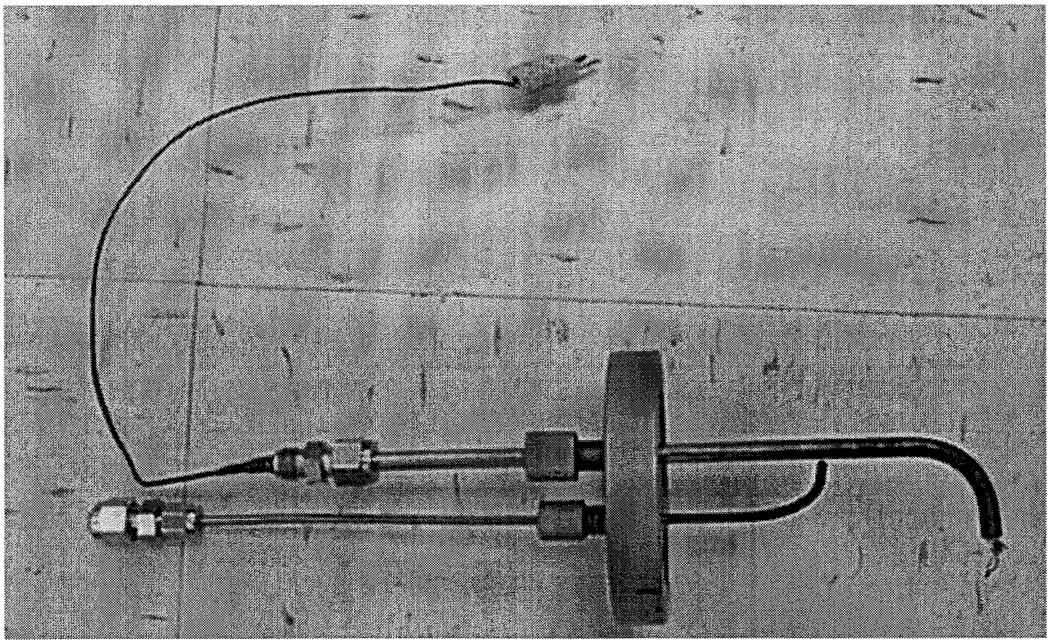

Figure 2.36: 3 3/8 in vacuum feedthrough which allows both translation and rotation of a thermocouple probe (1/4 in tube, top) and a mass spectrometry sampling probe (1/8 in tube, bottom).

operation of this reactor, often referring back to components discussed here.

A complete system for metalorganic chemical vapor deposition of YBCO has been modeled, designed, and fabricated. This CVD system functions as a flexible experimental test-bed reactor, permitting extensive in-situ investigations into YBCO thin film properties and growth processes. In addition, with minor modifications, the reactor presented is capable of growing and investigating virtually any metal-oxide thin film materials.

Chapter 3 CVD Procedure

Through our work with Superconductor Technologies Inc. (STI) [105], we have been the fortunate recipients of many tried and true operational instructions. MOCVD operational procedures have also been published extensively. Two excellent review articles which detail operating procedures for many research groups doing MOCVD of YBCO can be found in references [160] and [32]. As a result, the procedure presented below has been refined through many levels of trial and error both by our group and others around the world. In addition, many of the flow and growth conditions are a direct result of the extensive modeling discussed in Chapter 2 (Apparatus).

3.1 Preparations

3.1.1 Precursors

The choice to use tetramethylheptanedionate (tmhd) precursors came as a direct result of our interaction with STI, as that was their choice of precursor. All precursors and prepared substrates for this project were provided by STI.

Tmhd is a common ligand used to bond with large metal ions in order to make them volatile and suitable for vapor phase transport to reaction chambers. They are chemically known as 2,2,6,6-tetramethylheptane-3,5-dione or

$$(CH_3)_3CC(O)CHC(O)C(CH_3)_3 \ , \tag{3.1}$$

as illustrated in Figure 3.1. Readily available from commercial suppliers, Cu(tmhd)$_2$

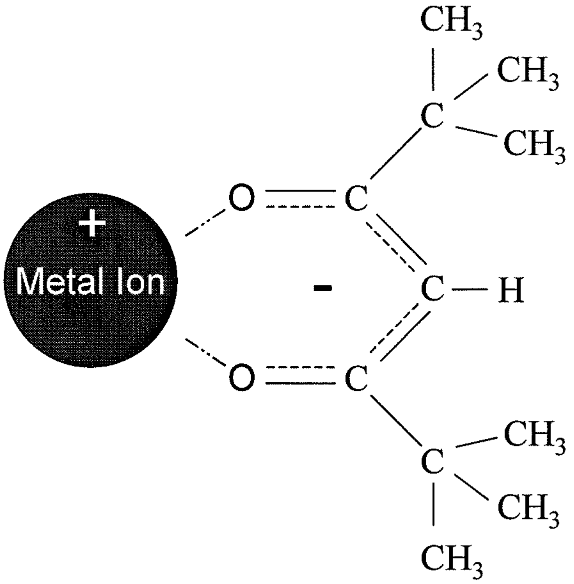

Figure 3.1: Schematic representation of one tetramethylheptanedionate ligand with a metal atom.

and Y(tmhd)$_2$ are the most common precursors in use for MOCVD of YBCO. Because the ligands are entirely organic (a partially oxidized hydrocarbon), they can be fully oxidized in the growth chamber with the end products being only carbon dioxide and water vapor; as a result, no potential film contaminants (other than carbon) are brought into the growth process [32].

There are considerable disadvantages to the use of Ba(tmhd)$_2$ for CVD processes. Unfortunately, Ba(tmhd)$_2$ is an oligomeric substance which exhibits limited volatility and decomposes significantly at the temperatures required for vaporization [39]. Unlike yttrium-tmhd and copper-tmhd, which sublime, barium-tmhd must be heated beyond the melting temperature in order to reach sufficient volatility for transport. The additional phase changes further accelerate the decomposition [32].

Chemically, barium-tmhd is commonly composed of oligomers of the form Ba$_x$(tmhd)$_{2x}$ (where x is an integer) [38]. As with all tmhd based precursors, barium-tmhd is very sensitive to water vapor [8]. In the presence of water, Ba(tmhd)$_2$ becomes

Table 3.1: Precursor material properties. Melting temperatures are courtesy of InorgTech [69]. Vapor pressure equations are based on temperature in K, and are courtesy of Tobaly et al. [144, 145].

Material	Melting Temp.	Vapor Press. (torr)	References
Ba(tmhd)$_2$	220°C	$10^{8.4-4710/T}$	[22, 38, 39, 41, 111, 144, 151, 159]
Cu(tmhd)$_2$	198°C	$10^{12.1-5720/T}$	[162, 144, 111]
Y(tmhd)$_3$	174-176°C	$10^{14.0-6110/T}$	[23, 111, 144, 162]

$Ba_5(tmhd)_5(OH)(H_2O)_3$ and $Ba_6(tmhd)_{12}(H_2O)_{13}$ among other hydrated oligomers [39, 151]. These hydrated species undergo degradation via an internal hydrolysis process [8]. However, with careful handling, commercially available Ba(tmhd)$_2$ can be used to achieve reproducible film growth of high performance YBCO [105, 161]. Typical material properties for all three tmhd based precursors are presented in table 3.1.

The upshot of the difficult material properties of Ba(tmhd)$_2$ and to a lesser degree Cu(tmhd)$_2$ and Y(tmhd)$_3$ is that we have had to be fastidious in our preparations of the sources for each growth run. In order to provide the maximum amount of surface area, the precursors are ground into a fine powder using a mortar and pestle. The powder is used to coat small stainless steel ball bearings [162, 163] which are then poured into the stainless steel bubbler (described in Chapter 2). The barium precursor is changed between each run, and hence the bubbler and ball bearings must be thoroughly cleaned between runs. The yttrium and copper bubblers last approximately ten runs before they need to be cleaned and repacked.

All of the materials are stored in a dry glovebox which is constantly purged with filtered nitrogen gas in order to prevent contact with any water vapor. All of the grinding and coating processes also take place inside of the glovebox.

In order to assure that all of the degraded precursor material from the previous run is removed from the ball bearings and bubblers, the cleaning process involves four steps. First, all components are soaked overnight and scrubbed with Alconox laboratory detergent. Everything is then rinsed several times with de-ionized water, and once with methanol. Finally, all the components are baked at 125 °C for at least 3 hours in order to remove any remaining water and methanol. While still hot from the baking process, the bubbler and ball bearings are returned to the glovebox for packing. Once the bubbler is packed it is reinserted into the gas handling system, and the entire system is evacuated to detect possible leaks.

3.1.2 Susceptor and Substrate

The untreated MgO substrates are purchased by STI from Superconductive Components Inc. as (100) single crystal wafers 5 mm in diameter, and 0.5 mm thick. The wafers are then subjected to STI's proprietary preparation technique which includes a solvent step followed by rinsing with de-ionized water, followed by a sputtering step followed by a high temperature anneal. The treated wafers are finally examined by AFM to verify that all of the miscut terraces are clean and smooth; see Figure 3.2 for an AFM image of a substrate prior to treatment and Figure 3.3 for an AFM image of the same substrate after treatment. At this point the samples are stored in a nitrogen environment (free from water vapor) at room temperature and pressure and shipped to Caltech. Once received, the substrates are stored in the glove box (mentioned in Section 3.1.1) until they are inserted into the CVD reactor for thin film deposition.

Before any growth experiment, the silicon carbide susceptor is soaked in 18:1 molar hydrochloric acid which has been diluted 1:1 with deionized water. This solvent process removes all previously deposited materials. The susceptor is then rinsed with deionized water, blown dry with nitrogen gas, and baked at 150°C for 30 minutes. The susceptor is then stored in the same nitrogen environment as the substrates.

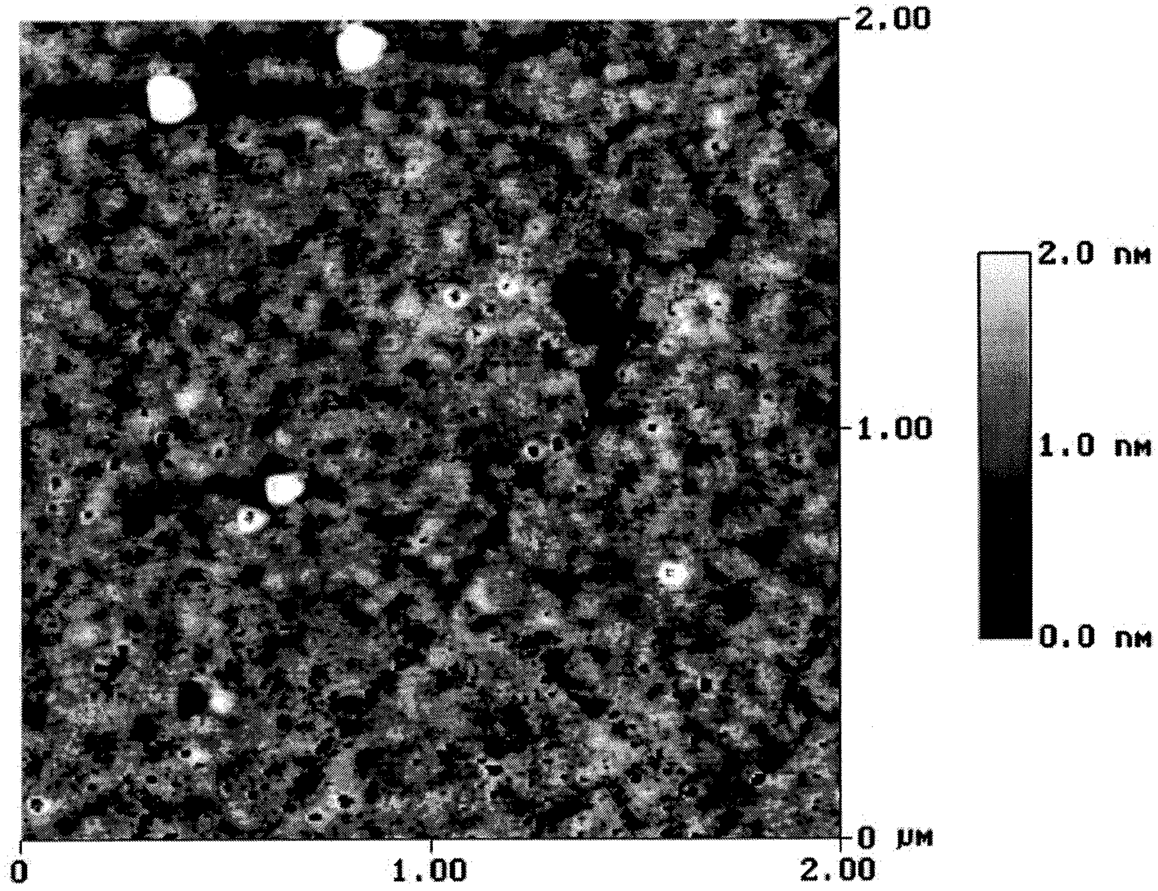

Figure 3.2: AFM image of an MgO substrate prior to STI's proprietary substrate preparation process.

3.2 Reactor Operation

Although the preparations require a minimum of two days, a thin film growth experiment is completed in one day, and analysis of the film often requires an additional day. The following section details the procedures involved in successfully operating the MOCVD reactor during a growth run.

3.2.1 Heating Up and Pumping Down

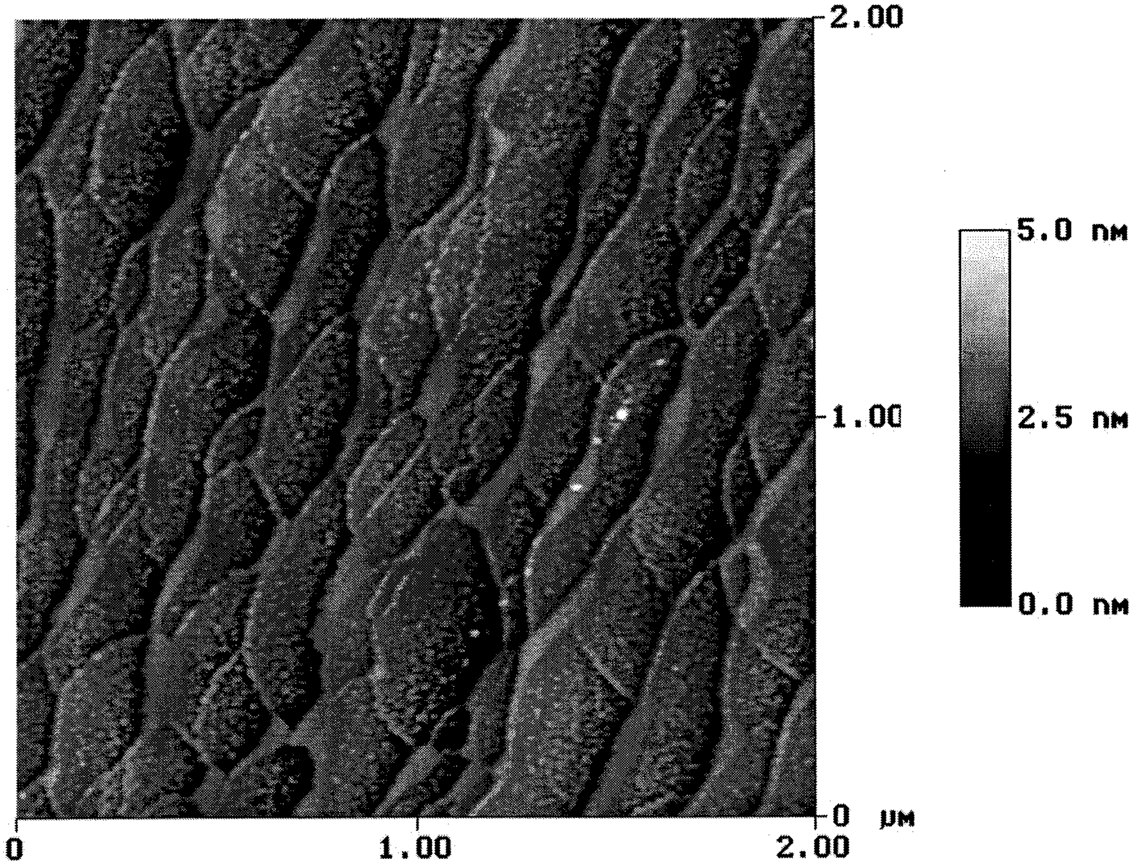

Figure 3.3: AFM image of the same sample presented in Figure 3.2 after STI treatment process.

On the morning of the growth run, the first step is to switch on all of the ovens and the oil bath. The time required to reach steady state is 2 – 3 hours for the bubbler ovens, which are set to temperatures of approximately 140 °C for the yttrium and copper bubblers, and 235 °C for the barium. The oil bath is heated to 250 °C, which is the maximum operating temperature of the silicon oil.

Unfortunately, prolonged exposure to high temperatures ($>$ 200 °C) causes the oil to degrade and polymerize. After a few months of heavy use the previously smooth flowing low viscosity oil (50 centistokes) becomes thick and rubbery. As a result, the oil requires periodic changing in order to continue trouble-free circulation.

The heated tubes, showerhead oven, plumbing oven, and variac controlled heat tapes are all set to maintain a consistent temperature of 255 °C. The thermal compromise inherent in the gas handling system involves the trade-off between preventing condensation of the precursors (especially the barium-tmhd because of its higher sublimation and melting temperatures) and the premature decomposition of the precursors. The precursors begin to shed their ligands at temperatures as low as 300 °C [23], hence only a narrow range of temperatures is available for successful transport of the vapor phase precursors to the reactor.

Next the reactor and gas handling system are pumped down and flushed with nitrogen. As mentioned in Chapter 3, a separate pump is used to evacuate the Six-way cross which houses the heaters and thermocouples. Without the cross pump a large pressure difference would build up between the cross and the reaction chamber, as the main vacuum pump evacuates the chamber. The six small holes of the gas bearing allow the pressure inside the cross to escape. In the case of a large pressure difference, the force of this escaping gas is so great that it can launch the susceptor and substrate off the inconel can and shatter the substrate.

Once the operating pressure of the chamber has stabilized at 10 torr, the cross pump is valved off and shut down. Helium is injected into the cross and hence through the gas bearing at a flowrate of 1 standard cubic foot per hour (SCFH).

Experience shows that if the cross pump is evacuating the cross and the wafer is at a temperature of 600 °C or higher, the heaters will burn through in less than 30 minutes. If the cross pump is not shut off, the helium for the gas bearing never reaches the susceptor, and in fact, the gases present in the reaction zone are pulled down into the can through the gas bearing. Since the reaction zone is usually oxygen rich, this inevitably results in a degradation of the heaters.

The chamber walls are protected with a shroud flow of nitrogen, between 1 and 2.5 slm, while both a dummy flow of nitrogen, approximately 3 slm, and the oxygen flow, $2-3.5$ slm, are established inside the reaction chamber. To initiate film growth, the dummy flow is exchanged with the live flow (containing unreacted precursors) as mentioned in Chapter 2.

With the flowrates and pressure inside the chamber at operating conditions, the reactor can be heated to the growth temperature. The DC power supplies are commanded by the data acquisition PC, and we use a voltage ramp to ensure a smooth steady heating rate. Typically the ramping time from room temperature to growth temperature is 1800 seconds. Once the heaters have reached the desired voltage and power levels, the chamber and all attached components require approximately one hour to thermally stabilize. When the wafer temperature has leveled off, the heater control loop is engaged with a setpoint based on thermocouples inside of the inconel can. FTIR results presented in Chapter 4, as well as use of the thermocouple probe, have enabled us to correlate can temperature with growth temperature.

The voltage corresponding to growth temperature varies depending on the age of the heaters. While a new heater requires 50 Volts to reach a wafer temperature of 800 °C, a heater nearing the end of its lifespan requires 75-80 Volts to reach the same temperature. We have observed that the heaters deteriorate after prolonged exposure to high temperatures through a combination of oxidation and sublimation. Each set of heaters will last for six to ten growth runs at growth temperatures above 750 °C; at lower temperatures, the heaters last considerably longer.

3.2.2 Ultraviolet Spectroscopy

As the wafer is coming to thermal equilibrium, the bubbler temperatures should also have leveled off. Before opening the bubblers, a set of ultraviolet reference data is required for composition control. The reference data is the transmitted intensity through the optical cell with no precursor materials present, only pure carrier gas.

The measured absorption for each precursor gas is a ratio of the raw transmission intensity divided by the initial reference data.

In order to minimize inaccuracy with the reference data, growth conditions must be maintained during the reference scan (plumbing oven temperature between 230-255°C and a pure nitrogen flow rate of 0.2 slm through the cell from the bubbler bypass line). In addition one channel is reserved as the control and does not pass through an optical cell. This "master channel" allows the control software to account for lamp drift (UV illumination) and solarization of the optical fibers. The master channel also requires an initial reference scan. The measured absorption for each material is multiplied by a ratio of the master channel reference data divided by the current master channel data.

$$Absorption = \frac{current\ transmissivity}{reference\ transmissivity} \times \frac{master\ reference}{master\ current} .$$

The reference scans for all 4 channels are captured simultaneously.

Once the reference UV data is captured, the nitrogen which is flowing through the bubbler bypass line is switched off, and the bubbler valves are opened very slowly. The bubblers are sealed before being heated to temperatures exceeding 130 °C, which creates a pressure difference of more than 100 torr between the inside of the bubbler and the vacuum lines. If the bubblers are not opened judiciously, a rush of gas escapes into the stainless steel tubing which can carry solid precursor powders out of the bubblers and result in contamination of the plumbing lines and optical cells.

After the bubblers have been opened, a small flow of nitrogen (typically 0.025 slm) is passed through the bubblers to monitor precursor concentrations as the bubblers reach operating temperature. Once the bubblers and the wafer have reached thermal equilibrium, the ultraviolet stoichiometry control loop is switched on.

Typical absorbance spectra for $Y(tmhd)_3$, $Ba(tmhd)_2$, and $Cu(tmhd)_2$ are shown

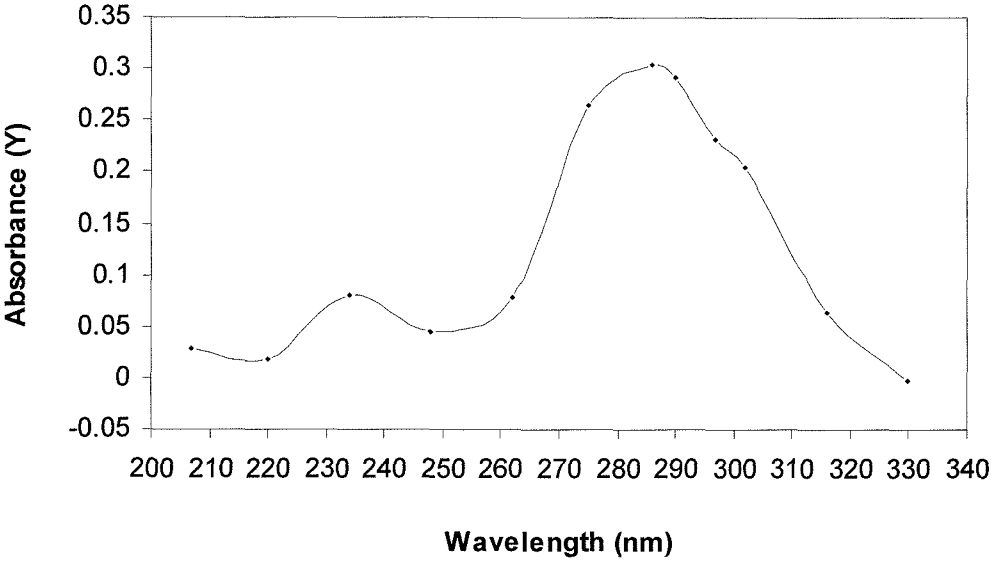

Figure 3.4: Ultraviolet absorbance spectrum for vapor phase yttrium precursor in a nitrogen carrier gas.

in Figures 3.4, 3.5, and 3.6 respectively. The control loop is wrapped around the frequency closest to the peak of each material. Yttrium absorbance is monitored at 286 nm, while barium is at 290 nm, and copper is at 297 nm.

Setpoints for the fraction of yttrium going to the reactor, X_Y, the fraction of barium going to the reactor, X_{Ba}, and the total amount of precursors (micromoles of metal per minute) are chosen based on the desired film composition. The fraction of copper precursor going to the reactor is calculated from the following formula:

$$X_{Cu} = 1 - X_Y - X_{Ba} \ . \tag{3.2}$$

Results of the correlation between the gas phase stoichiometry and film stoichiometry are presented in Chapter 4.

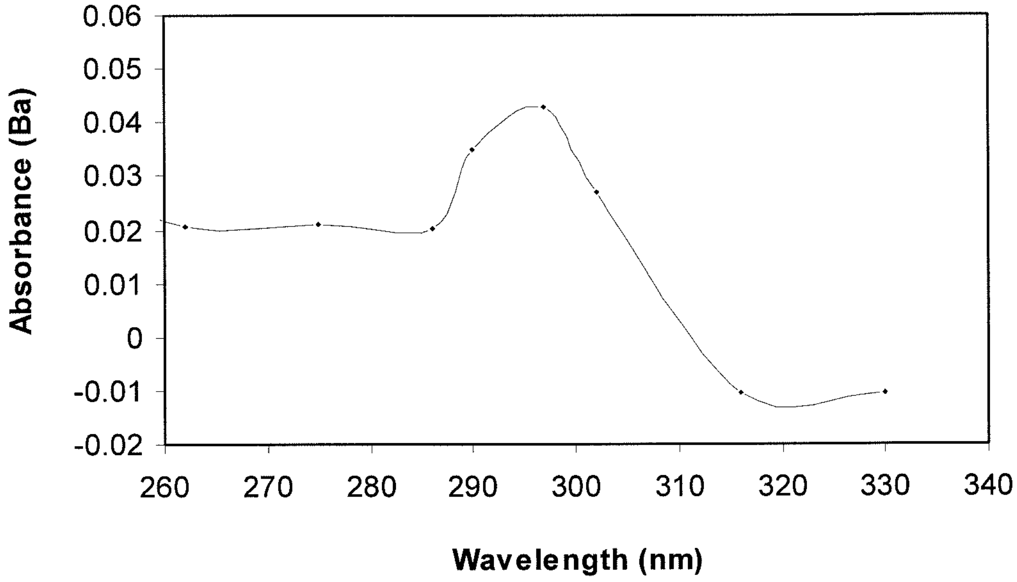

Figure 3.5: Ultraviolet absorbance spectrum for vapor phase barium precursor in a nitrogen carrier gas.

3.2.3 Film Growth

Downstream of the optical cells, the precursor flows are combined with a bulk flow of nitrogen inside a mixing manifold. The bulk nitrogen flow is used to maintain a steady 40 : 60 oxygen to nitrogen ratio inside the reaction chamber. When all the temperatures and flows have stabilized (and the particle trap is full of liquid nitrogen), growth mode is engaged. The dummy nitrogen is switched to the vent line, while the precursors and the bulk nitrogen flow are directed into the reaction chamber. Film growth lasts for a preset time (usually 60, 90, or 120 minutes) or until the barium precursor has decomposed to a level where further increases in bubbler nitrogen flowrate do not translate into an increased metal flowrate.

We operate the bubblers in the mass-transport limited regime. Hence the concentration of precursor in the optical cells is relatively independent of flowrate through the cell (and bubbler). When the barium precursor begins to degrade, the concen-

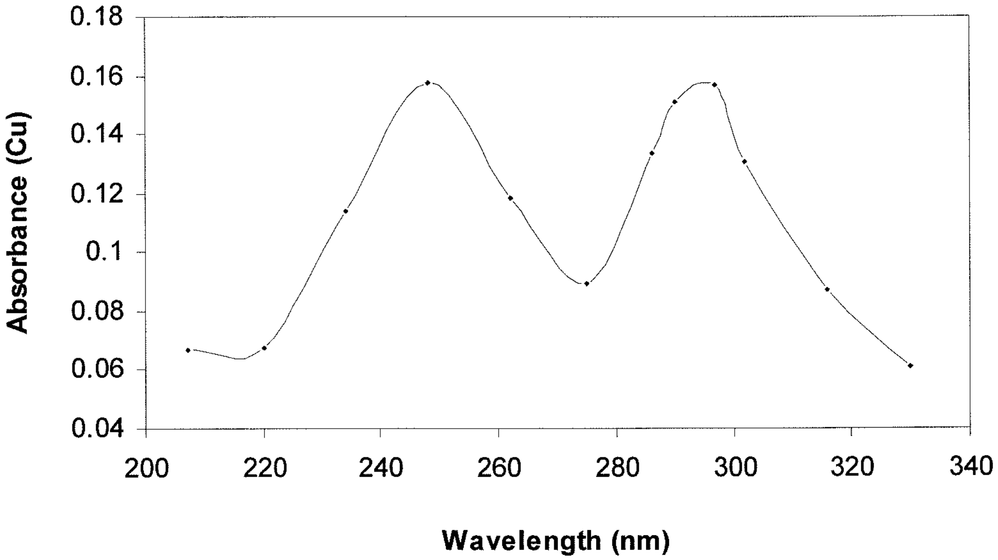

Figure 3.6: Ultraviolet absorbance spectrum for vapor phase copper precursor in a nitrogen carrier gas.

tration in the optical cells diminishes, and after a certain point, further increases in flowrate do not deliver enough barium to the reaction chamber. The barium precursor typically lasts from 1 – 3 hours depending on bubbler temperature, and bubbler packing quantity.

3.2.4 Cool Down

At the conclusion of the film growth, the dummy nitrogen flow is once again introduced to the reaction chamber. The bulk nitrogen flow and precursors are ejected through the vent line. The dummy nitrogen flow is tapered off so that the YBCO film cools down in a nearly pure oxygen environment. There are trace amounts of helium from the gas bearing and nitrogen from the shroud flow in the boundary layer surrounding the film. To insure proper oxygenation of the YBCO, the heater voltage is ramped down so that the wafer takes a minimum of 30 minutes to reach 450 °C.

At that point the heaters are ramped off quickly, and the chamber is brought up to atmospheric pressure while maintaining the oxygen environment. Several hours later, once the wafer is near room temperature (less than 100 °C), the film can be removed from the chamber and analyzed.

3.3 Film Characterization

Both before and after growth, the substrate is weighed on a ±10 microgram scale. The difference is the weight of the YBCO film, which when divided by the density of the film, $\rho_{YBCO} = 6.635\,\mathrm{g}\,/\,\mathrm{cm}^3$ and the surface area of the film, yields the film thickness.

$$thickness = \frac{Mass}{\rho_{YBCO} \times Area} \tag{3.3}$$

Thicknesses are typically between 200 nm and 500 nm.

3.3.1 Rutherford Backscattering Spectrometry

Most of our films were also analyzed using Rutherford Backscattering Spectrometry (RBS) in a facility maintained at Caltech by the Nicolet group [107]. RBS involves bombarding the films with a charged beam of He^{2+} alpha particles carrying a kinetic energy of 2MeV. The energy of those particles which are reflected from the film contains information about what materials are present, and the densities (thicknesses) of those materials. As such RBS provides information on the metal stoichiometry and thickness of our films. In addition, RBS spectra can yield depth specific stoichiometry, providing compositional feedback on the growth process in a time-based manner. Because the incident helium ions are most readily reflected by large, heavy

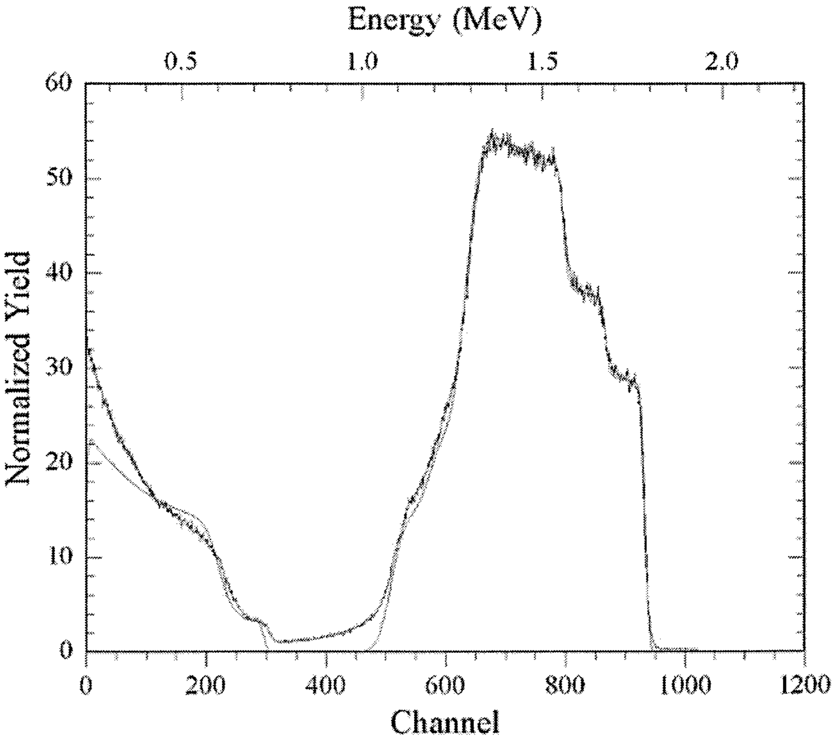

Figure 3.7: A Rutherford Backscattering Spectrum of a YBCO film (jagged line) is shown along with simulation results (smooth line).

atomic nuclei, RBS is most sensitive to metallic species, which makes it inappropriate for determining oxygen concentrations in the films.

For each analysis, the RBS is first calibrated with a special sample containing thin layers of gold, rhodium, and cobalt on silicon. Reference backscattering energies for the gold, rhodium, and cobalt are used to establish the amount of energy present in each channel (note the dual x-axes of Figure 3.7). The energy spectra were then modeled with a software package developed at Cornell University entitled RUMP [36, 37]. The program is used to deconvolute the RBS spectra by a process of successive simulations [125]. A sample spectra and the matching RUMP fit are depicted in Figure 3.7. This film, grown on 3-21-00, corresponds to a RUMP simulation of a film with composition of $Y_1Ba_{1.56}Cu_{2.85}O_{7-\delta}$ and a thickness of 0.276 μm.

3.3.2 Other Analytical Techniques

On occasion we sent films to STI for analysis by Energy Dispersive X-ray analysis (EDX) [124, 54] and X-Ray Diffraction analysis (XRD). The EDX system is associated with their Scanning Electron Microscope (SEM), and collects x-rays generated by the microscope's electron beam. The energies of the x-rays are explicitly related to the energy shell levels of the materials present in the film, hence EDX is used primarily for compositional analysis. However, EDX only provides aggregate information, averaging across an approximately 1 μm sized exposure area. Because the electron beam penetrates the film to a depth of nearly 1 μm, the x-rays retrieved include information about the substrate as well as the film. Because oxygen is present in both the film and the substrate, EDX like RBS is not an appropriate technique for determining the oxygen content of our films.

Analysis by XRD [31, 54, 137] provides information on the crystal structure of our films. XRD results indicate which phases are present in the Y-Ba-Cu-O system, and what the lattice spacings are for those phases. Cava *et al.* [26] provided a widely accepted correlation between c-axis length and oxygen content in YBCO films (which is discussed further in Chapter 5). As a result, XRD analysis is the most appropriate technique for determining the oxygen stoichiometry. The samples are analyzed in a $\Theta - 2\Theta$ diffractometer with CuKα generated radiation incident with a wavelength of 1.54056 nm.

Lastly, several of our films were analyzed with Atomic Force Microscopy (AFM) [65]. AFM uses a sharp silicon tip less than 100Å in diameter to probe the surface of the films. The tip is attached to the end of a cantilever, and the van der Waals force between the YBCO and the tip cause the cantilever beam to bend and deflect. The deflections are measured by a computer which translates them into an image of the surface.

The results from all of the analytical techniques are presented in Chapter 4. Additionally, other film characterization data is presented which unlike the RBS, EDX, XRD, and AFM techniques presented above, was not performed as part of our routine procedure.

Chapter 4 MOCVD Results and Discussion

4.1 Introduction

As mentioned in the preceding chapters, we have used our MOCVD reactor to grow many different thin films and investigate both the film properties and the growth processes. Among the films we have grown are YBCO and the individual metal oxide films, yttrium oxide (Y_2O_3), barium oxide (BaO), and both forms of copper oxide (Cu_2O and CuO). Film characterization results will be presented from RBS, XRD, XPS, and electron microprobe analyses.

The growth process has been investigated with *in-situ* FTIR and CGS (presented in Chapter 5), and chemical modeling. The growth chamber has been characterized for flow conditions with mass spectrometry, and for thermal conditions with pyrometry, FTIR, and thermocouples. Film growth results are applied to a gas phase and surface chemistry model in order to determine sticking coefficients for yttrium, barium, and copper onto YBCO.

4.2 Reactor Characterization

4.2.1 Chemical Purity

Our first film grown was yttrium oxide on silicon. The film was characterized with X-Ray Photoelectron Spectrometry [19] as presented in Figure 4.1.

XPS involves bombarding the film with high energy x-rays. The materials present in the film will absorb the x-rays and emit electrons from each energy shell. These electrons are analyzed based on their kinetic energy. The difference between the kinetic energy of the incident photons and the kinetic energy of the liberated electrons is the binding energy of the electrons. The binding energy can be correlated with specific materials (and their shell levels), and in some cases can yield information about the nature of the chemical bonds present in the material.

Figure 4.1 is worthy of mention because of the lack of contaminants present in the film. All of the peaks are accounted for by yttrium, oxygen, and silicon. The careful reader will also notice the presence of a carbon peak. Adventitious carbon is inevitably present on all samples. Concerns had been raised about the possibility of contamination by the copper showerhead or inconel can during the design phase of the reactor. Fortunately, the absence of any iron, nickel, copper, or tellurium in the yttrium oxide film precludes the possibility of metal contaminants in our films.

4.2.2 Film Uniformity

The next two films grown in our system were copper oxide and barium oxide. RBS results of the barium oxide film are presented in Figure 4.2. The energy level at the leading edge of the peak corresponds to barium (1.785 MeV versus 1.784 MeV predicted theoretical value). Illustrated in the figure are the endpoints for calculating the full width half maximum (FWHM) energy levels for each scan, $\Delta E_{edge} = 0.209\,\mathrm{MeV}$ and $\Delta E_{center} = 0.204\,\mathrm{MeV}$. The film thickness, t, can be calculated from the following formula [107]:

$$t = \frac{\Delta E}{[\varepsilon_0]} \times \frac{1}{N} \tag{4.1}$$

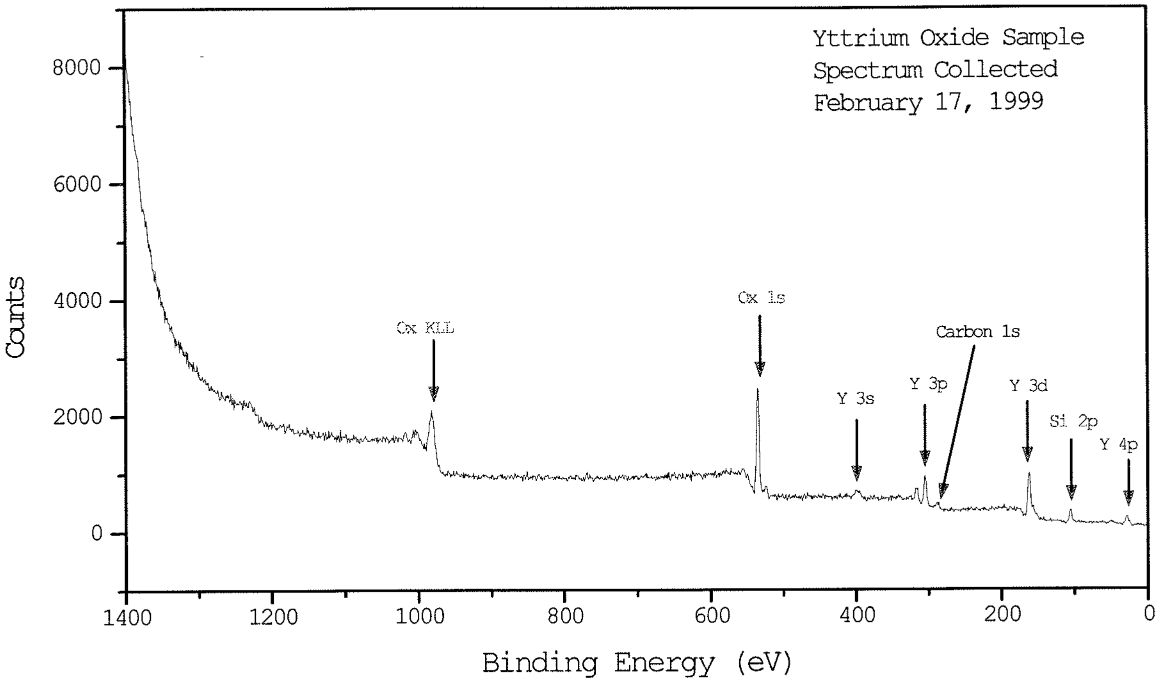

Figure 4.1: X-ray Photoelectron Spectrometry results of Y_2O_3 film grown on a silicon single crystal wafer.

where $[\varepsilon_0]$ is the ^{4}He stopping cross section factor, $229.1 \times 10^{-15}\,\mathrm{eV\,cm^2}$ for barium under our experimental conditions, and N is the number density of barium in the film, $22.39 \times 10^{21}\,\frac{\text{atoms}}{\text{cm}^3}$. The result is a thickness of 407 nm at the edge, and 398 nm in the center. Uniformity is achieved to within 2%, which compares well with the best commercial MOCVD reactors. Published values for optimum thickness uniformity are typically $\sim$ 1% [146].

4.2.3 The Boundary Layer

As mentioned in the discussion about the apparatus (Chapter 3), we made use of mass spectrometry to sample the gas nearest to the substrate. Two goals were accomplished with this investigation.

First the stabilizing effects of thermal diffusion and natural convection were con-

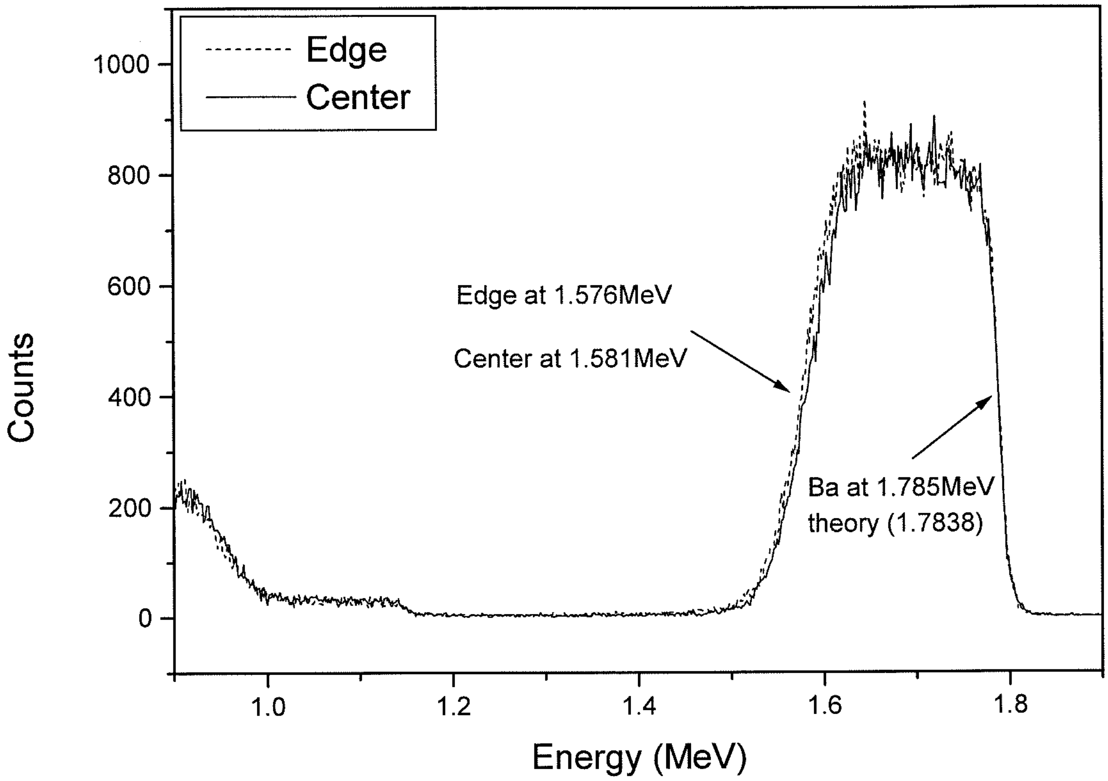

Figure 4.2: RBS results of a barium oxide film grown on a silicon substrate. Film thickness uniformity is illustrated by the similar widths of the two peaks.

firmed, Figure 4.3. With oxygen flowing at 5 slm, and nitrogen coming only from the shroud flows and window purge slows, the mass spectrometer provides a local measurement of oxygen percentage across the wafer. Note that at low temperatures, the flow is non-uniform allowing quite a bit of the shroud flow to enter the boundary layer from the perimeter. However, at growth temperatures (wafer $\geq$ 600 °C) the flow is much more uniform, and there is less nitrogen entering the boundary layer.

Mass spectrometry was also used to verify the operating conditions for growth and cool down at the wafer. At a chamber pressure of 10 torr, empirical evidence from STI indicated that a 40% oxygen environment (or slightly higher), was most appropriate for growth, while a 90% oxygen environment is required for oxidation

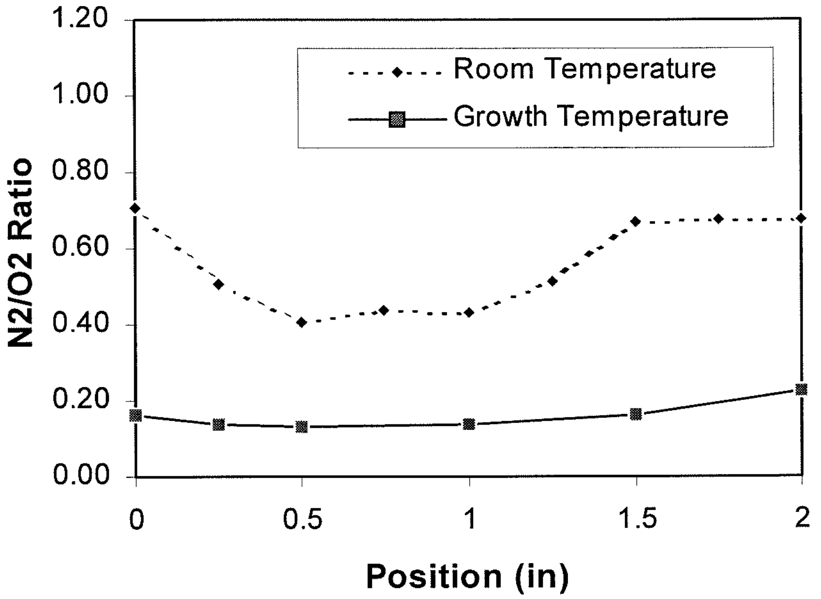

Figure 4.3: Mass spectrometry results are presented which demonstrate the thermal effects of heating the can (wafer temperature = 775 °C). Position is measured across a 2 inch diameter wafer, hence $x = 1.0$ is the centerline.

of the film. STI uses flowrates of 4 slm of O_2 and 6 slm of N_2 during their film growth. Our modeling results indicated that only half the total flowrate through the showerhead was required for the proper fluid mechanics, and since total flow is lower, precursor concentration and deposition rate could potentially be higher. As such, initial tests were carried out with 2 slm of O_2 and 3 slm of N_2. The mass spectrometry results presented below, Figure 4.4, show that the proper growth conditions were in fact achieved with flowrates of 3.5 slm of O_2 and 3.5 slm of N_2.

Similar results were attained for the cool-down conditions. Despite initial estimates of 5 slm total flow through the showerhead, proper conditions required 8 slm of O_2 through the showerhead. Similar to Figures 4.4 and 4.3, the graph in Figure 4.5 represents the ratio of N_2 to O_2 versus position on a 2 inch diameter substrate, where $x = 1$ in corresponds to the center of the wafer.

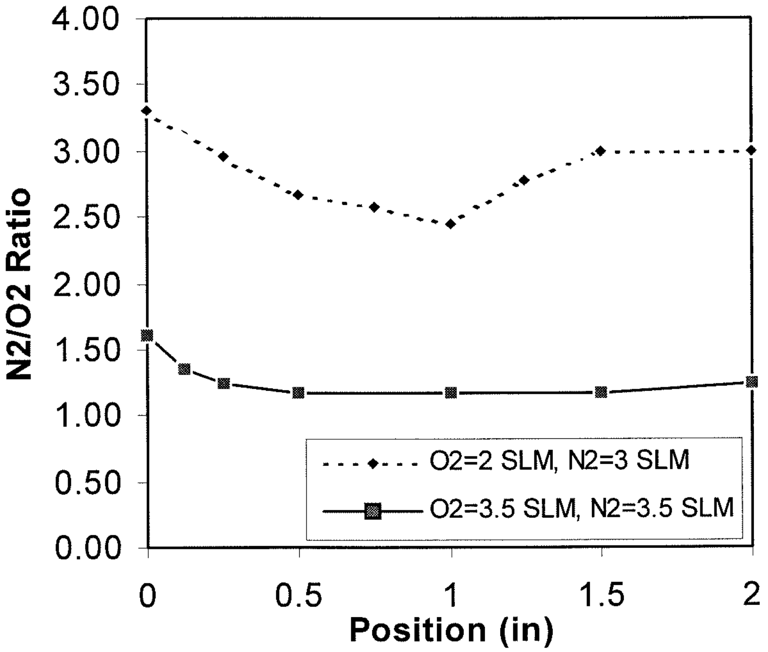

Figure 4.4: Mass spectrometry results for two different growth conditions.

4.2.4 Temperature Measurement

FTIR spectrometry was used to measure the temperature of the MgO substrates. The experimental setup is depicted in Figure 4.6. Published literature on the infrared reflectance spectra of MgO indicates a shift in the Restrahlen band with temperature [71]. A specially designed, thermally uniform, calibration oven was constructed to collect IR spectra from an MgO sample held at constant temperature [52]. The results of these experiments are presented in Figure ??. By comparing the half-height wavenumber for an MgO sample at any temperature with the reference values presented in Figure ??, we can calculate the actual sample temperature to within 10 degrees Kelvin.

The FTIR results together with the thermocouple probe (presented in Chapter 2) allowed us to calibrate the growth temperature of the wafer for a given heater power, can thermocouple reading, and given flow condition. We typically notice a

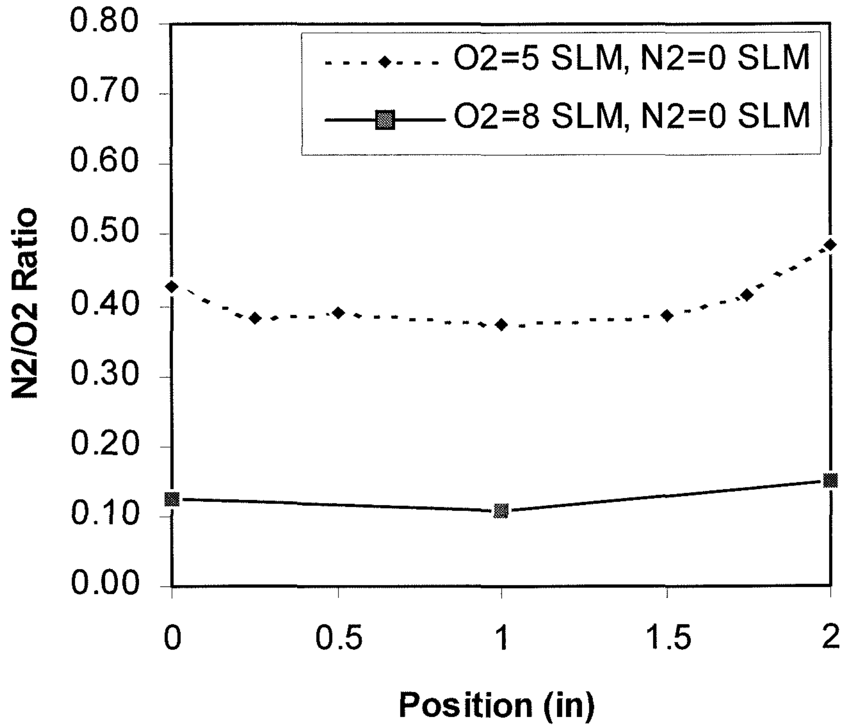

Figure 4.5: Mass spectrometry results for two different cool down conditions.

temperature difference of 250 °C between the inside of the can and the wafer when the wafer is at a temperature of 800 °C.

Additional FTIR results were gathered during a few of our growth runs. Noise in the spectra is inversely proportional to the number of scans collected; however, each scan requires approximately 7 seconds to acquire. As a compromise between noise and timeliness, we chose to collect 100 scans for each spectrum. Spectra from 12-17-99 are presented in Figure 4.8. The top line, 5400 s (relative heights are from the right-hand side of the plot), was gathered from the bare MgO wafer prior to growth, sample temperature ~ 150 °C. The second line, 10300 s, was gathered from the bare MgO wafer at the onset of YBCO film growth, sample temperature 625 °C. Growth proceeded for one hour, concluding at 13900 s. A closer look at the Restrahlen band (inset of Figure 4.8) reveals the gradual flattening of this feature as the MgO

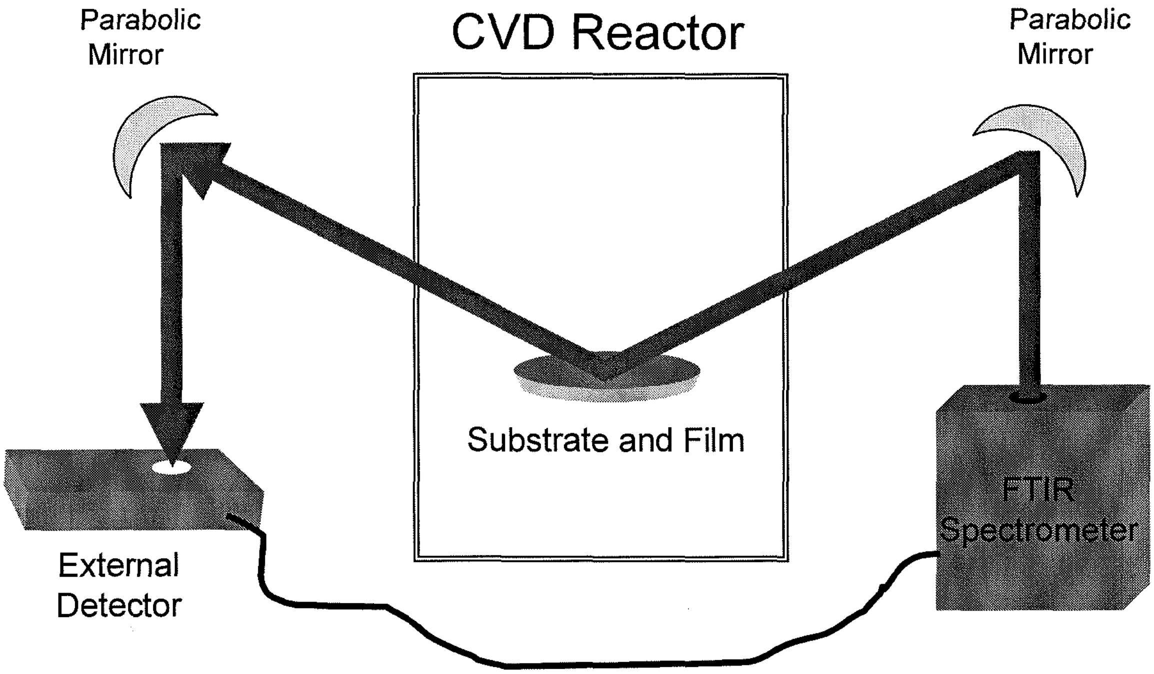

Figure 4.6: A schematic representation of FTIR analysis of MgO substrates and YBCO films *in-situ*.

is covered with the YBCO. For thicker films (> 400 nm) the feature is eliminated altogether.

4.3 YBCO Film Growth Results

Table 4.1 presents the results of our most successful growth experiments. The nature of our metalorganic precursors hinders the preparation of films with precisely reproducible compositions [160]. Nonetheless, many of our films fall within the desired stoichiometry for superconductivity.

Doudkowsky *et al.* [40] found in their study of YBCO by MOCVD that films with ratios of $2.5 < \frac{\mathrm{Cu}}{\mathrm{Y}} < 3.0$ and $0.97 < \frac{\mathrm{Ba}}{\mathrm{Y}} < 3.0$ would transition to superconductivity at temperatures between 70K and 90K. In other words, films with stoichiometries

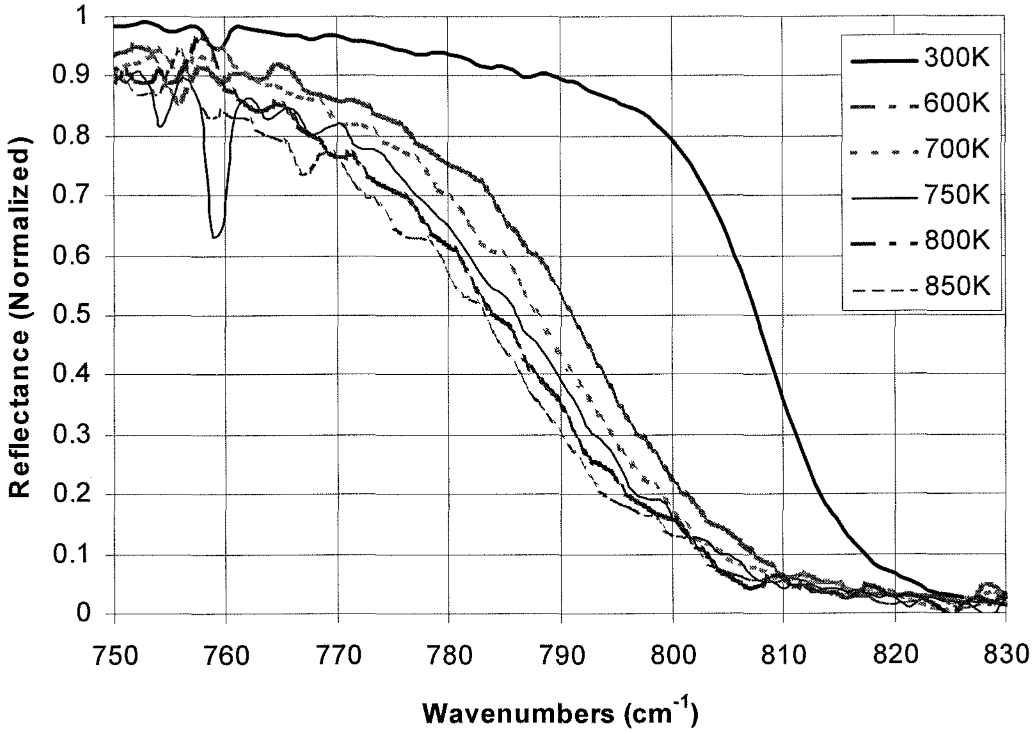

Figure 4.7: A shift in the Restrahlen band of the infrared transmission spectra is observed for MgO with variations in temperature.

in the following range,

$$0.142 < \mathrm{Y} < 0.224, \quad 0.195 < \mathrm{Ba} < 0.462, \quad 0.384 < \mathrm{Cu} < 0.604\ , \tag{4.2}$$

would eventually superconduct. In an earlier study Zhao *et al.* found the occurrence of superconductivity for films in the range of $3.0 < \frac{\mathrm{Cu}}{\mathrm{Y}} < 3.2$ and $1.1 < \frac{\mathrm{Ba}}{\mathrm{Y}} < 2.2$ or

$$0.156 < \mathrm{Y} < 0.196, \quad 0.207 < \mathrm{Ba} < 0.355, \quad 0.484 < \mathrm{Cu} < 0.604\ . \tag{4.3}$$

As such, between 5 and 8 of the films presented in table 4.1 should be superconducting. In fact, optimal stoichiometries for (Y, Ba, Cu) are presented by several

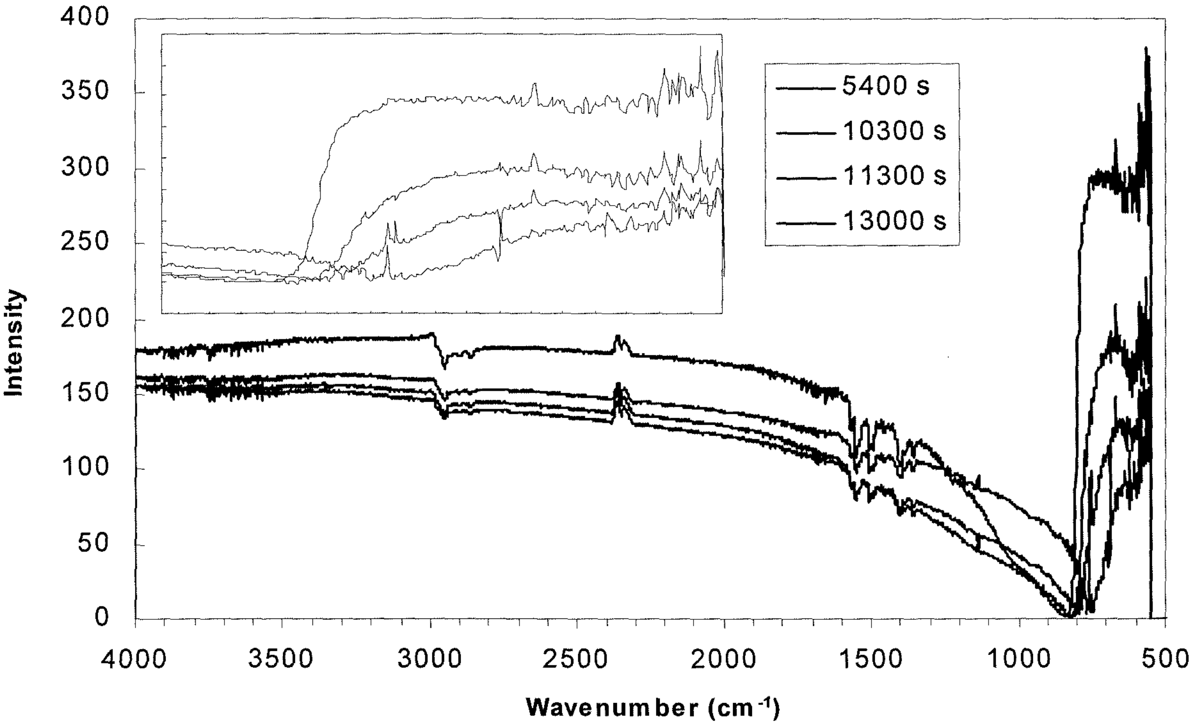

Figure 4.8: FTIR spectra from growth run on 12-17-99. Inset shows the diminishing height of the Restrahlen band.

research groups in table 4.2. It is worth noting that the ideal stoichiometry is not actually 1:2:3, but one that is slightly barium deficient [159].

Also of interest is the correlation between gas phase stoichiometry and film stoichiometry. Musolf and Smith [105] found that in order to achieve a 1:2:3 stoichiometry (0.167 : 0.333 : 0.5), gas phase stoichiometry of 0.3 : 0.4 : 0.3 was required in their horizontal flow MOCVD reactor. Our results of approximately 0.25 : 0.5 : 0.25 are similarly biased toward barium and yttrium, and this will be discussed further in the chapter.

4.3.1 X-ray Diffraction Results

Table 4.1: Growth run results are presented with input (gas phase) and output (film) stoichiometry. Results in italics are from EDX, while all others are based on RBS analyses. See text for discussion.

Date		Gas			Film		Thickness	Temp
Grown	Y	Ba	Cu	Y	Ba	Cu	μm	°C
6/3/99	0.197	0.420	0.383	0.380	0.263	0.357	0.321	675
8/10/99	0.197	0.420	0.383	*0.098*	*0.287*	*0.615*	0.544	675
8/24/99	0.190	0.580	0.230	*0.225*	*0.105*	*0.670*	0.318	675
9/1/99	0.190	0.580	0.230	0.195	0.329	0.476	0.496	675
9/28/99	0.200	0.590	0.210	0.146	0.348	0.505	0.308	700
9/30/99	0.250	0.510	0.240	0.172	0.345	0.483	0.365	700
10/15/99	0.250	0.490	0.260	0.184	0.208	0.608	0.585	700
11/19/99	0.270	0.530	0.200	0.190	0.149	0.661	0.592	600
12/17/99	0.200	0.590	0.220	0.180	0.281	0.539	0.240	625
1/3/99	0.240	0.510	0.250	0.357	0.227	0.416	0.445	675
1/13/00	0.180	0.550	0.270	0.213	0.250	0.537	0.293	725
1/28/00	0.150	0.580	0.270	0.174	0.209	0.616	0.223	760
3/21/00	0.200	0.510	0.290	0.185	0.288	0.527	0.276	800
3/27/00	0.200	0.510	0.290	0.197	0.314	0.489	0.305	760
4/5/00	0.200	0.510	0.290	0.262	0.312	0.426	0.369	800
	Typical	**STI**	**Film**	**0.173**	**0.285**	**0.542**	**0.700**	**800**

Table 4.2: Optimal stoichiometry as presented in the literature from several experimental studies.

Reference	Y	Ba	Cu
[40]	0.179	0.339	0.482
[66]	0.187	0.280	0.533
[92]	0.167	0.267	0.566
[100]	0.200	0.270	0.530

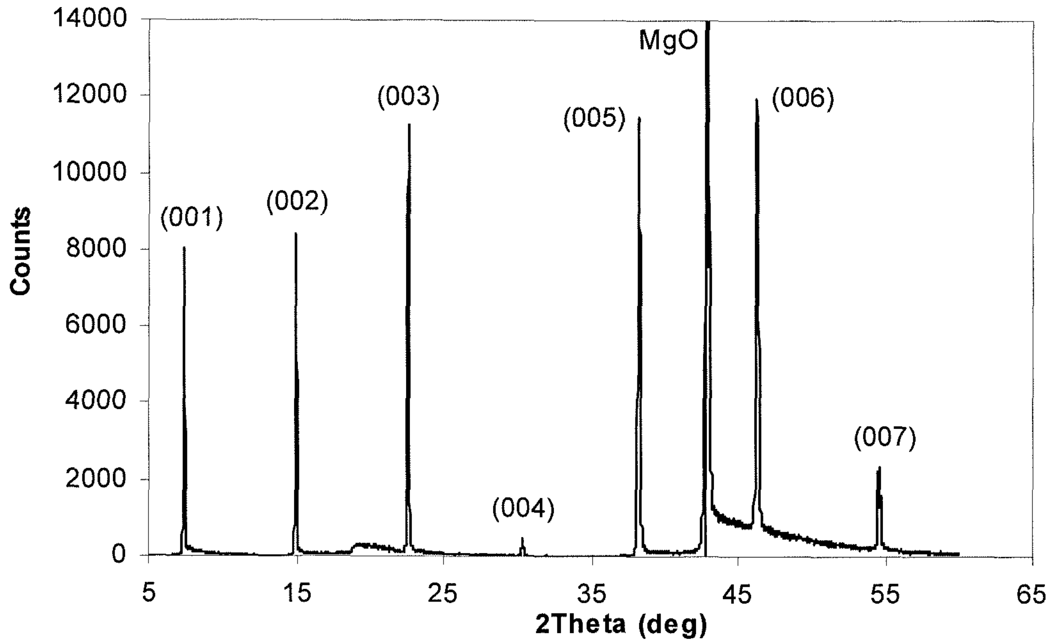

Figure 4.9: X-ray diffraction analysis before annealing indicates purely c-axis YBCO on MGO for film from 03/21/00.

X-ray diffraction analyses were carried out on the films which were most closely matched to published optimal stoichiometries. As an example, we will consider the film grown on 3/21/00. Figure 4.9 illustrates the XRD results with all of the peaks indexed to (00*l*) reflections of c-axis oriented $YBa_2Cu_3O_{7-\delta}$ plus the (001) reflection of the single crystal MgO substrate. The rocking curve analysis of the (005) peak, Figure 4.10, shows a full width half maximum (FWHM) value of 0.425°, which compares favorably with the published values of $0.3° < \text{FWHM} < 0.4°$ for c-axis oriented orthorhombic phase $YBa_2Cu_3O_{7-\delta}$ with good in-plane alignment and texturing (*i.e.,* a low degree of c-axis wobble among the many grains) [9].

The initial XRD scan yielded a relatively high value for the c-axis crystal length, 11.737 Å, indicating insufficient oxidation of the YBCO. The sample underwent an annealing process in a pure oxygen environment for 12 hours at a temperature of

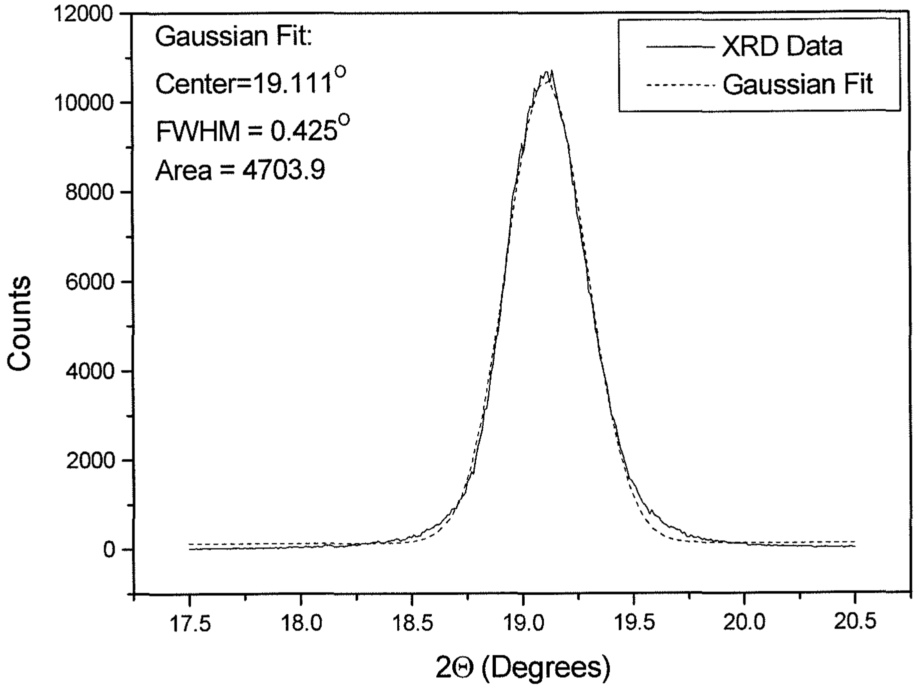

Figure 4.10: Rocking curve XRD analysis of YBCO-03/21/00 film includes a gaussian fit to show the FWHM = 0.425 °.

450 °C. At the conclusion of the annealing process, the film was reanalyzed with XRD resulting in the diffraction pattern shown in Figure 4.11. The new c-axis length of 11.675 Å compares well with the typical length of 11.665 Å for high quality STI films.

Unfortunately, none of the films grown in our chamber exhibit superconductivity above 78 K. All films were tested for superconductivity using a Lakeshore magnetic susceptibility instrument located at STI [105]. The films are exposed to a magnetic field generated by the primary induction coil located above the sample. The presence of this magnetic field is detected on the other side of the sample through the use of a second "pick-up" coil. The entire assembly is cooled with liquid nitrogen, and the strength of the measured magnetic field is plotted versus temperature. As the sample transitions into superconductivity, the magnetic field is repelled, and the signal

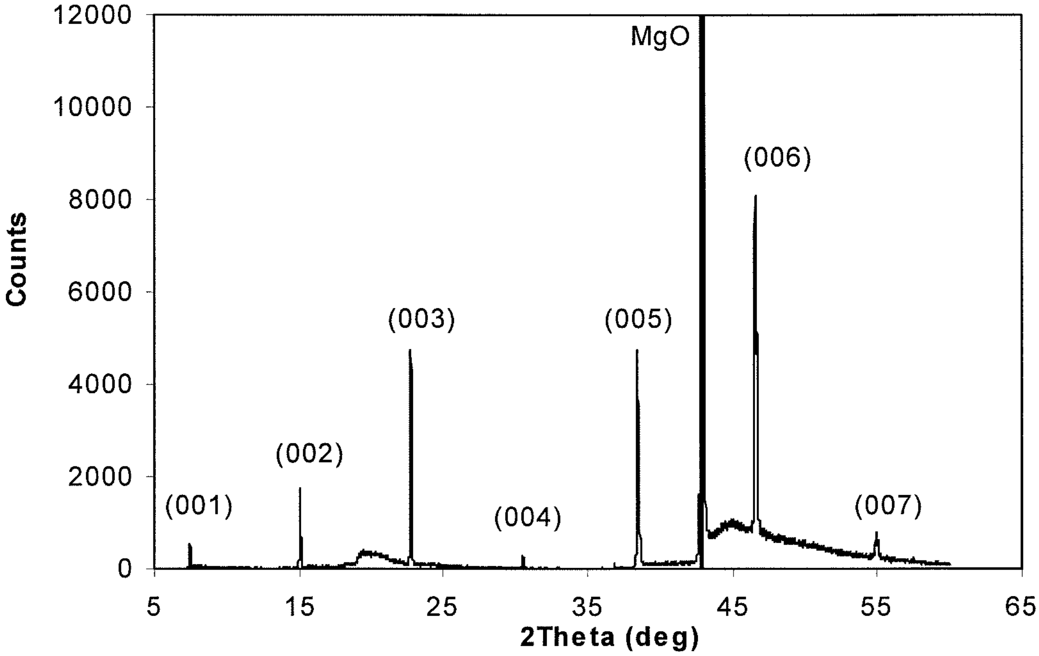

Figure 4.11: XRD analysis after annealing treatment, same film as Figure 4.9. Careful examination reveals a new peak of only 138 counts, at $2\Theta = 37^\circ$, which can be attributed to CuO.

detected by the pick-up coil gradually vanishes. Due to the limitation imposed by the boiling point of liquid nitrogen, our samples were not found to superconduct at temperatures greater than 78 K. In search of an explanation for this behavior, we investigated two films with electron microprobe analysis.

4.3.2 Silicon Incorporation

Electron microprobe analysis was carried out with a Jeol JXA-733 electron microscope designed for the non-destructive x-ray microanalysis and imaging of solid materials. It is capable of high spatial resolution and relatively high analytical sensitivity. The electron microprobe is capable of detecting nearly all of the elements in the periodic table (beryllium through uranium) at sensitivities on the order of 100 parts per million (ppm) [54, 119].

As with the XPS analysis presented above, we were looking for potential contaminants. Films were scanned for Fe, Si, Sr, Zn, Ni, and Pr. The electron microprobe is capable of acquiring digital secondary-electron and backscattered-electron images as well as digital x-ray maps. Figure 4.12 shows one image which was captured from secondary electron emission; as such, the gray scale represents atomic mass rather than surface height. We found a mountainous inclusion which grew around a particle of zinc and iron which appeared to have come from the inconel can[1] (note the large black island pictured in the lower left of Figure 4.12). Another inclusion was found to contain 17% (molar) silicon (small black ringed spot in the upper right of Figure 4.12). In addition, the smoother continuous film contained silicon in the range of $0.3 - 3.0\%$ (background of Figure 4.12).

There exists a significant body of knowledge concerning growth of YBCO on silicon [42, 43, 48, 97, 103, 133] and incorporation of Si in YBCO films [96, 98, 106]. However, we were unable to find specific data relating percent Si in YBCO to the critical temperature of superconductivity. It is universally acknowledged that the presence of silicon in YBCO depresses the critical temperature and critical current [42], and if the concentration of silicon is high enough, the material will not become superconducting at any temperature [96].

Complete inhibition of superconductivity has been achieved with half an atom of silicon per unit cell of YBCO [98], which corresponds to a 3% molar concentration of Si. In fact, 100nm thick YBCO films grown on (100) Si substrates, which did not exhibit any superconductivity, also did not have enough silicon at the surface to be detectable by XPS [43], hence the need for electron microprobe analysis.

It is also worth noting that in one study using Si ion implantation to inhibit superconductivity [98], the lattice parameters and crystal structure of the YBCO were preserved. Their XRD results clearly show c-axis oriented 1:2:3 phase YBCO

---

[1] The original inconel can had been damaged by electrical arcing from the heater terminals and has since been replaced.

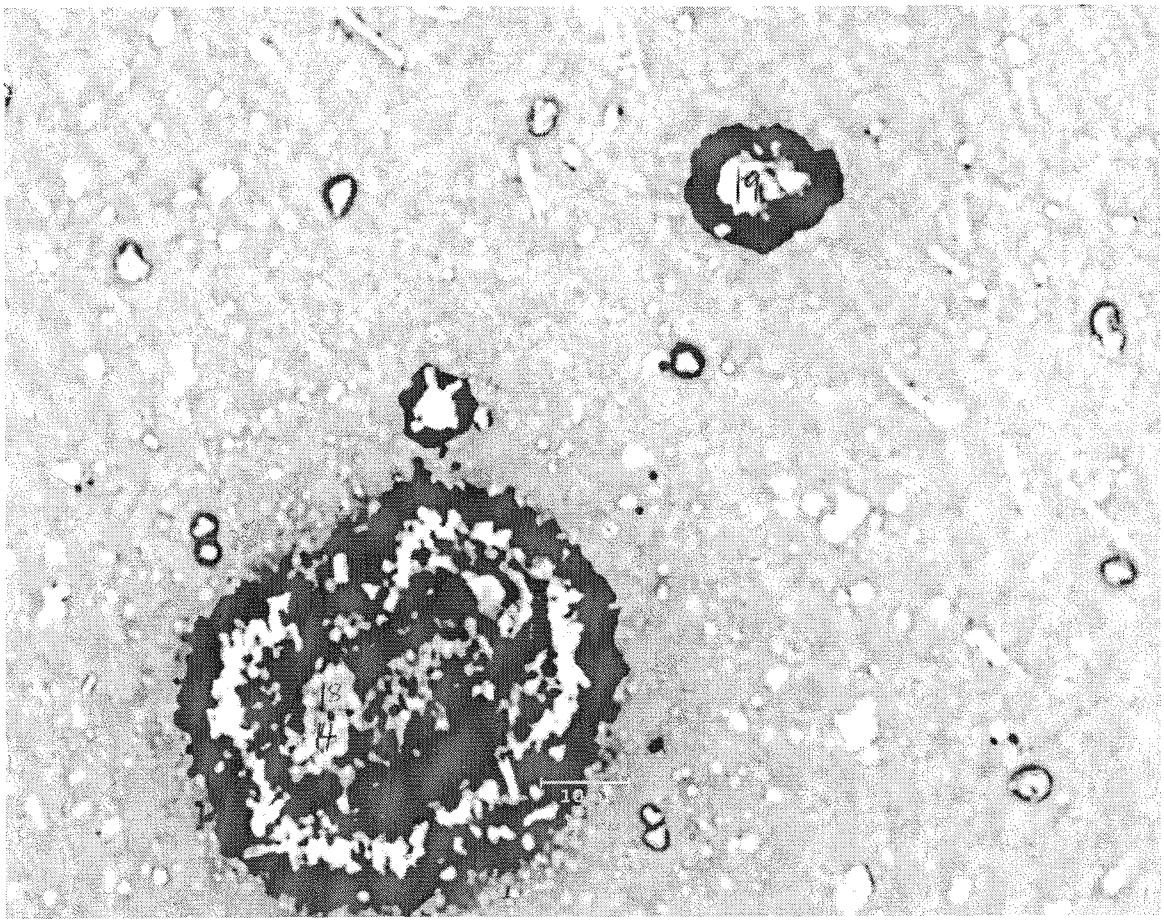

Figure 4.12: Secondary-electron emission image captured from electron microprobe analysis of YBCO film from 3/21/00.

regardless of Si concentration or post-implantation annealing procedures.

Films grown on silicon substrates have been shown to transition to superconductivity, although the required film thickness is at least 1 μm [43]. Even in the case of these very thick films, transition temperatures are most often $< 75\,\mathrm{K}$ [103].

The obvious conclusion is that our films do not superconduct at temperatures greater than 78 K because of the silicon contamination. The silicon reacts with the oxygen and metals in the film to form compounds such as copper silicide [106] and barium silicate [43]. Once the metal atoms are chemically bound to silicon, they are no longer able to donate charge carriers [43]. The most likely source of the silicon in our film is the SiC susceptor[2].

Nonetheless, we have demonstrated the ability to grow epitaxial 1:2:3 phase YBCO with good texturing and crystalline structure. As such, we felt justified in adapting our growth results for use in chemistry and growth models.

4.3.3 Gas Phase Chemistry Models

Our experimental data has already had an impact on YBCO – CVD modeling efforts. Raja and Kee [118] have implemented a gas phase and surface chemistry model which incorporates sticking coefficients generated from the results presented in table 4.1.

The decomposition mechanisms for the $Y(tmhd)_3$, $Ba(tmhd)_2$, and $Cu(tmhd)_2$ precursors have been postulated in the literature (references [111, 60] discuss $Cu(tmhd)_2$ decomposition in particular, while references [150, 25] discuss the decomposition pathways of many organometallic precursors including $Y(tmhd)_3$, $Ba(tmhd)_2$, and $Cu(tmhd)_2$). Generally speaking, the metal ions tend to shed their ligands as the initial step in the decomposition, followed by further breakdown of the hydrocarbon chain and oxidation of the metal ion. Table 4.3 presents the associated reactions, while the Arrhenius data is discussed below.

Basic chemical kinetics tells us that for any chemical reaction, say

$$A + m \times B \rightarrow C \ , \tag{4.4}$$

---

[2] STI also has a susceptor made of SiC in their chamber. However, they also found contaminants in their films which originated in the susceptor. The contaminants were eradicated through the use of a sapphire disc, which served as an intermediary between the substrate and susceptor. Plans for such an intermediary, or a susceptor made entirely of sapphire, are currently under way for our reactor.

Table 4.3: Gas phase precursor decomposition mechanism and the associated Arrhenius values. Note that "products" refers to various hydrocarbon pyrolisis products including carbon dioxide and water vapor.

Chemical Reaction	K_0	E_A (kcal / mol)	Ref.
$Y(tmhd)_3 \rightarrow YO$ + products	2.2×10^9	34.3	[23]
$Y(tmhd)_3 + O \rightarrow YO$ + products	4.08×10^{16}	30.3	[23]
$Ba(tmhd)_2 \rightarrow BaO$ + products	2.39×10^{17}	52.15	[118]
$Ba(tmhd)_2 + O \rightarrow BaO$ + products	1.69×10^{22}	41.1	[118]
$Cu(tmhd)_2 \rightarrow CuO$ + products	1.5×10^9	26.89	[149]
$Cu(tmhd)_2 + O \rightarrow CuO$ + products	9.6×10^{11}	32.72	[149, 24]

the creation or depletion rate of any of the species can be written as

$$\frac{d[C]}{dt} = k\,[A][B]^m \,, \tag{4.5}$$

where $[A]$, $[B]$, and $[C]$ are the concentrations of those species and k, a function of temperature, T, is the reaction rate,

$$k = K_0 T^n e^{E_A/RT} \,. \tag{4.6}$$

In most cases $n \sim 0$ and the important quantities are the pre-exponential factor, K_0, and the activation energy, E_A. Equation (4.6) is known as the Arrhenius equation, and the values for the constants are presented in table 4.3.

This set of chemical reactions has been incorporated into a two dimensional CVD modeling code entitled SPIN from Sandia Labs [29], which uses a finite-difference method to solve the basic flow and energy equations inside the reactor. The SPIN code provides a flux of metal oxide particles to the growing surface of the film. In order to properly incorporate the metal oxide particles into the YBCO film, sticking coefficients are required. The sticking coefficient is a ratio of the flux of arriving molecules to the surface of the film divided by the number of these molecules that are incorporated into the film.

The sticking coefficients are found by iteratively backing out the molar deposition rate for each metal (f_{YO}, f_{BaO}, and f_{CuO}) from the stoichiometries of the run data. In other words, since the growth rate and stoichiometry of the film is known, the deposition rate for each metal is known. The relationship between the molar deposition rates and the corresponding sticking coefficient was found through successive iterations of the SPIN code for hypothetical values of the sticking coefficients. This data was then fit to a fifth order logarithmic polynomial.

In our case, there are four equations for the molar deposition rates, and only three unknowns,

$$\text{Growth Rate} \propto (f_{YO} + f_{BaO} + f_{CuO}) \tag{4.7}$$

$$\text{Fraction of Y in the film} = \frac{f_{YO}}{f_{YO} + f_{BaO} + f_{CuO}} \tag{4.8}$$

$$\text{Fraction of Ba in the film} = \frac{f_{BaO}}{f_{YO} + f_{BaO} + f_{CuO}} \tag{4.9}$$

$$\text{Fraction of Cu in the film} = \frac{f_{CuO}}{f_{YO} + f_{BaO} + f_{CuO}} . \tag{4.10}$$

Hence, the system is over-determined. The molar deposition rates are found through a standard practice of minimization of the residuals. The sticking coefficients are then backed out of the logarithmic polynomial fit, for each growth run. All of the data is presented in Figure 4.13. Although the correlation coefficients for each linear regression are low (~ 0.1), the trendlines are presented to show the lack of temperature dependence for each sticking coefficient. It is also worth noting that the relatively high variability of the barium data is related to the difficulties encountered

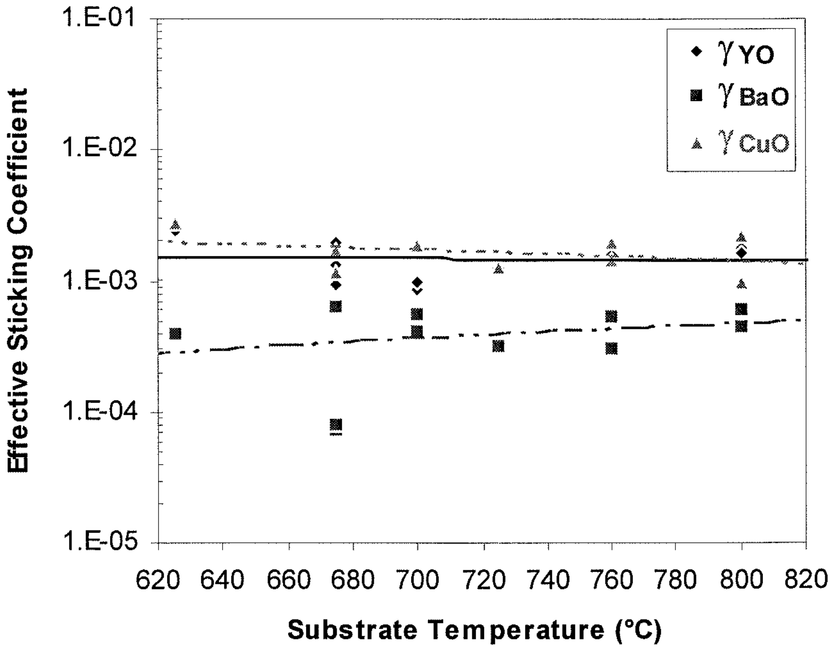

Figure 4.13: Plot of sticking coefficient versus temperature for each oxidized metal species, yttrium-oxide, barium-oxide, and copper-oxide. Each data point represents the results of a single growth run, while the lines represent linear regression fits to this data.

with condensation of barium in the gas handling system (discussed further in Chapter 2).

$$\gamma_{YO} = Temperature \cdot \left(-5.3 \times 10^{-7}\right) + 1.9 \times 10^{-3} \tag{4.11}$$

$$\gamma_{BaO} = Temperature \cdot \left(1.1 \times 10^{-6}\right) - 4.1 \times 10^{-3} \tag{4.12}$$

$$\gamma_{CuO} = Temperature \cdot \left(-3.1 \times 10^{-6}\right) + 4.0 \times 10^{-3} \tag{4.13}$$

The average values are $\gamma_{YO} = 1.7 \times 10^{-3}$, $\gamma_{BaO} = 4.0 \times 10^{-4}$, and $\gamma_{CuO} = 1.5 \times 10^{-3}$. Note that the lower sticking coefficient for barium correlates with the higher required flow rate of barium-tmhd.

4.4 Conclusion

Film growth results show that the MOCVD reactor is capable of growing highly uniform films under a wide variety of conditions. Growth of stoichiometric $YBa_2Cu_3O_7$ shows c-axis oriented grains with a low degree of c-axis wobble, and the presence of purely 1:2:3 phase material. FTIR results presented allow for an accurate calibration of the wafer temperature, and provide a qualitative means of monitoring film thickness. Mass spectrometry was used to verify the uniformity of the boundary layer, and optimize growth and cool-down gas-phase oxygen concentrations. Lastly, the film growth results were used to determine sticking coefficients for each of the metal-oxide species. The sticking coefficient values have been implemented in a gas-phase and surface chemistry model at the Colorado School of Mines [118].

Chapter 5 CGS Experiments

5.1 Introduction

As semiconductor manufacturers move to larger sized wafers and smaller sized features, the effects of film stress are important globally and locally to insure high yields and high performance devices. In addition, stress effects in thin film YBCO are of theoretical and experimental interest for use in growth models and to explain crystalline morphology. However, standard methods of measuring the related curvature tensor, $\boldsymbol{\kappa}$, are either difficult to apply *in-situ* and in real time (x-ray diffraction [6]), do not give an instantaneous full field map of the curvature tensor (beam bending [7]), or are sensitive to external vibrations (interferometric methods [168]). Based on optical beam shearing methods, Coherent Gradient Sensing (CGS) is a full field, real time and space, optical method which gives a direct mapping of the components of the curvature tensor for the film-substrate system. Initially referenced to a flat surface, a collimated incident beam is reflected from the sample and "sheared" by a series of diffraction gratings. The corresponding orders are combined, and the resulting first order interferogram can be shown to be directly related to the components of the curvature tensor across the sample.

We have implemented CGS in our MOCVD reactor to examine the curvature tensor of the film-substrate system throughout the growth and annealing process. For fully grown single-sided films, we have obtained a dynamic map of the magnitude of the average stress under various annealing conditions. Furthermore, CGS is used to observe the deposition of YBCO thin films onto bare MgO substrates.

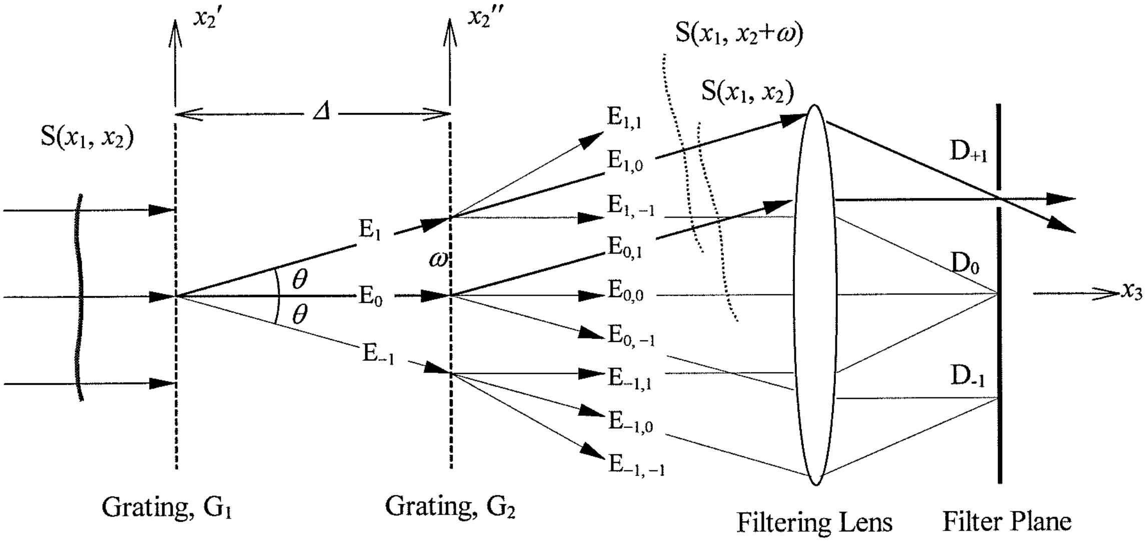

Figure 5.1: Ray diagram of the optical path of the CGS beam after reflection off the sample. Illustration courtesy of David Owen, Caltech Aeronautics.

5.2 CGS Theory

Based on beam shearing methods, CGS was first applied to thin films by Rosakis *et al.* [121]. A schematic of the optical path is shown in Figure 5.2. Initially referenced to a flat surface, a well collimated coherent beam, with an initial phase of $S(x_1, x_2)$, is reflected from the sample at an angle of incidence of 60° from the surface normal. After realignment by two angled mirrors, the beam passes through a series of two transmission gratings. The gratings effectively displace or "shear" the beam laterally by a small amount, ω. The resulting first order wavefronts, $E_{0,1}$ and $E_{1,0}$, with phases $S(x_1, x_2 + \omega)$ and $S(x_1, x_2)$, are combined to form a first order interferogram at D_{+1} as shown in Figure 5.1.

The wave front shift is parallel to the principal axis of the gratings, as shown in Figure 6.1. The magnitude of the shift is a function of the grating separation, Δ, and the diffraction angle, θ, as

$$\omega = \Delta \tan\theta \ , \tag{5.1}$$

where the diffraction angle, θ, is given by

$$\theta = \arcsin\frac{\lambda}{p} \ , \tag{5.2}$$

with λ being the wavelength of light and p being the grating pitch. For a small angle of diffraction, these equations approximate to

$$\begin{aligned} \omega &\cong \Delta\theta & (5.3) \\ \theta &\cong \frac{\lambda}{p} \ . & (5.4) \end{aligned}$$

The conditions for constructive interference of the original and shifted wave fronts may be expressed as

$$S(x_1, x_2 + \omega) - S(x_1, x_2) = n^{(2)}\lambda, \qquad n^{(2)} = 0, \pm1, \pm2, ... \tag{5.5}$$

where $n^{(2)}$ is an integer identifying the fringes observed for shearing along the x_2 direction. Dividing equation (5.5) by ω gives

$$\frac{S(x_1, x_2 + \omega) - S(x_1, x_2)}{\omega} = \frac{n^{(2)}\lambda}{\omega}, \qquad n^{(2)} = 0, \pm1, \pm2, ... \tag{5.6}$$

which in the limit of $\omega \longrightarrow 0$, may be approximated by

$$\frac{\partial S(x_1, x_2)}{\partial x_2} = \frac{n^{(2)}\lambda}{\omega}, \qquad n^{(2)} = 0, \pm1, \pm2, ... \tag{5.7}$$

Substituting for λ and ω yields

$$\frac{\partial S(x_1, x_2)}{\partial x_2} = \frac{n^{(2)} p}{\Delta}, \qquad n^{(2)} = 0, \pm 1, \pm 2, ... \tag{5.8}$$

Generalizing the result to include wave front shearing in either direction, $x_1$or x_2, we have

$$\frac{\partial S(x_1, x_2)}{\partial x_2} = \frac{n^{(\alpha)} p}{\Delta}, \qquad n^{(\alpha)} = 0, \pm 1, \pm 2, ... \tag{5.9}$$

where $n^{(\alpha)}$ represents the fringes observed for shearing along the x_a direction and $\alpha \in \{1, 2\}$. Equation (5.9) is the governing equation for interferograms formed using the technique of CGS. With further assistance provided by Lee, Rosakis, and Freund, [89], we can relate the fringes to curvature.

Beginning with a curved sample surface, $x_3 = f(x_1, x_2)$, we know that the curvature tensor has three components at any position (x_1, x_2). First, κ_{11} and κ_{22} are the convexities (or concavities) in the x_1 and x_2 directions and $\kappa_{12} = \kappa_{21}$ is the twist in the sample. From our definition of the surface, we also know that

$$\kappa_{\alpha\beta}(x_1, x_2) \cong \frac{\partial^2 f(x_1, x_2)}{\partial x_\alpha \partial x_\beta}, \qquad \alpha, \beta \in (1, 2)\ . \tag{5.10}$$

It can be shown [89] that for small surface deflections,

$$\left|\nabla^2 f\right| << 1\ , \tag{5.11}$$

that

$$\frac{\partial S(x_1, x_2)}{\partial x_\alpha} = \frac{1}{2} \frac{\partial f(x_1, x_2)}{\partial x_\alpha} = \frac{n^{(\alpha)} p}{2\Delta}\ . \tag{5.12}$$

Table 5.1: The correlation between the oxygen content in the material $YBa_2Cu_3O_x$ and lattice parameters of the unit cell is listed below.

x	a_0(Å)	b_0(Å)	c_0(Å)
7.0	3.822(1)	3.891(1)	11.677(2)
6.78	3.827(2)	3.895(2)	11.722(7)
6.76	3.830(2)	3.898(2)	11.728(6)
6.72	3.835(4)	3.890(4)	11.716(11)
6.60	3.831(2)	3.889(2)	11.736(6)
6.53	3.838(2)	3.887(2)	11.747(6)
6.51	3.845(3)	3.887(3)	11.768(8)
6.30	3.851(5)	3.883(5)	11.789(16)

Thus the desired relation becomes:

$$\kappa_{\alpha\beta}(x_1, x_2) \cong \frac{p}{2\Delta} \frac{\partial n^{(\alpha)}(x_1, x_2)}{\partial x_\beta} \,. \tag{5.13}$$

Equation (5.13) provides a mechanism to derive the curvature tensors from CGS interferograms. In this manner, CGS interferograms provide a full field technique for determining the instantaneous value of the curvature tensor for any specimen at any point, (x_1, x_2).

In our experiments, we vary either the oxygen content or the temperature of the wafer and count the number of fringes present in the x_2 direction. As we have already demonstrated, the fringes can be related to the curvature.

Cava *et al.* [26] have provided the necessary data to correlate curvature and oxygen content. Table 5.1 is reproduced from their work. As oxygen stoichiometry is changed, the lattice parameters of the YBCO structure are altered. The resulting volumetric change in the thin film when compared with no such changes in the structure of the supporting substrate results in a measurable degree of curvature for the wafer-substrate system.

Similar results are achieved with variations in temperature. Because MgO and YBCO have different coefficients of thermal expansion, as the temperature is changed, so is the stress state, and hence curvature, of the film-substrate system.

5.3 Experimental

The experiments were performed in the stainless steel, cylindrical, cold-wall, vertical, stagnation flow reactor described in Chapter 2. Gas flows of O_2 and N_2 ranging from 0 to 5 slm travel vertically down through the showerhead, while there is a shroud flow of 1.0 slm of N_2 around the showerhead to contain the flow. A series of mass flow controllers and actuated pumping allows for a constant background pressure to be maintained throughout the runs. For this investigation, we maintained the chamber pressure at either 10 torr or 100 torr. The gas was sampled near the substrate with a mass spectrometer in order to verify the composition of flow near the substrate. Temperature for the initial runs was measured by a thermocouple on the inside of the can. For the later, fully oxygenated runs, direct thermocouple contact was made with the susceptor.

The optical path through the reactor is at 60° from normal to the sample, a 18mWatt He-Ne laser provides a 1.5 in diameter collimated incident beam. The diffraction gratings have a pitch of 1000 lines/inch, and the grating spacing was 1 in for the 1×1 in wafer runs and increased to 2 in for the later runs. The sensitivity of CGS in this arrangement is $0.01\,\mathrm{m}^{-1}$ [20]. Because a single set of gratings was used, curvature in only one direction could be measured during an individual run. The images were captured on a Sony TRV43 camcorder. A schematic illustration of the experimental setup is shown in Figure 5.2, while digital photographs of the optics into and out of the reactor are shown in Figures 5.3 and 5.4.

The MOCVD of YBCO on MgO samples are well oriented, c-axis polycrystalline and were supplied by Superconducting Technologies Inc. [105]. *Ex-situ* CGS measurements of the supplied YBCO-MgO samples reveal them to be slightly curved and

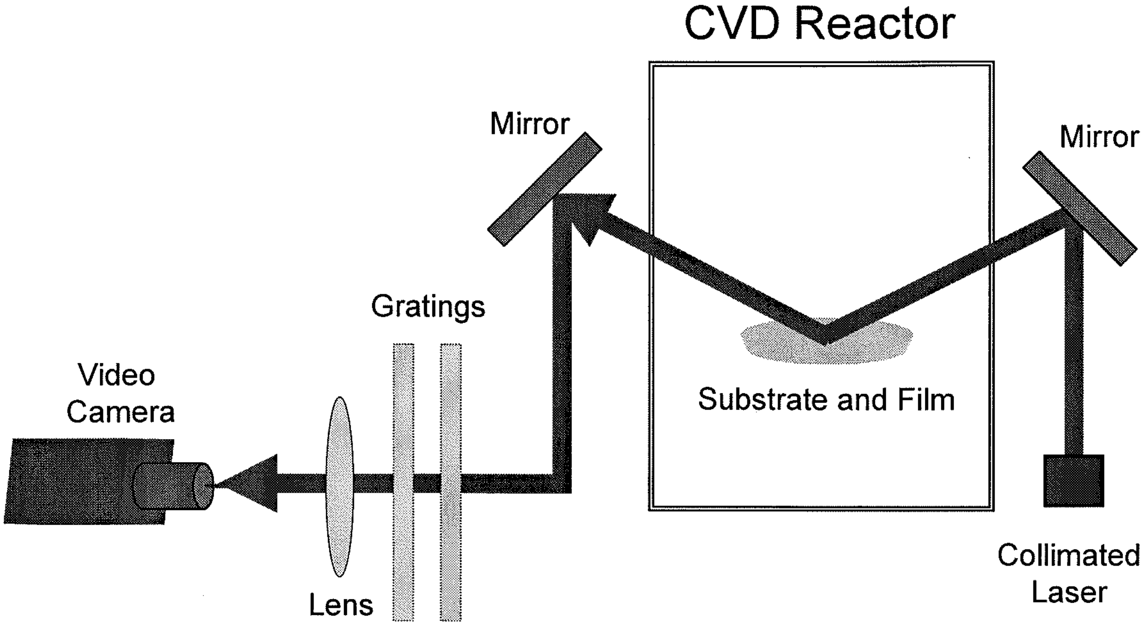

Figure 5.2: Schematic representation of the *in-situ* CGS analysis equipment.

spatially non-uniform. The respective curvatures of the bare wafer were not measured prior to production; however, the curvature of the supplied MgO substrates typically have a radius curvature less than 0.01 m^{-1}. XRD results show the presence of strictly 1:2:3 phase YBCO with a typical c-axis length of 11.665Å. Susceptibility measurements indicate a $T_c \geq 80\,^{\circ}C$ and $\Delta T_c \sim 1\,^{\circ}C$. Reference [105] further details the high quality nature of the supplied samples.

5.4 Results

To examine the strain due to thermal mismatch between MgO and YBCO, a one inch, square YBCO (700 nm thick) on MgO (0.5 mm thick) sample was heated from room temperature to 760 °C in vacuum in one hour while simultaneously monitoring the CGS interferograms. The sample was baked *in-situ* at 700 °C for one hour prior to the run to remove excess oxygen. UV reflectance spectra indicate the initial oxygen

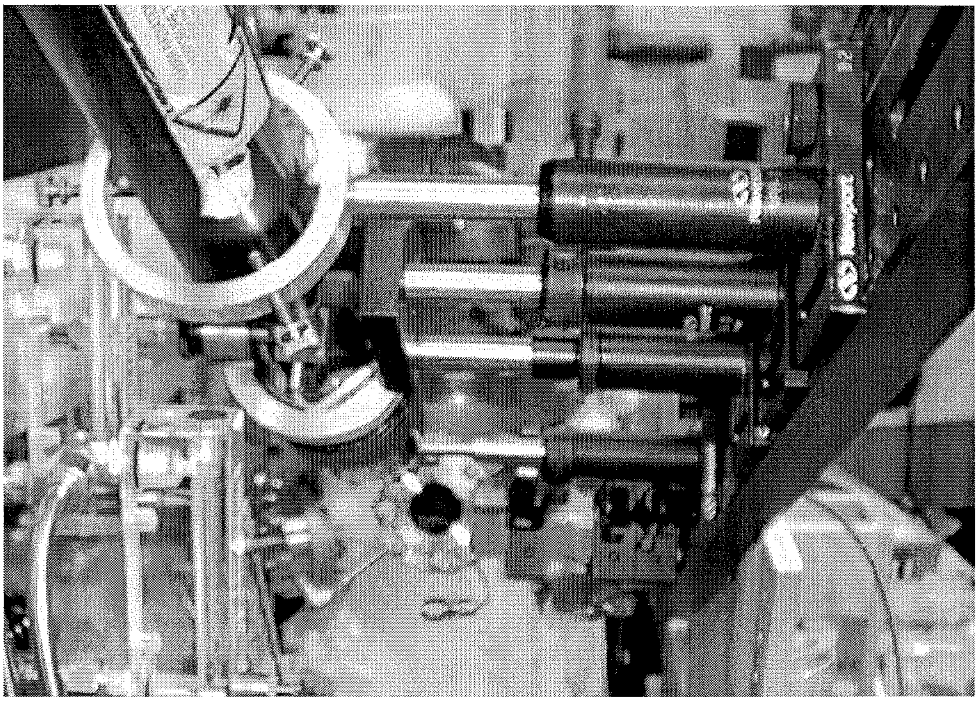

Figure 5.3: A view of the CGS optical path down the axis of the laser, through the collimating lens, and into the chamber.

stoichiometry of the $YBa_2Cu_3O_x$ to be $x \leq 6.3$ [76]. The CGS interferograms with shearing along the x_2 direction are shown in Figure 5.5.

We use Stoney's equation [136, 49] for thin films, $h_f \ll h_s$,

$$\kappa = 6\varepsilon_f \frac{h_f}{h_s^2} \frac{E_f}{E_s} \frac{(1 - \upsilon_s)}{(1 - \upsilon_f)} , \tag{5.14}$$

which becomes

$$\sigma_f = \frac{1}{6} \frac{E_s}{(1 - \upsilon_s)} \frac{h_s^2}{h_f} \kappa \tag{5.15}$$

when written in terms of stress in the film, σ_f. Variables $h_f = 700\,\text{nm}$ and $h_s = 0.5\,\text{mm}$ are the respective film and substrate thickness, $E_f = 148$ GPa [88] and $E_S = 315$ GPa [132] are the respective Young's moduli, $\upsilon_f = 0.255$ [88] and $\upsilon_s = 0.176$

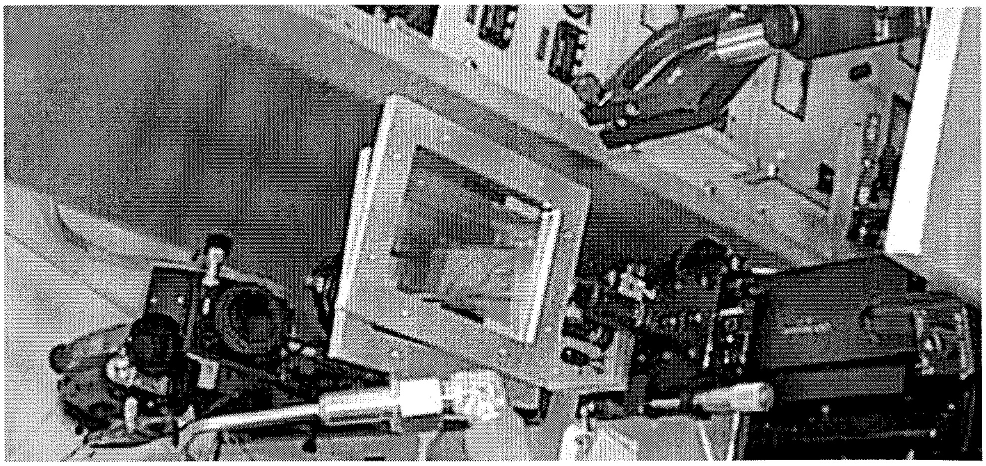

Figure 5.4: The CGS beam travels from right to left coming out of the reactor and reflecting off the mirror (upper right) before passing through the two gratings, aperture, and lens. Lastly the beam enters the video camera at the far left.

[132] are the respective Poisson's ratios. The measured curvatures from the CGS interferograms are combined with the values presented above and equation (5.15) to calculate the average stress, σ_f, and strain, ε_f, in each direction. The results are plotted versus temperature in Figure 5.6, where the strain values are calculated from the following relation,

$$\varepsilon_f = \sigma_f \frac{(1 - v_f)}{E_f} \ . \tag{5.16}$$

It is important to note that the CGS interferogram alone does not give the sign of the curvature, so the values reported are absolute.

The measured κ_{11} component shows a monotonically increasing stress-strain relationship with increasing temperature, while the measured κ_{22} component indicates similar room temperature values as κ_{11}, but exhibits a local minima at 624 °C and then increases to 1.03 GPa above 719 °C.

Exploring the orthorhombic to tetragonal phase transition, we examined fully oxygenated 2 inch diameter wafers from 25 °C to 650 °C under various oxygen conditions.

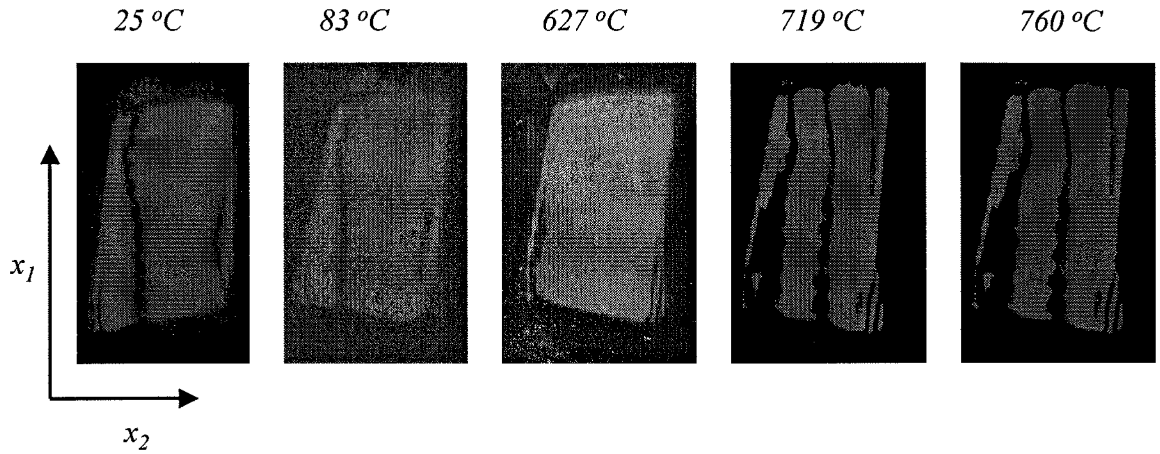

Figure 5.5: Series of CGS interferograms YBCO on MgO with temperature increasing from left to right. Shearing is along the x_2 direction.

A constant background pressure of 10 torr was maintained throughout the runs with flows of O_2 and N_2 ranging from 0 to 5 slm. The susceptor temperature was cycled between 300 °C and 600 °C in one hour while monitoring the CGS interferograms. The ratios of O_2/N_2 were 100 : 1 and vice versa for the respective oxygen and nitrogen rich cycles. Figure 5.7 shows a series of images taken as the temperature is cycled under different oxygen partial pressures. In the N_2 rich cycle (bottom), the initial interferogram remains intact with little change in the magnitude or direction for temperatures up until 558 °C, where we observe a sharp transition in the CGS interferogram in both magnitude and direction. For the O_2 rich cycle (top), we observe a similar transition but at a higher temperature, 584 °C – 650 °C. Hence, the transition temperature depends strongly on the O_2 partial pressure. In both cases, the transformation is reversible. By toggling the O_2 and N_2 ratio at 560 °C, the interferogram was seen to revert repeatedly from an oxygenated state to a deoxygenated state and back.

We find the curvature to be higher for oxygen rich conditions over the temperature range studied. Figure 5.8 shows CGS interferograms of a similarly prepared YBCO-

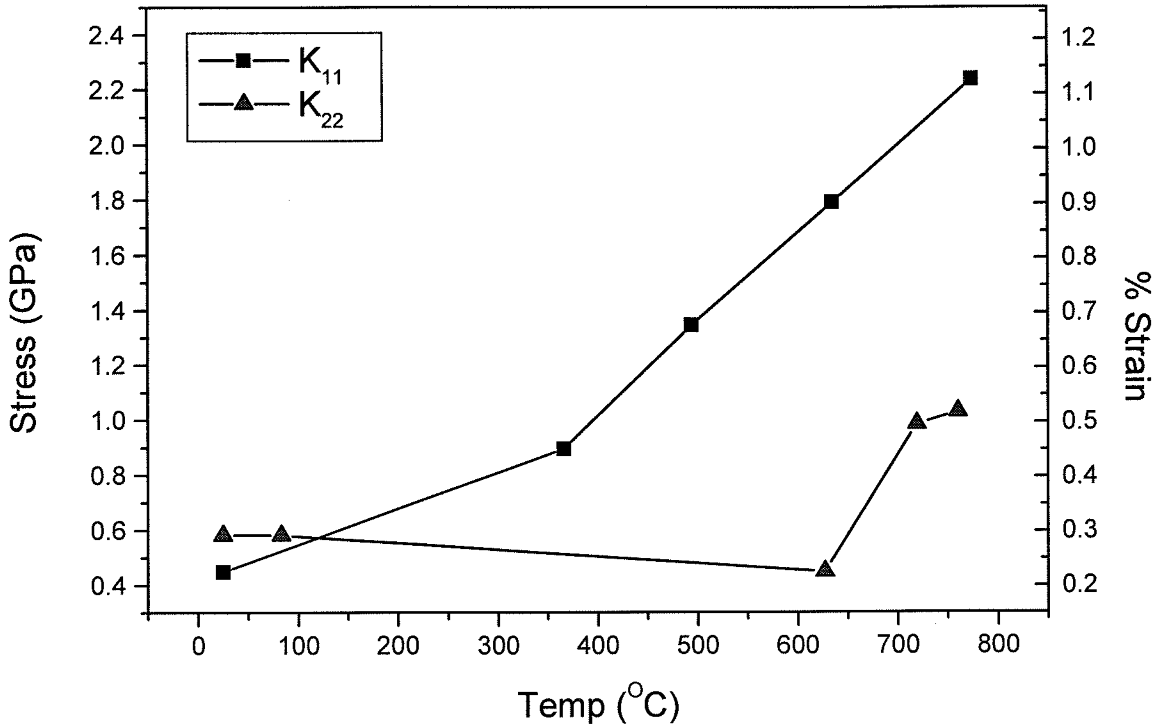

Figure 5.6: Stress and strain values calculated from the CGS interferograms presented in Figure 1.

MgO wafer held at constant temperature, 615 °C (±10 °C), with O_2 and N_2 flows. The total pressure is 100 torr. With the higher pressure, we see that the curvature doubles within about 7 minutes of changing the flow. Figure 5.7 illustrates this behavior.

We also implemented CGS analysis during YBCO film growth. Figure 5.9 shows three images of a 2 in substrate during the MOCVD growth of YBCO. Notice that despite film deposition, the basic fringe pattern does not change. This growth, conducted on 9/30/99 and resulting in a 365 nm thick film with nearly perfect 1:2:3 stoichiometry, begins and ends (after ~2 hours) with the fringe count of 5.8 as depicted in the figure. CGS analysis of several growth runs confirms that there is no change in curvature as YBCO films are deposited in our MOCVD reactor (the notable caveat is

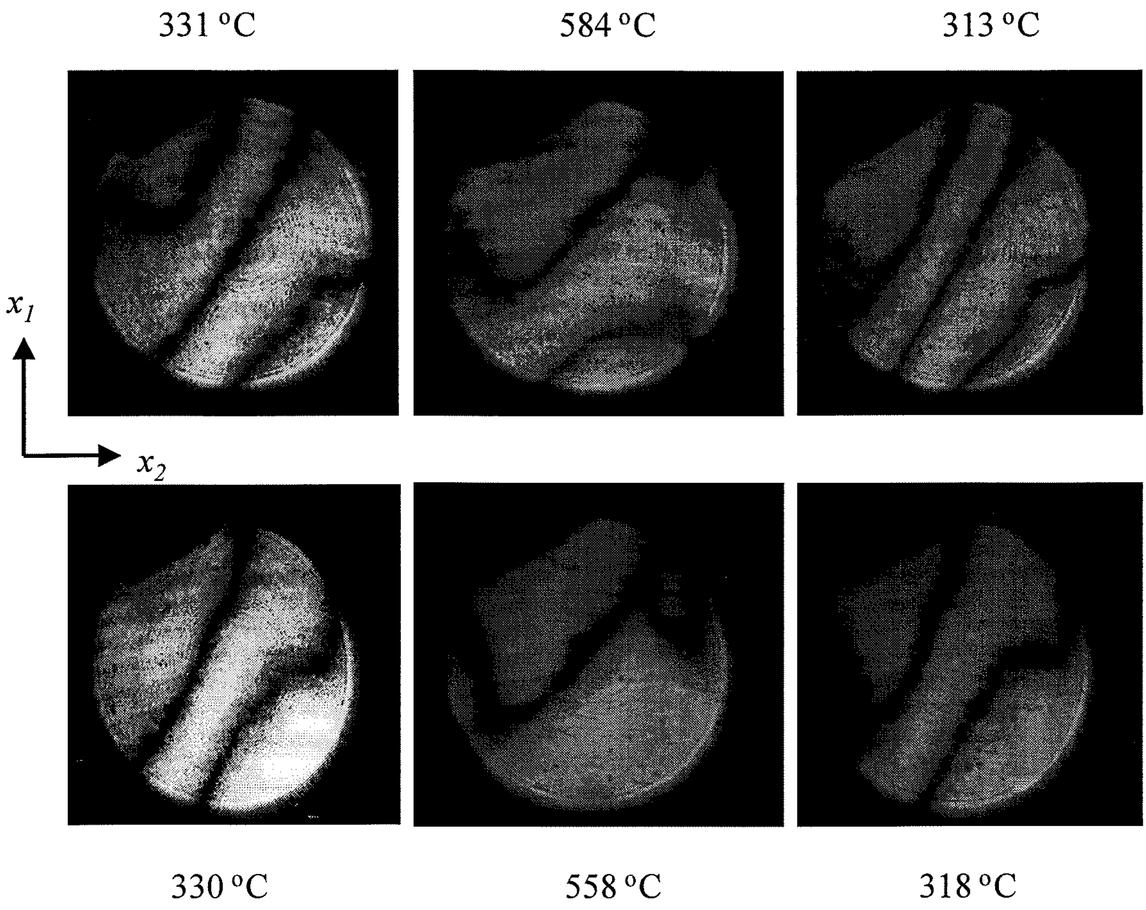

Figure 5.7: Series of CGS interferograms of YBCO on MgO with showerhead flows of 5.0 slm of O_2 (top) and N_2 (bottom). Total pressure is 10 torr. Shearing is along the x_1 direction.

that no films have been grown to thicknesses $> 500\,\mathrm{nm}$ during *in-situ* CGS analysis).

Figure 5.9 is also interesting because the initial substrate had a structural defect in the single crystal of MgO. In the first interferogram (uncoated MgO), there is a fingerprint type of fringe pattern in the upper right corner of the interferogram. This fingerprint pattern indicates local stresses around the defect. As the YBCO is deposited, the defect is covered up by a smooth film of YBCO, and the associated fingerprint pattern eventually vanishes.

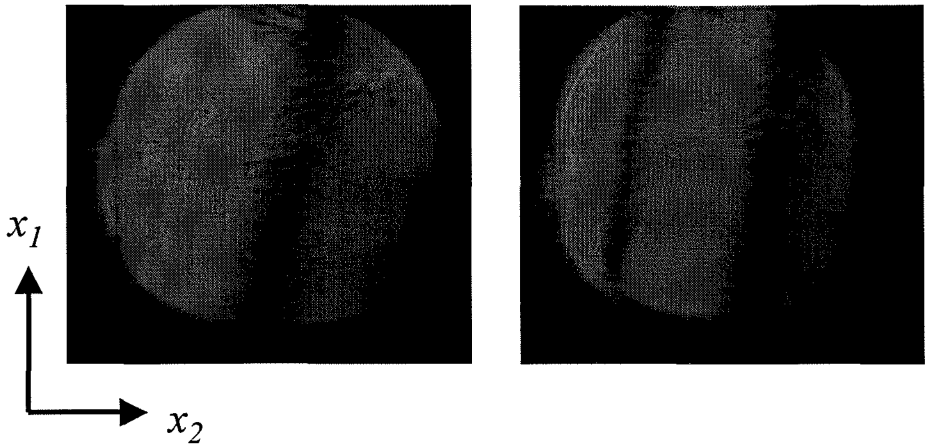

Figure 5.8: CGS interferograms of YBCO on MgO at 615 °C (±10 °C) under O_2 (right) and N_2 (left) flows of 5.0 slm. Total pressure is 100 torr. Shearing is along the x_1 direction.

5.5 Discussion

For the non-stoichiometric case, our stress-strain values from the measured κ_{11} and κ_{22} components are 0.4 and 0.6 GPa respectively at room temperature. As seen in Figure 5.6, at room temperature, the stress values derived from κ_{11} and κ_{22} are similar, but there is a dramatic decrease in the κ_{22} component near 624 °C which is indicative of a phase transition.

From published values [168] for varying thickness of YBCO films on MgO (0.5 mm thick x 10 mm diameter) grown by spray pyrolysis at 900 °C, we estimate the average stress produced from a 700 nm film to be -0.7 GPa at room temperature. The average stress values were obtained at room temperature from a series of bending tests, which showed the stress to be concentrated at the center of the sample. The stress is attributed to the lattice mismatch between YBCO and MgO, although the films are not completely stoichiometric and show a substantial amount of Y_2BaCuO_5 at the substrate-film interface. SEM images of the samples do not reveal characteristic spirals found in well oriented, c-axis films. Nonetheless, the values of stress computed

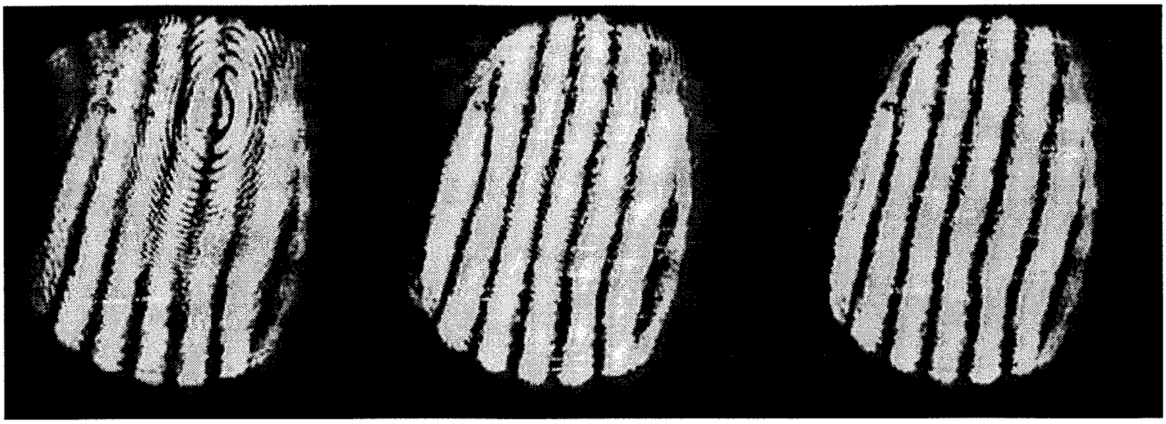

Figure 5.9: CGS interferograms of YBCO growth on MgO (9/30/99). From left to right, the elapsed growth time is 0 min, 8 min, and 29 min.

for our films compare well with the literature.

Of particular interest are the changes in the curvature components with temperature. Stress due to thermal mismatch can be computed using the following relation,

$$\sigma_f = \frac{\Delta T\,|\alpha_f - \alpha_s|}{\alpha_s \Delta T + 1}\,\frac{E_f}{1 - v_f}\,, \tag{5.17}$$

where α_f and α_s are the respective coefficients of linear expansion [74]. Although values for MgO over a broad temperature range are well known ($\alpha_{MgO} = 14 \times 10^{-6}\,\mathrm{K}^{-1}$ at 900 K [129]), similar properties for YBCO are not. For a temperature difference of $\Delta T = 750\,^{\circ}\mathrm{C}$, the coefficient of linear expansion is $21.6 \times 10^{-6}\,\mathrm{K}^{-1} < \alpha_f < 28.9 \times 10^{-6}\,\mathrm{K}^{-1}$ which is high compared to results for YBCO (4000 nm) on MgO buffered $\mathrm{SrTi0_3}$ substrates, $\alpha_{YBCO} = 13.4 \times 10^{-6}\ \mathrm{K}^{-1}$ [74]. Even the theoretical maximum coefficient of thermal expansion for YBCO single crystal material in the (100) direction is only $23 \times 10^{-6}\,\mathrm{K}^{-1}$ [73]. As a result, we can not explain the observed curvature entirely by thermal mismatch [6, 99].

Strain effects due to phase transitions are of great interest [16]. For stoichiometric YBCO, we compare our results to published phase diagrams [154]. Although the data for thin film YBCO is limited, it is clear that for bulk samples between 400 °C and 700 °C, YBCO undergoes an orthorhombic to tetragonal phase transition and that the transition temperature is proportional to the O_2 partial pressure, which is in agreement with our results. It is not clear from theory how the macroscopic curvature is affected by such a transition. However, the dissimilar lattice parameters for each of the two phases will inevitably incur stress effects during the phase transition.

Film thickness and coverage certainly have an effect on the macroscopic stress exhibited by a film substrate system; for this reason we do not believe that the CGS fringe pattern changes are unique to this particular phase transition. However, we do expect a relaxation upon the phase change. Although not fully understood, the observed increase in stress with oxygen flow in Figure 5.8 could be related to a non-equilibrium phase state of the YBCO.

5.6 Conclusions

CGS holds promise as a diagnostic technique: it provides a simple, full field, intuitive image of the curvature tensor under a wide range of run conditions. For thin film YBCO on MgO, we are able to observe changes in the macroscopic curvature of a sample due to thermal mismatch and a phase transition under run conditions. For YBCO, we find the curvature to be a strong function of the oxygen stoichiometry and sample temperature. Conversely, growth of YBCO on MgO does not exhibit any significant changes in curvature, indicating that the growth process occurs in relative equilibrium.

Chapter 6 Oxygen Diffusion in YBCO

6.1 Introduction

One of the most critical factors in the performance of high temperature cuprate semiconductors is the oxygen stoichiometry [26, 73, 85, 112]. For the material of $YBa_2Cu_3O_{6+x}$, variation of the oxygen content from $x = 1$ to $x = 0$ dramatically affects the carrier density in the CuO_2 planes and hence the electronic behavior. Decreasing the oxygen content in the chains acting as the doping reservoir results in a decrease in the carrier density in the CuO_2 planes [78]. Reduced carrier density results in lowered critical current and critical temperatures for superconducting materials.

Most thin film deposition techniques incorporate insufficient oxygen content at growth temperatures, typically $x \approx 0.0 - 0.1$. In order to obtain the proper superconducting phase and stoichiometry, a post-growth oxygenation step is required. Therefore, quantitative and qualitative understanding of the oxygenation process is important for the preparation of high performance films and for the determination of material properties, including superconducting and normal electrical transport, magnetic, and structural properties. Additionally, many growth models could benefit greatly from a better understanding of oxygen transport in high-T_c superconducting films.

Oxygen diffusion both into and out of YBCO thin films has been studied primarily by electrical resistivity measurements [55, 79, 80, 83, 90, 169], oxygen tracer diffusion studies [17, 93], spectroscopic ellipsometry [2, 134], and x-ray diffraction [27, 135], while for bulk materials, investigative techniques also include thermogravimetric analysis (TGA) [77, 68, 131, 139, 153, 170], electrochemical methods [115, 110, 101, 128, 155], and neutron diffraction [70, 116].

Unfortunately, none of these techniques are suitable for use inside the growth chamber, although they are not necessarily intended to be. Electrical resistivity measurements and the other electrochemical methods require silver contact pads to be adhered to the samples. Not only can this not be accomplished *in-situ*, but it is a destructive process which can permanently alter the sample. Tracer diffusion, x-ray diffraction, and neutron diffraction require extensive testing facilities which are difficult or impossible to utilize in conjunction with a growth system. Thermogravimetric analysis is not appropriate for thin films because it does have sufficient sensitivity and works only with large bulk samples. Lastly, spectroscopic ellipsometry, which also requires extensive equipment and can also need computational post-processing, is not appropriate for measuring transient oxygen concentrations. The illuminating light can only provide concentration information to the penetration depth of the wavelength of light used, as opposed to other techniques which provide measurements across the entire film thickness. Additionally, the penetration depth is a function of the oxygen concentration, all of which limit the usefulness of spectroscopic techniques in assessing diffusion rates. Results of ultraviolet reflectance measurements, presented later in this chapter, will confirm this point.

Our use of a new technique, developed at Caltech by the Rosakis group [120] and entitled Coherent Gradient Sensing (CGS), enables us to observe changes in oxygen content indirectly by monitoring the curvature of the wafer. All measurements are made inside of an MOCVD growth chamber capable of producing epitaxial YBCO thin films. In addition to being a continuous, real-time, full-field optical technique which provides a direct map of the curvature across the entire surface of a wafer, CGS is non-invasive (all associated hardware is located outside of the chamber), non-destructive, and highly repeatable and reproducible.

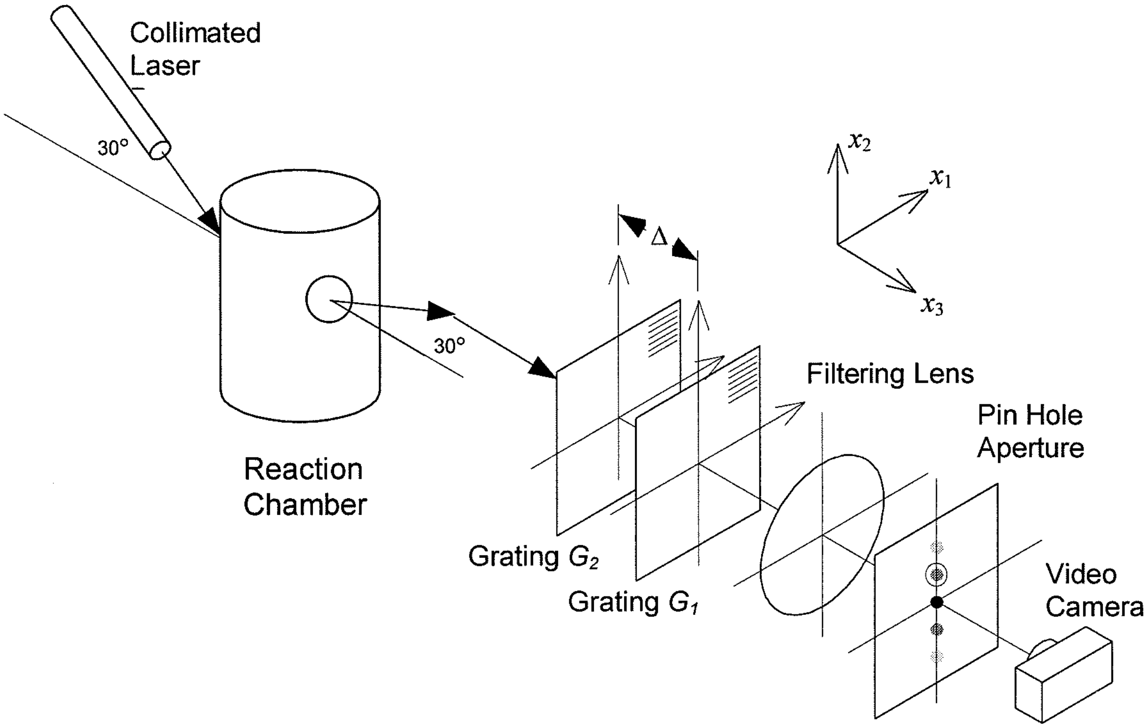

Figure 6.1: Schematic of the optical beam path for our CGS experimental setup.

There is evidence of significant differences in the diffusion constants for films of different morphologies. In other words, films grown by different techniques exhibit different diffusion rates under similar conditions [79]. Thus for film growth models to function accurately they must incorporate chemical data for the particular growth technique they are modeling. To our knowledge, there have not been any oxygen diffusion studies conducted with YBCO grown by MOCVD methods. As such, our experimental data could prove valuable to CVD modeling efforts.

6.2 Diffusion Theory

In order to characterize the diffusion of oxygen into or out of the YBCO film, Figure 6.2, we need to first solve the diffusion equation (also known as the heat equation or

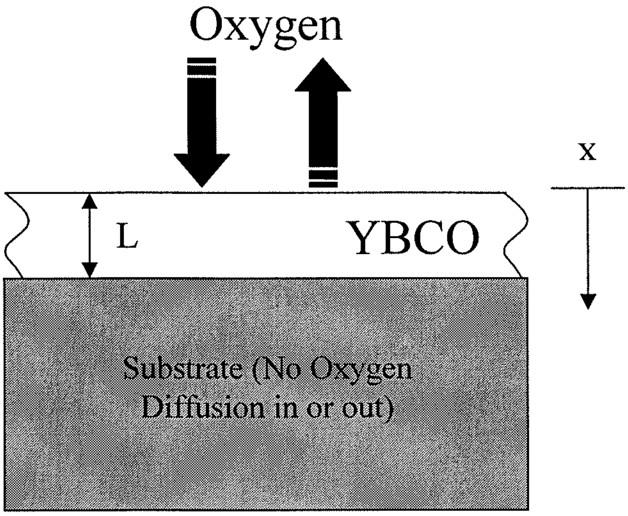

Figure 6.2: Schematic illustrating one-dimensional diffusion of oxygen from the gas phase into and out of the YBCO thin film.

Fick's 2^{nd} law), which is presented in terms of molar concentration, $c(x,t)$, as

$$\frac{\partial c}{\partial t} = D\frac{\partial^2 c}{\partial x^2} , \tag{6.1}$$

where D, the diffusivity of oxygen in YBCO, is assumed to be constant[1]. Time, t, is defined as zero at the moment when the partial pressure of oxygen in the chamber changes, and distance, x, is depicted in Figure 6.2. Our set of experimental conditions allows a on-dimensional treatment of the problem.

The molar concentration of oxygen varies from 6/12 to 7/13; therefore, we will use a simple transformation for the concentration variable,

$$\text{Concentration of Oxygen} = 0.5 + c(x,t) \ . \tag{6.2}$$

---

[1] This assumption, although commonplace in the literature, is in fact, not correct. The diffusion constant is directly related to the concentration of oxygen in the film. Unfortunately, the use of a diffusion constant which varies with concentration makes the analysis intractable.

Using Shewmon's analysis [130], as a starting point, we begin with the separation of variables technique, assuming

$$c(x,t) = X(x)T(t) \; . \tag{6.3}$$

Equation (6.1) then becomes

$$\frac{1}{DT}\frac{dT}{dt} = \frac{1}{X}\frac{d^2X}{dx^2} \; . \tag{6.4}$$

This equation will only be satisfied if both sides are equal to a constant. For our purposes, we will let that constant be a real, negative number, $-\lambda^2$. Thus we have reduced our partial differential equation into two ordinary differential equations,

$$T' + \lambda^2 DT = 0 \tag{6.5}$$

$$X'' + \lambda^2 X = 0 \; . \tag{6.6}$$

Solutions to these equations are of the form

$$T(t) = T_0 e^{-\lambda^2 Dt} \tag{6.7}$$

$$X(x) = A' \sin \lambda x + B' \cos \lambda x \; . \tag{6.8}$$

Because these solutions must hold for any value of λ, the sum of solutions with different values of λ is also a solution. Thus our solution for $c(x,t)$ becomes

$$c(x,t) = \sum_{n=1}^{\infty} e^{-\lambda_n^2 Dt} \left(A_n \sin \lambda_n x + B_n \cos \lambda_n x \right) \; . \tag{6.9}$$

Now we must apply our boundary and initial conditions in order to attain a workable solution. We begin with the scenario of oxygen diffusing out of the film.

$$\text{at } t = 0, \qquad c(x,0) = c_o \tag{6.10}$$

Additionally, we impose the constraint that at the surface, the oxygen content in the film is in equilibrium with the oxygen in gas phase. For the case of oxygen diffusion out of the film, there is only nitrogen in the gas. As oxygen is released into the gas phase, it is immediately pumped away, resulting in our assumption of a sustained partial pressure of oxygen at the surface equal to zero. Implicit in this analysis is the assumption that the surface kinetics of adsorption and absorption are sufficiently fast that diffusion in the bulk is the rate limiting step. Thus,

$$\text{at } x = 0, \qquad c(0,t) = 0 \; . \tag{6.11}$$

Finally, we know that at the back side of the film (against the substrate) there is no diffusive flux of oxygen. Hence,

$$\text{at } x = L, \qquad \frac{\partial c}{\partial x} = 0 \; . \tag{6.12}$$

Applying the first boundary condition to our solution yields

$$c(0,t) = \sum_{n=1}^{\infty} e^{-\lambda_n^2 Dt} \left(B_n\right) = 0 \; , \tag{6.13}$$

or

$$B_n = 0 \; . \tag{6.14}$$

In order to satisfy the second boundary condition, we find

$$\frac{\partial c(L,t)}{\partial x}=\sum_{n=1}^{\infty}e^{-\lambda_n^2 Dt}\lambda_n A_n\cos(\lambda_n L)=0\ . \tag{6.15}$$

Thus

$$\lambda_n L=(n+\frac{1}{2})\pi \tag{6.16}$$

Finally, we can apply the initial condition to find A_n.

$$c(x,0)=\sum_{n=1}^{\infty}A_n\sin\left((n+\frac{1}{2})\pi\frac{x}{L}\right)=c_o \tag{6.17}$$

Using knowledge of advanced trigonometry, we can solve for A_n. First we multiply both sides of the equation by $\sin\left[(p+\frac{1}{2})\pi\frac{x}{L}\right]$ and integrate over x from 0 to L.

$$\int_0^L c_o\sin\left((p+\frac{1}{2})\pi\frac{x}{L}\right)dx=\sum_{n=1}^{\infty}A_n\int_0^L\sin\left((p+\frac{1}{2})\pi\frac{x}{L}\right)\sin\left((n+\frac{1}{2})\pi\frac{x}{L}\right)dx \tag{6.18}$$

Now we find that each of the infinite number of integrals on the right side is equal to zero except when $p=n$, in which case the integral is equal to $\frac{L}{2}$. Putting it all back together gives us

$$A_n=\frac{2}{L}\int_0^L c_o\sin\left((n+\frac{1}{2})\pi\frac{x}{L}\right)dx=2c_o\frac{\left(1-\cos\left[(n+\frac{1}{2})\pi\right]\right)}{(n+\frac{1}{2})\pi}=\frac{2c_o}{(n+\frac{1}{2})\pi}\ . \tag{6.19}$$

Our final solution becomes

$$c(x,t)=\frac{2c_o}{\pi}\sum_{n=0}^{\infty}\frac{\sin\left[(n+\frac{1}{2})\pi\frac{x}{L}\right]}{(n+\frac{1}{2})}\exp\left(-\left[(n+\frac{1}{2})\frac{\pi}{L}\right]^2Dt\right)\ . \tag{6.20}$$

However, for our experiments we are most interested in the average concentration, $\overline{c}$,

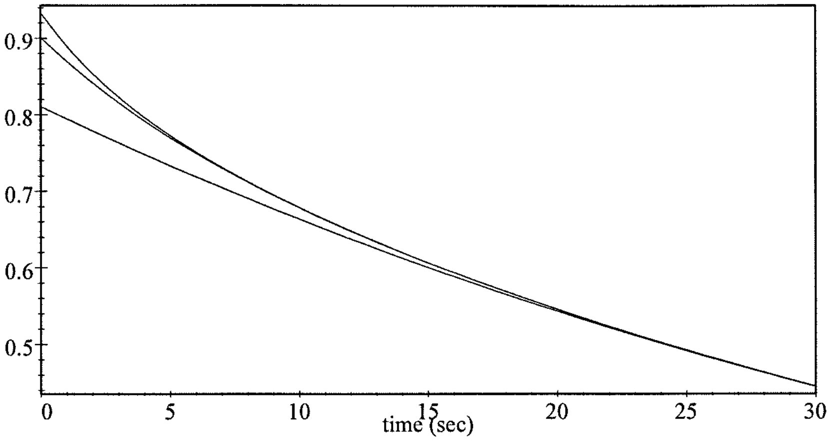

Figure 6.3: Plotted are the first three terms of $\frac{\bar{c}}{c_o}$, where τ is 50 seconds. The solid line is the 1^{st} term only, while the dashed line represents the 1^{st} and 2^{nd} terms, and the dotted line is for the 1^{st}, 2^{nd}, and 3^{rd} terms.

which can be calculated by integrating over x from 0 to L.

$$\bar{c}(t) = \frac{1}{L}\int_0^L c(x,t)dx \ , \tag{6.21}$$

$$\bar{c}(t) = \frac{2c_o}{\pi^2}\sum_{n=0}^{\infty}\frac{\exp\left(-\left[(n+\frac{1}{2})\frac{\pi}{L}\right]^2 Dt\right)}{(n+\frac{1}{2})^2} \ , \tag{6.22}$$

or

$$\frac{\bar{c}}{c_o} = \frac{8}{\pi^2}\left[e^{-t/\tau} + \frac{1}{9}e^{-9t/\tau} + \frac{1}{25}e^{-25t/\tau} + \ . \ . \ .\right] \ , \tag{6.23}$$

where τ is the time constant,

$$\tau = \frac{4L^2}{\pi^2 D} \ , \tag{6.24}$$

which is in agreement with the results presented in [134].

For long times, $t > \tau/3$, the first term is sufficient to describe the behavior of our

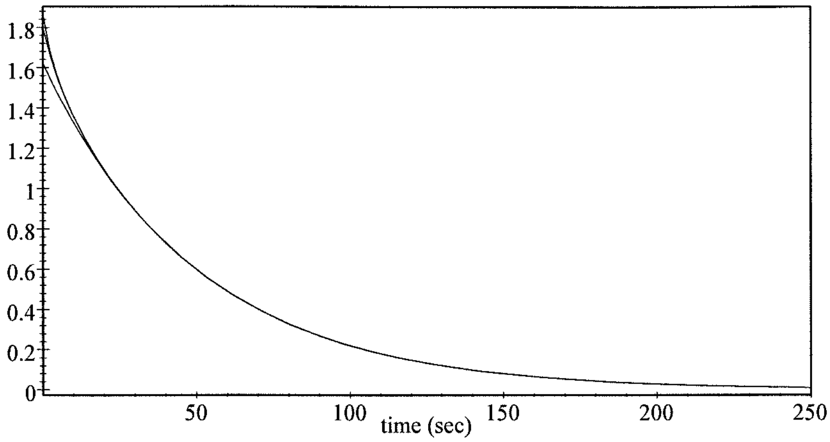

Figure 6.4: Presented is the same plot as in Figure 6.3. However, here the x-axis is extended to illustrate the full decay.

solution; see Figures 6.3 and 6.4.

6.2.1 Penetration Depth Considerations

As was mentioned in the introduction to this chapter, we performed ultraviolet reflectance measurements *in-situ* during transitions in oxygen stoichiometry. In the near-UV spectral region, there exists a peak, characterized by Kircher *et al.* [76], which increases in strength as oxygen concentration decreases. The peak is only present for $x < 6.73$, where x is defined in $YBa_2Cu_3O_x$. Recently it has been found that the 4.1 eV ($\sim$ 310 nm) transition originates from charge transfer transitions in the copper-oxygen chain planes at the bottom of the YBCO unit cell, consequent to the loss of oxygen at the O1 sites [12]. The following figure, Figure 6.5, illustrates this spectral feature.

Plotted below are the transient results of removing oxygen from the 500 nm thick YBCO film at 590 °C. In Figure 6.6 the change in swept area underneath the spectra (for a sample spectrum see Figure 6.5) versus time on a logarithmic scale; also plotted

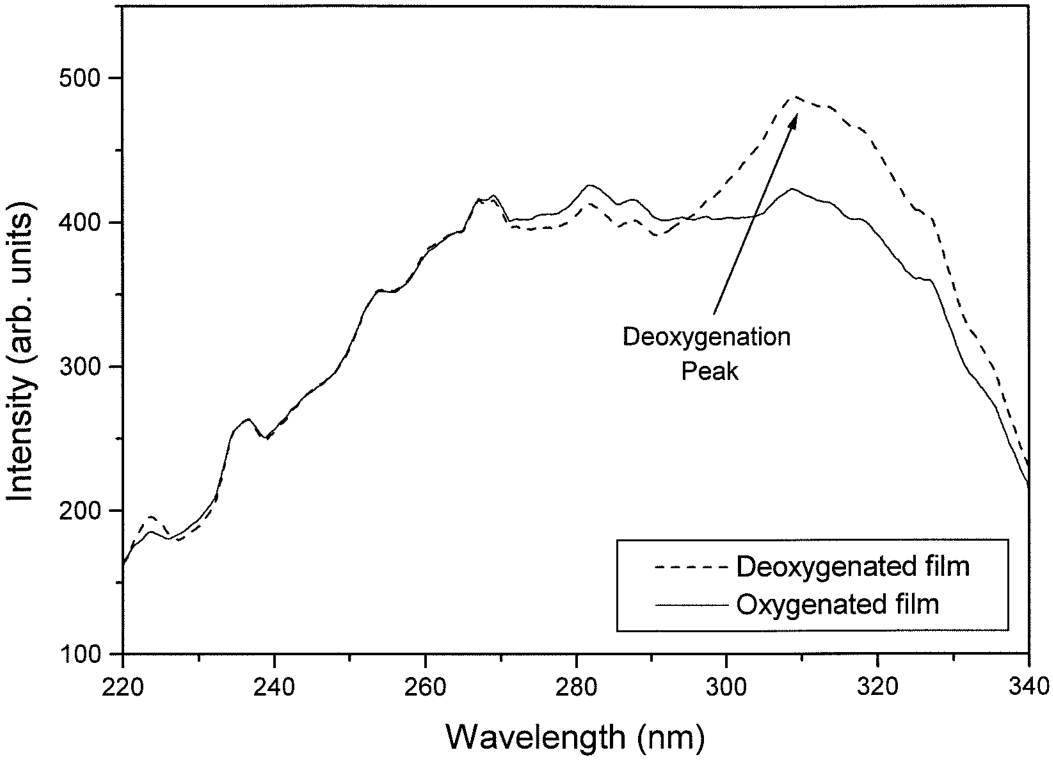

Figure 6.5: Raw ultraviolet reflectance spectra from a 500 nm thick YBCO film taken on October 24, 2000, at 485 °C. Dashed line is from the film before oxygen processing, while the solid line represents the fully oxygenated film.

in Figure 6.7 is the height of the 310 nm peak in the reflectance spectra of YBCO. The data is fit by a linear regression where the slope and intercept is listed along with the correlation coefficient in the upper right corner of each figure.

The difference between the two different time constants, $\tau_{area} = 1/slope = 8\,\mathrm{s}$, $\tau_{ph} = 1/0.0648 = 15\,\mathrm{s}$, can be explained by the variation in penetration depth. We know from [67] that the penetration depth, h, is the inverse of the absorption coefficient,

$$K = 4\pi\omega k \ , \tag{6.25}$$

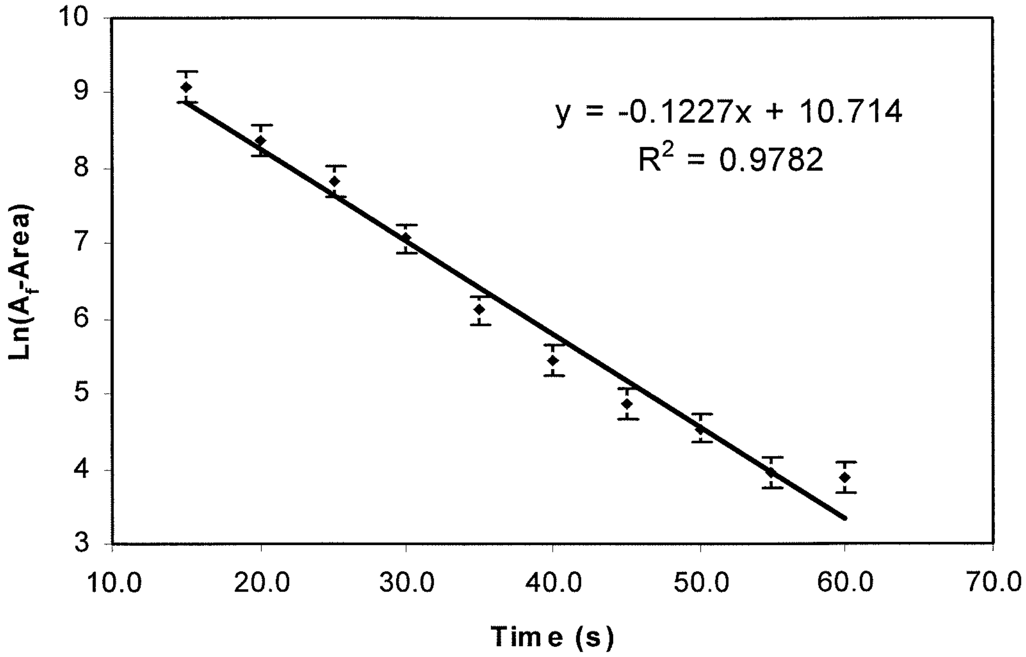

Figure 6.6: Exponential fit of the area beneath the reflected ultraviolet spectra measured from 220 nm to 340 nm versus time since the removal of gas phase oxygen from the 500 nm thick film surface at 590 °C.

where ω is the wavenumber ($\omega = 8066 \times E$ when ω is in cm^{-1} and the photon energy, E, is in eV), and k is the imaginary component of the index of refraction for YBCO,

$$N = r + ik \ . \tag{6.26}$$

For the experiment in question, the average penetration depth over the range 230-350nm is 35nm, while the penetration depth at the deoxygenation peak (300-330nm) averages 68nm [76]. Using the previous analysis for the exponential decay of the oxygen concentration over time, equation (6.20), we can look at the specific region

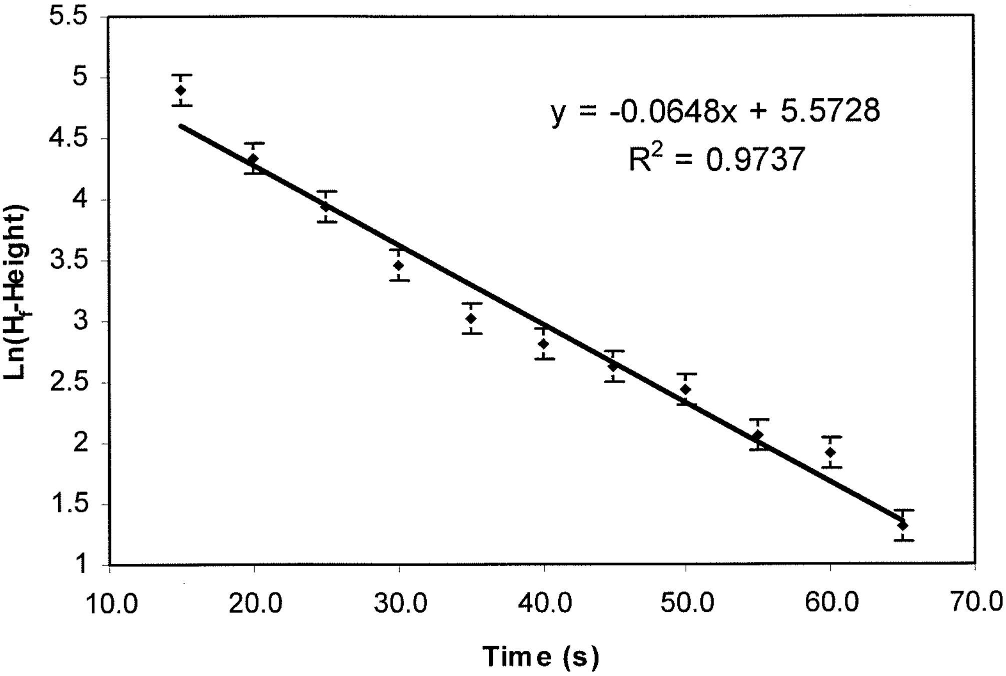

Figure 6.7: Exponential fit of reflectance peak height at 310 nm versus time since the removal of gas phase oxygen from the 500 nm thick film surface at 590 °C.

seen by the ultraviolet spectroscopy.

$$\overline{c_{uv}}(t) = \frac{1}{h}\int_0^h c(x,t)dx \ , \tag{6.27}$$

$$\overline{c_{uv}}(t) = \frac{2c_o}{\pi^2}\frac{L}{h}\sum_{n=0}^{\infty}\left(1-\cos\left[(n+\frac{1}{2})\frac{h}{L}\pi\right]\right)\frac{\exp-\left[(n+\frac{1}{2})\frac{\pi}{L}\right]^2 Dt}{(n+\frac{1}{2})^2} \ . \tag{6.28}$$

For our penetration depth of 35nm,

$$1-\cos\left[(n+\frac{1}{2})\frac{h}{L}\pi\right] = 0.006, 0.05, 0.15, 0.28, \ . \ . \ . \tag{6.29}$$

The following table demonstrates the contribution of the cosine term in the infinite sum, equation (6.29), for the three cases of total penetration depth, $h = L$, a depth

Table 6.1: The coefficients for the first ten exponential terms in the solution for concentration are listed below. The columns include results for the entire film thickness, $\bar{c}$, and the two penetration depths discussed in the text, $\overline{c_{uv-area}}$ and $\overline{c_{uv-ph}}$.

term	$\bar{c}$	$\overline{c_{uv-area}}$	$\overline{c_{uv-ph}}$
1^{st}	1	.006	.0023
2^{nd}	.11	.006	.022
3^{rd}	.04	.0059	.021
4^{th}	.02	.0058	.019
5^{th}	.012	.0056	.017
6^{th}	.0083	.0053	.014
7^{th}	.0059	.0051	.011
8^{th}	.0044	.0048	.0089
9^{th}	.0035	.0045	.0065
10^{th}	.0028	.0041	.0045

of $h = 35\,\text{nm}$, and a penetration depth of $h = 68\,\text{nm}$.

The first column of values, $\bar{c}$, is the term by term coefficients in the solution for average oxygen concentration across the entire thickness of the film,

$$\frac{\bar{c}}{c_o} = \frac{16}{\pi^2}\left[e^{-t/\tau} + \frac{1}{9}e^{-9t/\tau} + \frac{1}{25}e^{-25t/\tau} + \ .\ .\ .\right]. \tag{6.30}$$

As illustrated in Figures 6.8 and 6.9, it would be inappropriate to fit the ultraviolet data to a simple first order exponential decay. As mentioned in the introduction, the data presented by Aarnink *et al.* [2] consistently underpredicts the decay constants, and hence overpredicts the diffusion constants. In fact, they recognized this fact, "Because the optical penetration depth is smaller than our film thickness, the obtained values may be too high. On the other hand, the penetration depth varies with energy and oxygen content, whereas the film thickness is a real constant." We also observe this trend to underpredict time constants in our data when ultraviolet reflectance data is compared to CGS data. As will be shown, the time constant for the same

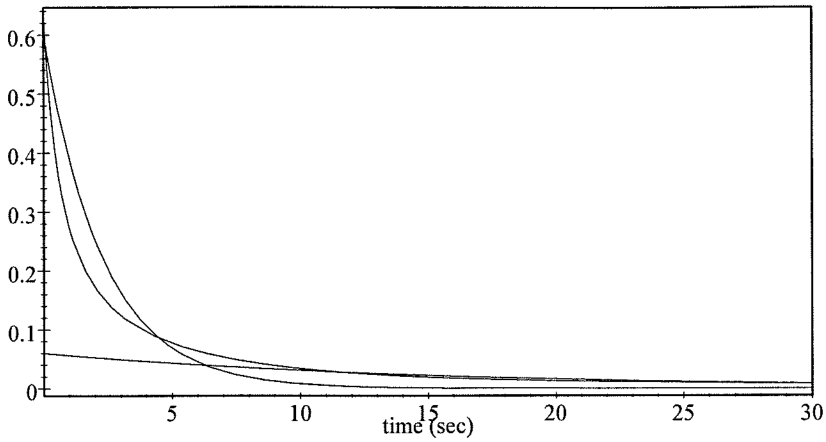

Figure 6.8: Pictured above are the first 7 terms of the normalized oxygen concentration for a penetration depth of 68 nm (short dashed line, $\tau = 50s$). Also included are the two closest match single-term exponential fits (solid line, $\tau = 2.3s$ fits the early portion of the decay) and (long dashed line, $\tau = 15s$).

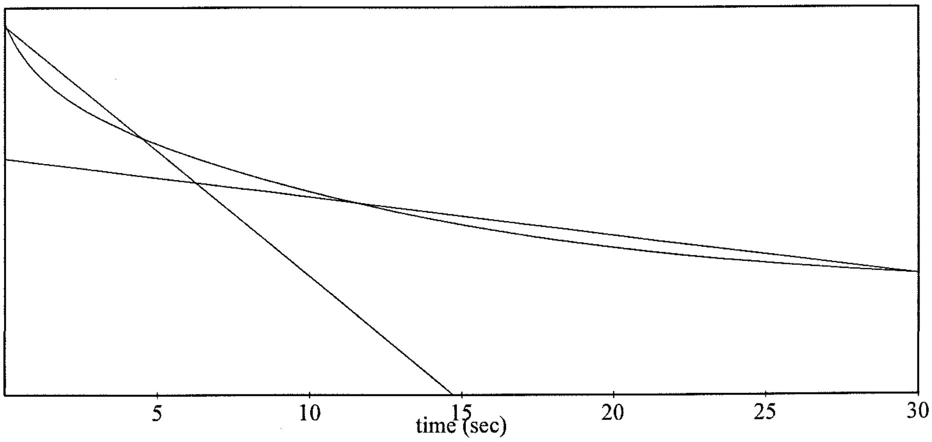

Figure 6.9: A further illustration of the curves depicted in figure 6.8, presented with a logarithmic y-axis.

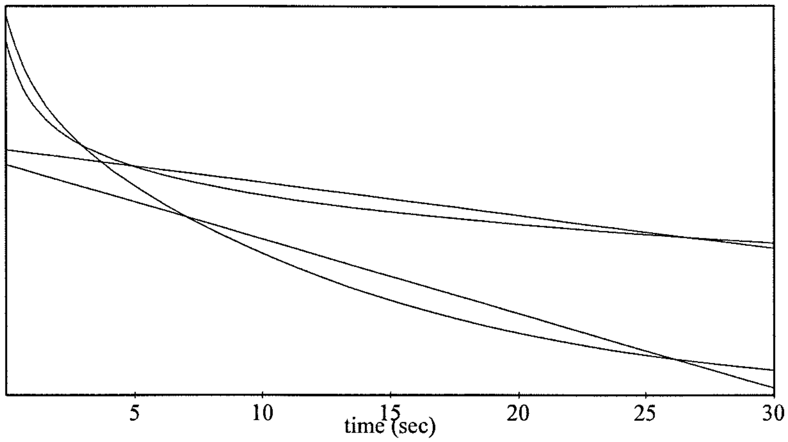

Figure 6.10: Average normalized oxygen concentrations as computed for the first 7 terms with a decay constant of $\tau = 50\,\mathrm{s}$ versus the closest single term exponential fit. Solid curved line is for a penetration depth of 35nm, while the dashed curved line is for a penetration depth of 68nm. Of the straight lines, the dashed corresponds to a $\tau = 25\,\mathrm{s}$ and the solid straight line corresponds to a $\tau = 11\,\mathrm{s}$.

film under the same conditions as calculated from CGS data is $\tau = 28\,\mathrm{s}$ (versus the 8 s and 15 s found earlier for the UV data). Hence, although ultraviolet spectroscopy (and spectroscopic ellipsometry) is an excellent tool for measuring oxygen content in YBCO for steady state conditions, it is a poor choice for measuring transient phenomenon such as oxygen diffusivity (unless of course the film thickness is equal to the penetration depth at the frequency of interest).

The discrepancy between our time constants as calculated for the curve area, Figure 6.6, and peak height, Figure 6.7, is depicted in Figure 6.10.

6.3 Experimental

Real-time *in-situ* measurements were carried out in a stainless steel, cylindrical, cold-walled, vertical, stagnation-flow MOCVD reactor [148]. A series of mass flow controllers and actuated pumping allows for a constant background pressure of 10 torr to be maintained throughout all experiments. Flows of O_2 and N_2 gases ranged from 0 to 8 slm. Wafer temperature measurement was made through direct thermocouple contact with the top exposed surface of the wafer. Temperature is controlled with a feedback loop wrapped around a thermocouple placed inside the inconel can which supports the wafer and encloses the heaters. Typical heating rates were 2.5°C/min.

The CGS optical setup is as described in Chapter 5 and depicted in Figure 6.1, with the grating spacing increased to 6 inches. The sensitivity of the CGS setup in this arrangement is greater than 0.01 m^{-1} [20]. Interferometer images were again captured on a Sony TRV43 Hi8 camcorder.

The MOCVD of YBCO on MgO samples are well oriented c-axis polycrystalline and were supplied by Superconducting Technologies Inc. [105]. The respective curvatures of the bare substrates were not measured prior to production; however, the curvature of supplied MgO substrates typically have a radius of curvature less than $0.01\,m^{-1}$. XRD results show the presence of strictly 1:2:3 phase YBCO with a c-axis length of 11.69 Å and 11.71 Å. Susceptibility measurements indicate a $T_c = 87.7\,°C$ and 90.5 °C and $\Delta T_c \sim 1\,°C$. Reference [105] further details the high quality nature of the supplied samples.

The samples were heated in an environment of pure nitrogen. Once the desired temperature of the wafer was reached, a molecular oxygen environment was initiated along with video recording of the fringe pattern. Later once the stress pattern has reached a steady state, the oxygen environment is replaced with nitrogen until once again the stress pattern has reached a steady state. This pattern was often repeated up to three times.

The analysis presented in Chapter 5 serves to relate the number of fringes in the interferogram with the oxygen concentration in the YBCO film. Because we are only concerned with changes in stoichiometry, and hence changes in curvature or fringe

Figure 6.11: Pictured is a 500 nm wafer in a stressed state of low oxygen content (left) and the same wafer in a less stressed state of high oxygen content (right).

numbers, the CGS technique is insensitive to any initial curvature of the sample.

Also mentioned in Chapter 5, we use a video recording to allow the counting of the number of bright fringes present in a CGS inteferogram of the wafer. Shown in Figure 6.11 are two opposite conditions of oxygenation for a given wafer. On the left, the fringe count is 5.2 (bright fringes) which corresponds to a deoxygenated state. On the right, a fringe count of 4 corresponds to full oxygenation at 590 °C.

The tabulated fringe count values are plotted versus time at which point the asymptote of the exponential decay is determined. Once the choice of asymptote has been made (1.5 in the case depicted in Figure 6.12), the oxygenation fringe count data minus the asymptote value (for the case of deoxygenation, the fringe count data is subtracted from the asymptote) is plotted logarithmically, and a linear regression analysis is performed to identify the time constant; the same data from Figure 6.12 is again depicted in Figure 6.13 to show the exponential fitting. In this instance, the time constant is $\tau = 13.4\,\mathrm{s}$, and with a slight modification to equation (6.24), the

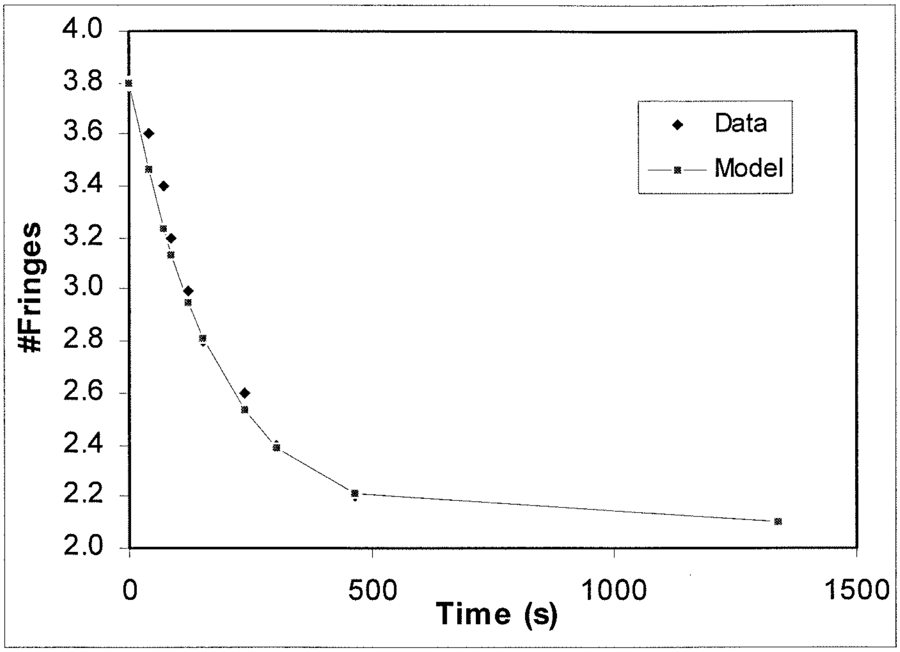

Figure 6.12: Second oxygenation of a 500 nm YBCO film at a temperature of 585 °C.

diffusion constant becomes

$$D = \frac{4L^2}{\pi^2 \tau} = 7.6 \times 10^{-11}\,\mathrm{cm}^2/\mathrm{s}\ . \tag{6.31}$$

Data was collected for two separate films. Both were initially 700 nm, however 200 nm was removed from one of the films via an ion plasma milling operation. Because the diffusion constant is a function of both the time constant and the film thickness, our intent was to correlate these calculations across both variables. In order to attain several distinct values of the time constant, we experimented with four different film temperatures: 485 °C, 510 °C, 585 °C, and 640 °C. To investigate the repeatability of the results, multiple repetitions of the experiment were immediately performed at most of the temperature points.

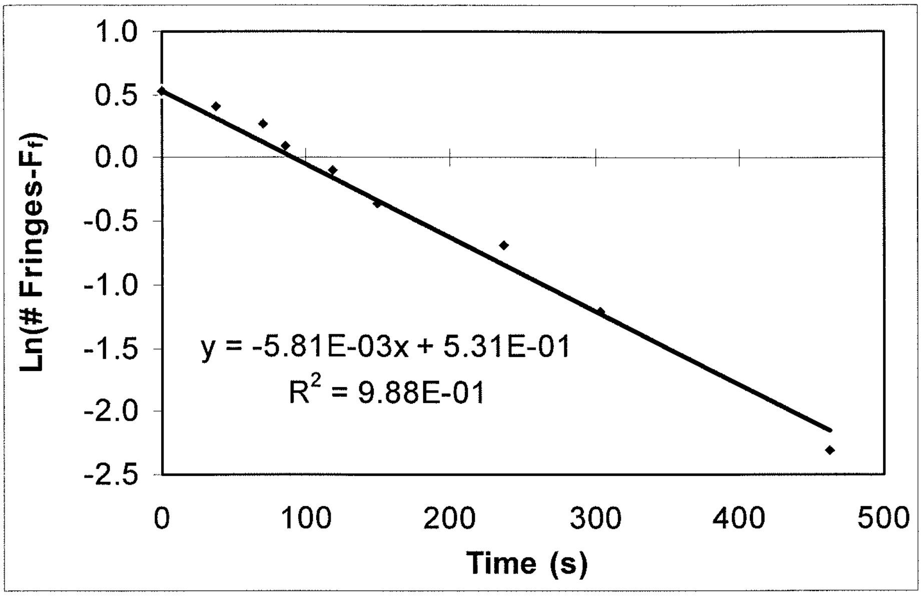

Figure 6.13: Second oxygenation of a 500 nm film at 585 °C illustrated with linear regression parameters: slope, intercept, and correlation coefficient.

6.4 Results and Discussion

The results of our experiments are presented in tables 6.2 through 6.5. All of the raw data is presented in Appendix C in graphical form similar to Figure 6.12.

YBCO undergoes a phase transition from an orthorhombic to a tetragonal lattice structure within the temperature and oxygen stoichiometry range of our experiments [73]. The effect of this phase transition on the stress pattern of the wafer is not obvious. Table 6.6 illustrates which temperatures were subject to the transition. However, experimental results from 485 °C and 510 °C, wherein the material crossed the phase boundary, appeared no different from those at higher temperatures.

One of the most intriguing aspects of the data collected is a repeatable occurrence of a first run transient. At higher temperatures (640 °C), all of the data exhibits a fast and slow component for oxygen in diffusion, which can be traced to the removal of lightly bound oxygen first, and more tightly bound oxygen at higher activation

Table 6.2: The results of our oxygenation CGS experiments on the thin wafer are listed below. An initially deoxygenated film is exposed to $P_{O_2} \geq 9\,\text{torr}$, while being monitored by CGS interferometry.

Wafer Thickness =	500 nm	Oxygenation
Temperature(°C)	Tau (s)	Diffusivity $\left(\frac{\text{cm}^2}{\text{s}}\right)$
485	172	5.9×10^{-12}
510	17.5	5.8×10^{-11}
	11.7	8.7×10^{-11}
	13.4	7.6×10^{-11}
585	18.0	5.6×10^{-11}
	13.4	7.6×10^{-11}
	8.5	1.2×10^{-10}

Table 6.3: The table below represents the results of our deoxygenation CGS experiments on the thin wafer. An initially oxygenated film is exposed to $P_{O_2} \leq 0.1\,\text{torr}$, while being monitored by CGS interferometry.

Wafer Thickness =	500 nm	Deoxygenation
Temperature(°C)	Tau (s)	Diffusivity $\left(\frac{\text{cm}^2}{\text{s}}\right)$
485	830	1.2×10^{-12}
510	221	4.6×10^{-12}
	133	7.6×10^{-12}
	134	7.6×10^{-12}
585	47	2.2×10^{-11}
	44	2.3×10^{-11}
590	24	4.3×10^{-11}

Table 6.4: The table below represents the results of our oxygenation CGS experiments on the thick wafer. An initially deoxygenated film is exposed to $P_{O_2} \geq 9\,\text{torr}$, while being monitored by CGS interferometry.

Wafer Thickness =	700 nm	Oxygenation
Temperature(°C)	Tau (s)	Diffusivity $\left(\frac{\text{cm}^2}{\text{s}}\right)$
510	498	4.0×10^{-12}
585	235	8.5×10^{-12}
	68.5	2.9×10^{-11}
590	287	6.9×10^{-12}
640	51.0	3.9×10^{-11}
	100	2.0×10^{-11}
	112	1.8×10^{-11}

Table 6.5: The table below represents the results of our deoxygenation CGS experiments on the thick wafer. An initially oxygenated film is exposed to $P_{O_2} \leq 0.1$ torr, while being monitored by CGS interferometry.

Wafer Thickness =	700 nm	Deoxygenation
Temperature(°C)	Tau (s)	Diffusivity $\left(\frac{\text{cm}^2}{\text{s}}\right)$
585	832	2.4×10^{-12}
	159	1.3×10^{-11}
590	1071	1.9×10^{-12}
640	223	8.9×10^{-12}
	176	7.5×10^{-11}
	265	8.9×10^{-12}

Table 6.6: Equilibrium oxygen concentration and phase information is listed for each of our experimental conditions. Data courtesy of [14, 58].

Temp (°C)	x ($P_{O_2} = 9$ torr)	Phase	x ($P_{O_2} = 0.1$ torr)	Phase
485	6.71	Orthorhombic	6.31	Tetragonal
510	6.68	Orthorhombic	6.27	Tetragonal
585	6.5	Tetragonal	6.14	Tetragonal
590	6.48	Tetragonal	6.12	Tetragonal
640	6.38	Tetragonal	6.08	Tetragonal

energies [158]. However, at the lower temperatures, there is a much more sporadic presence of fast and slow diffusivity components. As an example, consider the case of oxygen in diffusion at 585 °C with the thin wafer.

For the initial oxidation, there are two regimes clearly evident, as shown in Figure 6.14. The first regime is for a fast component of diffusion (lighter shaded diamond shapes) and has a time constant of $\tau = 6.7$ s, while the second regime represents a slower component of the diffusion which becomes apparent once the fast component expires. The slower component is represented by the darker shaded square shapes, and has a time constant, $\tau = 25.3$ s. The time constant listed in table 6.2 is illustrated by the thick black line and the matching linear regression (equation in bold), where the time constant is $\tau = 18.0$ s. As such, our results constitute an effective diffusion constant for oxygen in YBCO, rather than an absolute diffusivity.

The subsequent oxidation experiments for the same experimental conditions are illustrated in Figure 6.15. Notice that although the diffusion does become faster, it remains tightly adhered to a single exponential term. In each of the subsequent runs the time constant is reduced, going from $\tau = 13.4$ s in the second oxidation run to a quicker $\tau = 8.5$ s for the third and final oxidation.

In our search for an explanation of the disparate fast and slow components, we first investigated the flow conditions within the reactor. With a careful examination of the data file from this experiment, it was determined that the total time required for the flow to transition from N_2 to O_2 including residence time in the showerhead and chamber is slightly less than 15 seconds at the prescribed flowrates of 8 slm. The residence time was calculated to be less than 2 seconds using a displaced volume of 6 liters (12 in high × 5.25 in ID).

Another possible explanation for the two distinct diffusion speeds is a secondary activation energy required to create atomic oxygen from molecular oxygen [169]. In fact, one group [80] has found that their YBCO films, created by pulsed laser deposi-

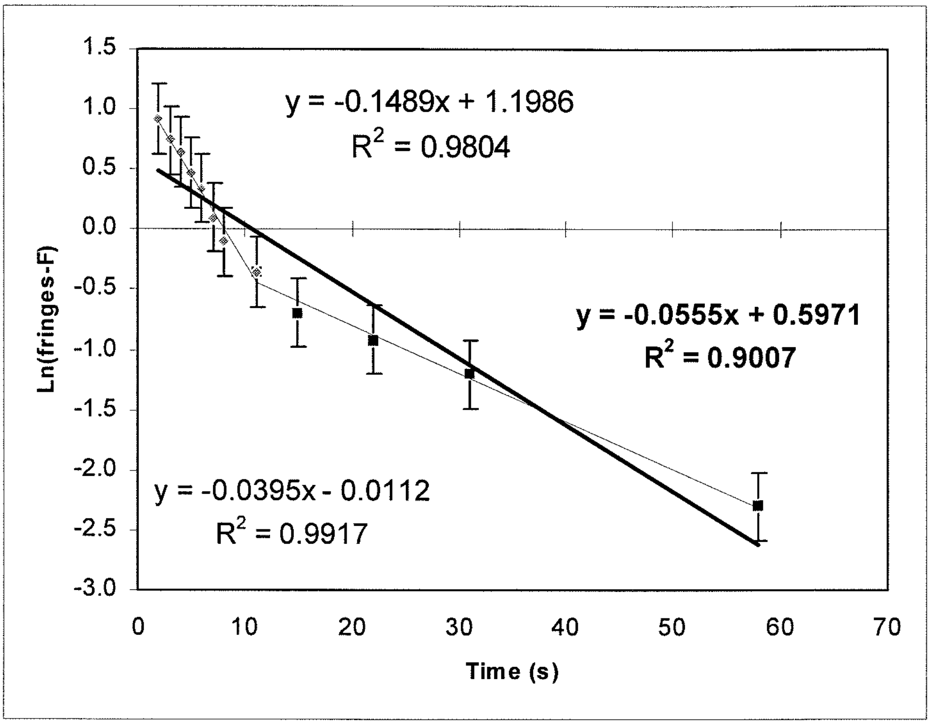

Figure 6.14: Exponential fits of the initial oxidation of a 500 nm at 585 °C. Fast and slow components are clearly evident in the diffusion of oxygen. Note that the error bars are calculated based on the overall fit (bold equation and thick line), and not the individual component fits.

tion (PLD), undergo a microstructural transformation at the surface of the film only on the initial heating with exposure to oxygen. They postulate that the film creates a-axis grains at the surface which act as a catalyst to increase the quantity of atomic oxygen available at the surface of the film.

As we have already derived the solution for concentration, equation (6.23), the transient components could simply be the latter terms in the summation. As the overall diffusion gets faster, the amount of time during which the latter terms affect the solution becomes less and less. Thus the initial oxidation would exhibit the effect of $\frac{1}{9}e^{-9t/\tau}$ and $\frac{1}{25}e^{-25t/\tau}$, while the later oxidations would not. However, these terms would act to speed up the diffusion at first, and this scenario was only present at

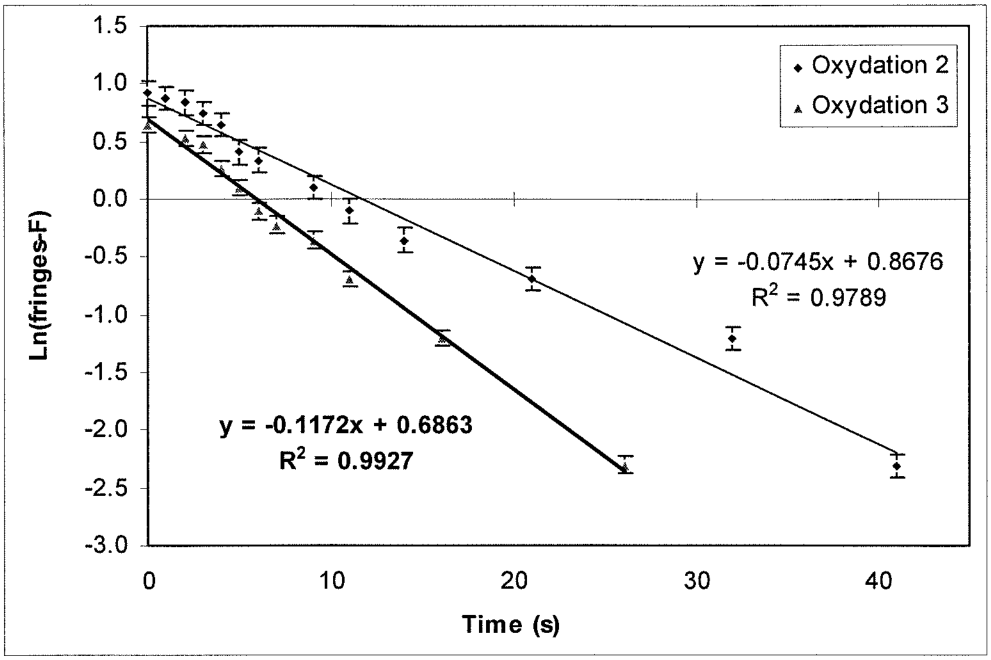

Figure 6.15: Secondary oxidation of the 500 nm film at 585 °C exhibit a uniform diffusion rate of oxygen into the film. Note that the error bars are calculated based on the overall fit for each set of data.

temperatures of 510 °C and below.

Additional transient effects can come from the phase transition, grain boundary diffusion, or the stoichiometry contribution to the diffusivity. In our case, in-diffusion is significantly faster than out-diffusion. This makes intuitive sense because when the oxygen content is initially low (at the start of in-diffusion) there are plenty of vacancies available to allow the oxygen atoms to move easily. When the vacancies fill up and the oxygen content is high, there is not as much oxygen mobility, and the atoms cannot reach the surface to diffuse out as quickly as they came in. This view is supported by the literature [153, 55, 152, 169, 86, 83]. In fact Patrakeev *et al.* [113] showed that the diffusion constant varied from 1.3×10^{-6} to 6.3×10^{-6} to 35×10^{-6} for $YBa_2Cu_3O_{6+x}$ at 1000 K, where x varies from 0.35 to 0.45 to 0.55 respectively.

The difference between the values of the diffusion constant for the different film

Figure 6.16: Arrehenious plot of diffusion constants for oxygen in YBCO.

thicknesses warrants some discussion as well. Yamamoto *et al.* [169] showed that films with different microstructures (as deposited on different substrates) had diffusion constants which differed by nearly one and a half orders of magnitude. Additionally, the condition of the film surface can dramatically affect the diffusion rate [80]. As such, the obvious conclusion is that the ion milling procedure which was used to remove material from the 500 nm film altered the surface condition, and hence the apparent diffusion rate of the film.

Nonetheless, our data agrees very well with the literature for c-axis oriented thin films; see Figure 6.16. For in-diffusion of oxygen at 600 °C, references [83, 122] quote diffusivities of approximately 2×10^{-10} cm^2 / s for bulk YBCO material, while references [83, 169] quote diffusivities of 2×10^{-12} cm^2 / s for thin films. Notice the high variability of the published experimental data; through analysis of our results from run to run and film to film, we are confident that the values presented are accurate to within a factor of 2 (*i.e.*, less than half of one order of magnitude).

6.5 Conclusion

We have shown that CGS is an effective technique for observing oxygen diffusion in YBCO. In addition we have provided experimental data for the diffusivity of oxygen in YBCO created by MOCVD. Unique diffusivity data is presented for several different operating temperatures, and two different film thicknesses. The studies have confirmed the presence of fast and slow components in the diffusion process, and they have revealed interesting differences between oxygen in-diffusion and out-diffusion for YBCO.

Chapter 7 Conclusion

We have demonstrated the ability to intelligently design and construct an MOCVD facility for thin film deposition of $YBa_2Cu_3O_{7-\delta}$. After thorough numerical and analytical modeling, the reactor design resulted in a flexible system capable of extensive sensing and diagnostics, uniform film deposition, and accurate monitoring of wafer temperature, thickness, and curvature. The reactor includes adaptive closed-loop control of precursor stoichiometry, chamber pressure, flowrates, gas handling system temperature, and wafer temperature. Furthermore, the warm wall design permits the use of extensive *in-situ* sensors and diagnostics.

A Fourier Transform Infrared (FTIR) spectrometer has been integrated into the design from the beginning. Using the FTIR we have collected polarized infrared reflectance spectra during film growth. The growth temperature has been calibrated by monitoring the temperature dependant spectral position of the MgO Restrahlen band edge near $800\,\mathrm{cm}^{-1}$ and referencing to a thermocouple in direct contact with the substrate. Gradual disappearance of the Restrahlen band during YBCO deposition has also provided qualitative feedback on film thickness.

As evidence of reactor uniformity, we have calculated the precise thickness of a BaO film at the center and outermost edge of a 2 inch substrate; the resultant non-uniformity is 2%. In addition to film thickness, we characterized the uniformity of the gas flow reaching the substrate using a quadrupole mass spectrometer.

C-axis oriented epitaxial $YBa_2Cu_3O_7$ has been grown, and by comparison with published results, we do not see the presence of any a-axis grains nor of any off-stoichiometric compounds. The calculated c-axis length is comparable to the best fully oxygenated crystalline films, while XRD rocking curve analysis indicates a low degree of c-axis wobble. Typical stoichiometries of the films, as measured by RBS are 0.185 : 0.288 : 0.527 for Y : Ba : Cu. This value compares very favorably with published optimum stoichiometries of 0.187 : 0.280 : 0.533.

Coherent gradient sensing, a novel, real-time, full-field optical technique, which provides a direct map of the components of the curvature tensor across the entire surface of the wafer, has been implemented on an MOCVD deposition chamber for the first time. Along with film growth investigations, stress analyses of YBCO films during heating and cooling of the film/substrate were demonstrated for different operating conditions. The CGS laser-interferometric technique was also used to observe the expected shift in the orthorhombic to tetragonal phase transition of YBCO with temperature and O_2 concentration.

Moreover, CGS was implemented in an *in-situ* study of oxygen diffusion in YBCO. Unique data was presented on the diffusion rates of oxygen in YBCO films grown by MOCVD. Oxygen concentrations were also investigated with ultraviolet spectrometry, and a theoretical analysis of one-dimensional thin film diffusion was carried out. For a variety of experimental conditions, oxygen diffusion constants have been provided which are in close agreement with published data for other types of YBCO thin films.

7.1 Future Directions

Now that accurate measurements of oxygen diffusion in YBCO grown by MOCVD are available, the post-growth annealing processes can be properly refined. STI has found that their films are often over-oxidized after growth, and a brief annealing in nitrogen yields optimal material properties. Most groups, however, produce YBCO which requires a post-growth anneal in oxygen to complete the oxidation. For either case, our results will permit the optimization of these annealing steps, making possible the precise calculation of the time and temperature required.

The results of our FTIR analyses open up opportunities for process improvement and deeper process understanding. By closing a control loop around the real-time FTIR results, accurate control of growth rate and film temperature is possible. The FTIR system can also be used with an external beam arrangement to investigate gas phase chemistry inside the reactor.

Studies by Hitchman *et. al.* [63, 82] have shown the decomposition of YBCO precursors through analysis by FTIR in an external tube furnace. Because of the unique diagnostic access to our MOCVD system, FTIR analysis could be used to further study this decomposition within the growth environment. Profiling of the species with respect to distance from the substrate may also be possible.

Although the optical setup would be quite complex, it is possible to use ultraviolet spectroscopy in a manner similar to that for FTIR mentioned above. The same spectral features which allow our system to accurately control the flowrates of the metal precursors can be used to monitor the breakdown of the precursor. As the precursors travel from the showerhead to the substrate, they are heated and reacted with oxygen, which causes the spectral peaks illustrated in Chapter 2 to diminish. Since the ultraviolet beam is easily collimated into a small area (1-2 cm^2), more precise height correlated information is attainable. Either *in-situ* FTIR or UV spectrometry of the gas phase chemistry within the reactor could potentially provide invaluable data for MOCVD modelling efforts.

Recently, discussions of adapting the MOCVD reactor for thin film growth of other materials have arisen. This reactor could potentially deposit almost any type of metal-oxide thin film, for example other Perovskite thin films, including ferroelectric materials such as barium titanate or lead titanate, could be produced relatively easily.

Once a new material system has been established in the reactor, the task of analyzing the growth and material properties with CGS, FTIR, and UV spectrometry becomes very tractable. Diffusion experiments involving oxygen transport within the crystals are equally accessible given the prior work on oxygen diffusion and the present status of the MOCVD facility. Because of the flexible nature and extensive diagnostic tools available on our MOCVD system, a wealth of opportunities are available for the study of numerous processes and materials.

Bibliography

[1] W.M. Kays and M.E. Crawford, *Convective Heat and Mass Transfer*, McGraw-Hill, New York (1980)

[2] W.A.M. Aarnink, R.P.J. Ijsselsteijn, J. Gao, A. Van Silfhout, and H. Rogalla, Phys. Rev. B, **45**, 13002 (1992)

[3] H. Adachi, K. Setsune, T. Mitsuyu, K. Hirochi, Y. Ichikawa, T. Kamada, and K. Wasa, Jpn. J. Appl. Phys., **26**, L709 (1987)

[4] F. Anderegg, X.P. Huang, E. Sarid, and C.F. Driscoll, Rev. Sci. Instr., 68, 2367 (1997)

[5] D.E. Aspnes, IEEE J. Select. Topics Quant. Elec., 1, 1054 (1995)

[6] S. Auzary, K.F. Badawi, L. Bimbault, J. Rabier, R.J. Gaboriaud, and P. Goudeau, J Phys III, **7**, 35 (1997)

[7] S. Auzary, F. Badaw, L. Bimbault, J. Rabier, and R.J. Gaboriaud, J of Alloys and Compds, **251**, 37 (1997)

[8] A.R. Barron and W.S. Rees, Adv. Mater. Opt. Electron., **2**, 271 (1993)

[9] J. Bassas, X. Alcobe, M. Doudowsky, J. Santiso, S. Berton, and A. Figueras, Mater. Sci. Forums, **278-281**, 478 (1998)

[10] J.G. Bednorz and K.A. Muller, Z. Phys. B, **64**, 189 (1986)

[11] A.D. Berry, D.K. Gaskill, R.T. Holm, E.J. Cukauskas, R. Kaplan, and R.L. Henry, Appl. Phys. Lett., **52**, 1743 (1988)

[12] M.E. Bijlsma, H. Wormeester, D.H.A. Blank, E.A.F. Span, A. VanSilfhout, and H. Rogalla, Phys. Rev. B. **57**, 13418 (1998)

[13] N. Blayo and B. Drevillon, Appl. Phys. Lett., 57, 786 (1990)

[14] R. Bormann and J. Nolting, Appl. Phys. Lett. **54**, 2148 (1989)

[15] M. Born and E. Wolf, *Principles of Optics*, Pergamon Press, New York (1986)

[16] A. M. Bratkovsky, V. Heine, and E.K.H. Salje, Philos T Roy Soc A, **354**, 2875 (1996)

[17] S.I. Bredikhin, G.A. Emelchenko, V.S. Shechtman, A.A. Zhokhov, S. Carter, R.J. Chater, J.A. Kilner, and B.C.H. Steele, Physica C, **179**, 286 (1991)

[18] W. Breiland and G. Evans, J. Electrochem. Soc., **138-6**, 1806 (1991)

[19] D. Briggs and M.P. Seah, *Practical Surface Analysis Volume 1*, John Wiley & Sons, New York (1983)

[20] H.A. Bruck and A.J. Rosakis, Optics and Lasers in Engineering **18**, 25 (1993)

[21] J.M. Buriak, L.K. Cheatham, R.G. Gordon, J.J. Graham, and A.R. Barron, Eur. J. Solid State Inorg. Chem., **29**, 43 (1992)

[22] H. Busch, A. Fink, A. Muller, and K. Samwer, Supercond. Sci. Technol., **6**, 42 (1993)

[23] A.F. Bykov, P.P. Semyannikov, and I.K. Igumenov, J. Therm. Analysis, **38**, 1477 (1992)

[24] A.F. Bykov, P.P. Semyanikov, and I.K. Igumenov, J. Therm. Analysis, **38**, 1463 (1992)

[25] A.F. Bykov, A.E. Turgambaeva, and I.K. Igumenov, Russ. J. Coord. Chem., **22**, 397 (1996)

[26] R.J. Cava, B. Batlogg, C.H. Chen, E.A. Rietman, S.M. Zahurak, and D. Werder, Phys. Rev. B, **36**, 5719 (1987)

[27] Y.X. Chen, J. Zhang, and Z. Wu, Supercond. Sci. Technol., **5**, 463 (1992)

[28] W.K. Cho, D.H. Choi, and M.U. Kim, Int. J. Heat Mass Transfer, **42**, 4143 (1999)

[29] M.E. Coltrin, R.J. Kee, and J.A. Miller, J. Electrochem. Soc., **131**, 425 (1984)

[30] K. Conder and C. Kruger, Physica C, **262**, 92 (1996)

[31] B.D. Cullity, *Elements of X-ray Diffraction*, Addison-Wesley, Reading, MA (1978)

[32] K.H. Dahmen and T. Gerfin, Prog. Crystal Growth and Charact., **27**, 117 (1993)

[33] W.J. Desisto and B.J. Rappoli, J. Crystal Growth **191**, 290 (1998).

[34] P.H. Dickinson, T.H. Geballe, A. Sanjurjo, D. Hildenbrand, G. Craig, M. Zisk, J. Collman, S.A. Banning, and R.E. Sievers, J. Appl. Phys., **66**, 444 (1988)

[35] D. Dijkkamp, T. Venkatesan, X.D. Wu, S.A. Shaheen, N. Jisrawi, Y.H. Min-Lee, W.L. Mclean, and M. Croft, Appl. Phys. Lett., **51**, 619 (1987)

[36] L. Doolittle, Nucl. Instrum. Methods B, **9**, 344 (1985)

[37] L. Doolittle, Nucl. Instrum. Methods B, **15**, 227 (1986)

[38] A.A. Drozdov, S.I. Troyanov, N.P. Kuzmina, L.I. Martynenko, A.S. Alikhanyan, and I.P. Malkerova, J. Phys. (Paris) IV, Colloq., **5**, C3-379, (1993)

[39] A. Drozdov and S. Troyanov, J. Phys. (Paris) IV, Colloq., **5**, C5-373, (1995)

[40] M. Doudkowsky, J. Santiso, S. Berton, A. Figueras, and J. Bassas, Chemical Physics, **288**, 1 (1997)

[41] N.E. Fedotova, I.K. Igumenov, V.I. Mamtyuk, and G.V. Sidorenko, J. Phys. (Paris) IV, Colloq., **5**, C5-431, (1995)

[42] D.B. Fenner, D.K. Fork, J.B. Boyce, G.A.N. Connell, and A.M. Viano, Physica C, **162**, 141 (1989)

[43] D.B. Fenner, A.M. Viano, D.K. Fork, G.A.N. Connel, J.B. Boyce, F.A. Ponce, and J.C. Tramontana, J. Appl. Phys., **69**, 2176 (1991)

[44] P.A. Flinn, D.S. Gardner, and W.D. Nix, IEEE Trans. Electron. Devices, **34**, 689 (1987)

[45] J.A. Floro, E. Chason, S.R. Lee, R.D. Twesten, R.Q. Hwang, and L.B. Freund, J. Electr. Mater., **26**, 969 (1997)

[46] J.A. Floro, E. Chason, R.D. Twesten, R.Q. Hwang, and L.B. Freund, Phys. Rev. Lett., **79**, 3946, (1997)

[47] J.A. Floro, G.A. Lucadamo, E. Chason, L.B. Freund, M. Sinclair, R.D. Twesten, and R.Q. Hwang, Phys. Rev. Lett., **80**, 4717 (1998)

[48] D.K. Fork, A. Barrera, T.H. Geballe, A.M. Viano, and D.B. Fenner, Appl. Phys. Lett. **57**, 2504 (1990)

[49] L.B. Freund, J.A. Floro, and E. Chason, Applied Physics Letters, **74**, 1987 (1999)

[50] P.N. Gadgil, J. Electron. Mater., **22**, 171 (1993)

[51] M.A. Gallivan, D.G. Goodwin, and R.M. Murray, "A Design Study for Thermal Control of a CVD Reactor for YBCO," in The Proceedings of the International Conference on Control Applications (1998)

[52] M.A. Gallivan and A. Iwaniec, *Calibration Oven Manual*, California Institute of Technology, Private Communication (2000)

[53] J.R. Gavaler, Appl. Phys. Lett., **23**, 480 (1973)

[54] J.I. Goldstein, D.E. Newbury, P. Echlin, and D.C. Joy, *Scanning Electron Microscopy and X-ray Microanalysis,* Plenum Press, New York (1992)

[55] G.S. Grader, P.K. Gallagher, J. Thomson, and M. Gurvitch, Appl. Phys. A, **45**, 179 (1988)

[56] P.R. Griffiths and J.A. de Haseth, *Fourier Transform Infrared Spectrometry*, John Wiley & Sons, New York (1986)

[57] A.I. Gurary, G.S. Tompa, A.G. Thompson, R.A. Stall, P.A. Zawadzki, and N.E. Schumaker, J. Crystal Growth, 145, 642 (1994)

[58] R.H. Hammond and R. Bormann, Physica C, **162**, 703 (1989)

[59] B. Han and Y. Guo, Experimental/Numerical Mechanics in Electronic Packaging, **1**, 1 (1996)

[60] K. Hanaoka, H. Ohnishi, H. Harima, and K. Tachibana, Physica C, **190**, 145 (1991)

[61] N. Hata, A. Matsuda, and K. Tanaka, J. Electrochem. Soc., 134, C485 (1987)

[62] R.M. Hazen, L.W. Finger, R.J. Angel, C.T. Prewitt, N.L. Ross, H.K. Mao, C.G. Hadidiacros, P.H. Hor, R.L. Meng, and C.W. Chu, Phys. Rev. B, **35**, 7238 (1987)

[63] M.L. Hitchman, S.H. Shamlian, G.G. Condorelli, and F. Chabert Rocabois, J. Alloy Compd., **251**, 297 (1997)

[64] M. Hong, S.H. Liou, J. Kwo, and B.A. Davidson, Appl. Phys. Lett., **51**, 694 (1987)

[65] R. Howland and L. Benatar, *A Practical Guide to Scanning Probe Microscopy*, Park Scientific Instruments, Sunnyvale, CA (1996)

[66] J. Hudner, O. Thomas, E. Mossang, P. Chaudouet, F. Weiss, D. Boursier, J.P. Senateur, M. Ostling, and A. Gaskov, J. App. Phys., **74**, 4931 (1993)

[67] J. Humlicek, J. Kirchner, H.-U. Habermeier, and M. Cardonna, Physica C, **190**, 383 (1992)

[68] Y. Ikuma, S. Akiyoshi, J. Appl. Phys., **64**, 3915 (1988)

[69] http://www.inorgtech.com/products/product0.html

[70] S. Jantsch, J. Ihringer, J.K. Maichle, W. Prandl, S. Kemmler-Sack, R. Kiemel, S. Losch, W. Schafer, M. Schlichenmaier, and A.W. Hewat, J. Less Common Met. **150**, 167 (1989)

[71] J.R. Jasperse, A. Kahn, J.N. Plendl, and S.S. Mitra, Phys. Rev., **146**, 526 (1966)

[72] K.F. Jensen, E.O. Einset, and D.I. Fotiadis, Annu. Rev. Fluid Mech., **23**, 197 (1991)

[73] J.D. Jorgensen, M.A. Beno, D.G. Hinks, L. Soderholm, K.J. Volin, R.L. Hitterman, J.D. Grace, I.K. Schuller, C.V. Serge, K. Zhang, and M.S. Kleefisch, Phys. Rev. B, **36**, 3608 (1987)

[74] J. Kawashima, Y. Yamada, and I. Hirabayashi, Physica C, **306**, 114 (1998)

[75] L.R. Raja, R.J. Kee, R. Serban, and L.R. Petzold, "Dynamic Optimization of Chemically Reacting Stagnation Flows," in 194th Electrochemical Society Proceedings (1998)

[76] J. Kircher, M.K. Kelly, S. Rashkeev, M. Alouani, D. Fuchs, M. Cardona, Phys. Rev. B, **44**, 217 (1991)

[77] K. Kishio, K. Suzuki, T. Yamamoto, K. Kitazawa, and K. Fueki, J. Solid State Chem., **82**, 192 (199)

[78] S. Kittelberger, O.M. Stoll, and R.P. Huebener, Supercond. Sci. Technol., **11**, 744 (1998)

[79] S. Kittelberger, U. Bolz, R.P. Heubener, B. Holzapfel, and L. Mex, Physica C, **302**, 93 (1998)

[80] S. Kittelberger, U. Bolz, R.P. Huebener, B. Holzapfel, L. Mex, and R.A. Schwarzer, Physica C, **312**, 7 (1999)

[81] N. Kobayashi, Y. Nakamura, H. Goto, and Y. Homma, J. Appl. Phys., 73, 4637 (1993)

[82] A.Y. Kovalgin, F. Chabert Rocabois, M.L. Hitchman, S.H. Shamlian, and S.E. Alexandrov, J. Phys. IV, **5:C5**, 357 (1995)

[83] C. Krauns and H. Krebs, Z. Phys. B, **92**, 43 (1993)

[84] J. Kwo, T.C. Hsieh, R.M. Fleming, M. Hong, S.H. Liou, B.A. Davidson, and L.C. Feldman, Phys. Rev. B, **36**, 4039 (1987)

[85] W.K. Kwok, G.B. Crabtree, A. Umezawa, B.W. Veal, J.D. Jorgensen, S.K. Malik, L.J. Nowicki, A.P. Paulikas, and L. Nunez, Phys. Rev. B, **37**, 106 (1988)

[86] J.R. Lagraff and D.A. Payne, Phys. Rev. B, **47**, 3380 (1993)

[87] R.B. Laibowitz, R.H. Koch, P. Chaudhari, and R.J. Gambino, Phys. Rev. B, **35**, 8821 (1987)

[88] H. Ledbetter and L. Ming, J. Mater. Res., **6**, 2253 (1991)

[89] H. Lee, A.J. Rosakis, and L.B. Freund, *Full Field Optical Measurement of Curvatures in Ultrathin Film Substrate Systems*, To Be Published

[90] S.H. Lee, S.C. Bae, J.K. Ku, and H.J. Shin, Phys. Rev. B, **46**, 9142 (1992)

[91] M. Leskela, H. Molsa, and L. Niinisto, Supercond. Sci. Technol., **6**, 627 (1993)

[92] Y.Q. Li, J. Zhao, C.S. Chern, P. Lu, B. Gallois, P. Norris, and B. Kear, Physica C, **195**, 161 (1992)

[93] Y. Li, J.A. Kilner, T.J. Tate, M.J. Lee, R.J. Chater, H. Fox, R.A. de Souza, and P.G. Quincy, Phys. Rev. B, **51**, 8498 (1995)

[94] D.R. Lide, ed., *CRC Handbook of Chemistry and Physics, 77th edition*, CRC Press, Boca Raton (1996)

[95] J.G. Liebeskind, R.K. Hanson, and M.A. Cappelli, Appl. Optics, 32, 6117 (1993)

[96] Q.Y. Ma, E.S. Yang, G.V. Treyz, and C.A. Chang, Appl. Phys. Lett., **55**, 896 (1989)

[97] Q.Y. Ma, E.S. Yang, R.B. Laibowitz, and C.A. Chang, J. Electronic Materials, **21**, 487 (1991)

[98] Q.Y. Ma, P. Dosanjh, J.F. Carolan, and W.N. Hardy, Appl. Phys. Lett., **63**, 3633 (1993)

[99] J. Maeda, Y. Nakamura, T. Izumi, and Y. Shiohara, Supercond Sci Tech, **12**, 563, (1999)

[100] V. Matijasevic, P. Rosenthal, K. Shinohara, A.F. Marshall, R.H. Hammond, and M.R. Beaslet, J. Mater. Res. **16**, 698 (1991)

[101] J. McManus, D. Fray, and J. Evetts, Physica C, **169**, 193 (1990)

[102] A. Mogro-Campero, L.G. Turner, E.L. Hall, M.F. Garbuaskas, and N. Lewis, Appl. Phys. Lett., **54**, 2719 (1989)

[103] A. Mogro-Campero, Supercond. Sci. Technol., **3**, 155 (1990)

[104] P.W. Morrison, J.R. Haigis, J. Vacuum Sci. Tech. A, 11, 490 (1993)

[105] J. Musolf and E. Smith, IEEE T. Appl. Supercon. **9,** 2167 (1999)

[106] H. Nakajima, S. Yamaguchi, K. Iwasaki, H. Morita, H. Fujimori, and Y. Fujino, Appl. Phys. Lett., **53**, 1437 (1988)

[107] W.K. Chu, J.W. Mayer, and M.A. Nicolet, *Backscattering Spectrometry*, Academic Press Inc., Orlando (1978)

[108] W. D. Nix, Metall. Trans., **20A**, 2217 (1989)

[109] H. K. Onnes, Commun. Phys. Lab. Univ. Leiden, **120b**, 3 (1911)

[110] E.J.M. O'Sullivan and B.P. Chang, Appl. Phys. Lett., **52**, 1441 (1988)

[111] D.J. Otway, B. Obi, and W.S. Rees, J. Alloys and Compounds, **251**, 254 (1997)

[112] S.I. Park, C.C. Tsuei, and K.N. Tu, Phys. Rev. B, **37**, 2305 (1988)

[113] M.V. Patrakeev, I.A. Leonidov, V.L. Kozhevnikov, V.I. Tsidilkovskii, and A.K. Demin, Physica C, **210**, 213 (1993)

[114] C. Pickering, Thin Solid Films, 313, 406 (1998)

[115] O. Porat, Z. Rosenstock, I. Schtreichman, and I. Riess, Solid State Ionics, **86-88**, 1385 (1996)

[116] H.F. Poulsen, N.H. Andersen, and B. Lebech, Physica C, **173**, 387 (1991)

[117] S. Proyer, E. Stangl, M. Borz, B. Hellebrand, and D. Bauerle, Physica C, **257**, 1, (1996)

[118] L.R. Raja, Colorado School of Mines, Private Communication (2000)

[119] S.J.B. Reed, *Electron Microprobe Analysis*, Cambridgy University Press, Cambridge (1975)

[120] Y.J. Lee, J. Lambros, and A.J. Rosakis, Optics and Lasers in Engineering, **25**, 25 (1996)

[121] A.J. Rosakis, R.P. Singh, Y. Tsuji, E. Kolawa, and N.R. Moore Jr., Thin Solid Films, **325**, 42 (1998)

[122] S.J. Rothman, J.L. Routbort, and J.E. Baker, Phys. Rev. B, 40, 8852 (1989)

[123] S.J. Rothman, J.L. Routbort, U. Welp, and J.E. Baker, Phys. Rev. B, **44**, 2326 (1991)

[124] J.C. Russ, *Fundamentals of Energy Dispersive X-ray Analysis*, Butterworths, London (1984)

[125] J. Saulitis, G.R. Johnston, and J.L. Cocking, Thin Solid Films, **166**, 201 (1988)

[126] D. Schafer, B. Brauns, R. Wolf, B. STeiger, and G. Zscherpe, Vacuum, 41, 1084 (1990)

[127] M. Scheuermann, C.C. Chi, C.C. Tsuei, D.S. Yee, J.J. Cuomo, R.B. Laibowitz, R.H. Koch, B. Braren, R. Srinivasan, and M.M. Plechaty, Appl. Phys. Lett., **51**, 1951 (1987)

[128] Y. Scolnik, E. Sabatani, and D. Cahen, Physica C, **174**, 273 (1991)

[129] J. Shanker, S.S. Kushwah, and P. Kumar, Physica B, **78**, 223 (1997)

[130] P. Shewmon, *Diffusion in Solids*, The Minerals, Metals, & Materials Society Press, Pennsylvania (1989)

[131] L.T. Shi and K.N. Tu, Appl. Phys. Lett., **55**, 1351 (1989)

[132] G. Simmons and H. Wang, *Single Crystal Elastic Constants and Calculated Aggregate Properties: A Handbook*, MIT Press, Cambridge (1971)

[133] V.A. Skryshevsky, P. Kus, V.I. Strikha, T.A. Vdovenkova, and K. Karlovsky, Supercond. Sci. Technol., **7**, 651 (1994)

[134] E. Span, H. Wormeester, D. Blank, and H. Rogalla, Materials Science and Engineering, B**56**, 123 (1998)

[135] M. Stenger, G. Ockenfub, M. Reese, T. Konigs, R. Wordenweber, C. Barre, J.Y. Prieur, and J. Joffrin, Solid State Comm., **98**, 777 (1996)

[136] G. G. Stoney, Proc. Roy. Soc. (London) **A82**, 172 (1909).

[137] G.H. Stout and L.H. Jensen, *X-Ray Structure Determination*, John Wiley & Sons, New York (1989)

[138] Y. Sumino, O.L. Anderson, and I. Suzuki, Phys. Chem. Minerals, **9**, 38 (1983)

[139] T.B. Tang and W. Lo, Physica C, **174**, 463 (1991)

[140] L.R. Testardi, J.H. Wernick, and W.A. Royer, Solid State Commun., **15**, 1 (1974)

[141] A.G. Thompson, R. Karlicek, E. ARmour, W. Kroll, P. Zawadzki, and R.A. Stall, III-V Review, 9, 12 (1995)

[142] A.G. Thompson, R.A. Stall, P. Zawadzki, and G.H. Evans, J. Electron. Mater., 25, 1487 (1996)

[143] A.G. Thompson, Mater. Lett., 30, 255 (1997)

[144] P. Tobaly and G. Lanchec, J. Chem. Thermodyn., **25**, 503 (1993)

[145] P. Tobaly and I.M. Watson, J. Chem. Thermodyn., **27**,1211 (1995)

[146] G.S. Tompa, P.A. Zawadzki, K. Moy, M. McKee, A.G. Thompson, A.I. Gurary, E. Wolak, P. Ersherick, W.G. Breiland, G.H. Evans, N. Bulitka, J. Hennessy, and C.J.L. Moore, J. Crystal Growth, 145, 655 (1994)

[147] Y. Toyoshima, Thin Solid Films, 234, 367 (1993)

[148] A.B. Tripathi, D.A. Boyd, M.A. Gallivan, R.M. Murray, H.A. Atwater, D.G. Goodwin, L.R. Raja, R.J. Kee, and J. Musolf, "A Stagnation-Flow MOCVD Reactor For Intelligent Deposition of YBCO Thin Films," in Proceedings of the Electrochemical Society Spring Meeting (2000)

[149] A.E. Turgambaeva, A.F. Bykov, and I.K. Igumenov, J. Phys. (Paris) IV, Colloq., **5**, C5-221, (1995)

[150] A.E. Turgambaeva, A.F. Bykov, and I.K. Igumenov, Electrochemical Soc. Proc., **97-25**, 139

[151] S.B. Turnipseed, R.M. Barkley, and R.E. Sievers, J. Am. Chem. Soc., **30**, 1164 (1991)

[152] K.N. Tu, N.C. Yeh, S.I. Park, and C.C. Tsuei, Phys. Rev. B, **39**, 9142 (1989)

[153] T. Umemura, K. Egawa, M. Wakata, and K. Yoshizaki, Japan. J. Appl. Phys., **28**, L1945 (1989)

[154] T.A. Vanerah, R.S. Roth, and H.F. McMurdie, eds, *Phase Diagrams for High Tc Superconductors II,* American Ceramic Society, Ohio (1997)

[155] D.J. Vischjager, P.J. VanDerPut, J. Schram, and J. Schoonman, Solid State Ionics, **27**, 199 (1988)

[156] S.R. Vosen, Electrochemical Society Proceedings **96-5**, 95 (1996)

[157] T. Vreeland, A. Dommann, C.J. Tsai, and M.A. Nicolet, Mater. Res. Soc. Proc., **30**, 3 (1988)

[158] V.B. Vykhodets, T.E. Kurennykh, K.V. Trifonov, A.Y. Fishman, and A.A. Fotiev, JETP, **79**, 355 (1994)

[159] E. Waffenschmidt, G. Sjamsudin, J. Musolf, F. Arndt, X. He, M. Heuken, and K. Heime, J. Appl. Phys., **77**, 438 (1995)

[160] I.M. Watson, Chemical Vapor Deposition **3,** 9 (1997)

[161] I.M. Watson, M.P. Atwood, and S. Haq, Supercond. Sci. Technol., **7**, 672 (1994)

[162] I.M. Watson, M.P. Atwood, D.A. Cardwell, and T.J. Cumberbatch, J. Mater. Chem. **4**, 1393 (1994)

[163] I.M. Watson, *Handbook of Thin Film Technology*, IOP Publishing, Bristol (1995)

[164] C. Webb, S.L. Weng, J.N. Eckstein, N. Missert, K. Char, D.G. Schlom, E.S. Hellman, M.R. Beasley, A. Kapitulnik, and J.S. Harris Jr., Appl. Phys. Lett., **51**, 1191 (1987)

[165] F.M. White, *Heat and Mass Transfer,* Addison-Wesley, Massachusetts (1988)

[166] F.M. White, *Viscous Fluid Flow,* McGraw-Hill, New York (1991)

[167] M.K. Wu, J.R. Ashburn, C.J. Torng, P.H. Hor, R.L. Meng, L. Gao, Z.J. Huang, Y.Q. Wang, and C.W. Chu, Phys. Rev. Lett., **58**, 908 (1987)

[168] W. Wu, M.T. Lanagan, M.L. Jullberg, R.B. Poeppel, B. Wang, and S. Danyluk, Thin Solid Films, **223**, 260 (1993)

[169] K. Yamamoto, B.M. Lairson, J.C. Bravman, and T.H. Geballe, J. Appl. Phys., **69**, 7189 (1991)

[170] A. Yoshida, H. Tamura, S. Morohashi, and S. Hasuo, Appl. Phys. Lett., **53**, 811 (1988)

[171] J. Zhao, C.S. Chern, Y.Q. Li, D.W. Noh, P.E. Norris, P. Zawadzki, B. Kear, and B. Gallois, J. Crystal Growth, **107**, 699 (1991)

Appendix A Commonly Used Abbreviations

CGS	Coherent Gradient Sensing - measurement technique to study sample curvature and stress
CVD	Chemical Vapor Deposition - thin film growth technology
MOCVD	Metal Organic Chemical Vapor Deposition
YBCO, $YBa_2Cu_3O_7$	Yttrium-Barium-Copper-Oxide superconductor
XRD	X-Ray Diffraction - crystallographic measurement technique
RBS	Rutherford Backscattering Spectrometry - analytic technique to determine composition and thickness
AFM	Atomic Force Microscopy - analytic technique to determine surface profile
EDX	Energy Dispersive X-ray analysis - analytic technique to determine composition
FTIR	Fourier Transform InfraRed spectrometry - analytic technique to determine spectral features
RHEED	Reflective High Energy Electron Diffraction
SLM	Standard Liters per Minute - mass flowrate of fluid
tmhd	tetramethylheptanedionate - ligand from metalorganic precursors

Appendix B The Showerhead Oven

The showerhead oven is constructed of 0.030 thick stainless steel sheet metal with welded seams, ceramic wool insulation, and ceramic stand-offs to connect the inner box with the outer box. The inner box is depicted in Figure B.1, while the outer box is shown in Figure B.2.

Design of the showerhead oven involved a typical thermal resistance calculation to determine the heater power required; see Figure B.3. In this calculation, temperature is analogous to voltage, and heat transfer per unit area, $q"$, is analogous to electrical current. Thus for the first resistance,

$$q" = k\frac{(T_1 - T_2)}{x} \; , \tag{B.1}$$

where k is the thermal conductivity of our insulation ($k = .0721\frac{\mathrm{W}}{\mathrm{m\,K}}$) and $x = 2$ in, substitution yields

$$q" = 1.419\frac{\mathrm{W}}{\mathrm{m^2\,K}}(T_1 - T_2) \; . \tag{B.2}$$

For the second resistance

$$q" = h(T_2 - T_a) \; . \tag{B.3}$$

From [165], page 396, we can compute the heat transferred across the second resistance (natural convection on a vertical plate) using the following formula:

$$\frac{\mathrm{Nu}}{\mathrm{Gr}^{1/4}} = \frac{\mathrm{Pr}^{1/2}}{\left(2.435 + 4.884\,\mathrm{Pr}^{1/2} + 4.953\,\mathrm{Pr}\right)^{1/4}} \,. \tag{B.4}$$

Where the Nusselt number is as defined in the first part of equation 2.2, except D is substituted for by L in this case ($L = 16\,\mathrm{in} = .4064\,\mathrm{m}$), the Grashof number is defined as

$$\mathrm{Gr} = \frac{g\beta}{\nu^2}\left(T_2 - T_a\right)L^3 \,, \tag{B.5}$$

in which g is the acceleration due to gravity and β is the coefficient of thermal expansion, both of which are constants. In fact, for air we can reduce the Grashof number to

$$\mathrm{Gr} = 3.3 * 10^7 \frac{1}{\mathrm{K\,m}^3}\left(T_2 - T_a\right)L^3 \,. \tag{B.6}$$

Lastly, the Prandtl number is defined by

$$\mathrm{Pr} = \frac{\mu C_p}{k} = 0.71 \text{ for air at room temperature.} \tag{B.7}$$

Using these data, equation B.4 reduces to

$$\frac{\mathrm{Nu}}{\mathrm{Gr}^{1/4}} = 0.47305 \tag{B.8}$$

and with $k = 0.0328 \frac{\mathrm{W}}{\mathrm{m\,K}}$ for air at 135 °C, we find

$$h = 1.473 \frac{\mathrm{W}}{\mathrm{m}^2\,\mathrm{K}^{5/4}}\left(T_2 - T_a\right)^{1/4} \,. \tag{B.9}$$

Because the same current must pass through both resistors, we know that

$$q" = k\frac{(T_1 - T_2)}{x} = h(T_2 - T_a) \ . \tag{B.10}$$

Adding in the results for h, k, and the thermal boundary conditions, $T_1 = 250\,^{\circ}\mathrm{C}$ and $T_a = 25\,^{\circ}\mathrm{C}$, yields

$$T_2 = 83.2\,^{\circ}\mathrm{C} \ . \tag{B.11}$$

Although an external temperature of 83.2°C is too hot to touch, it is well within the acceptable range for stainless steel.

Lastly, we need to compute the power required to drive the internal heater:

$$q" = k\frac{(T_1 - T_2)}{x} = 236.71\frac{\mathrm{W}}{\mathrm{m}^2} \ . \tag{B.12}$$

For our oven design, we have a surface area of

$$Area = 4 * Side + Top = 1476\,\mathrm{in}^2 = .9523\,\mathrm{m}^2 \ , \tag{B.13}$$

which combines with $q"$ for a

$$Total\ Power = 225\,\mathrm{W} \ . \tag{B.14}$$

In order to provide for a factor of safety of $3x$, we selected a heater capable of outputting 650 Watts.

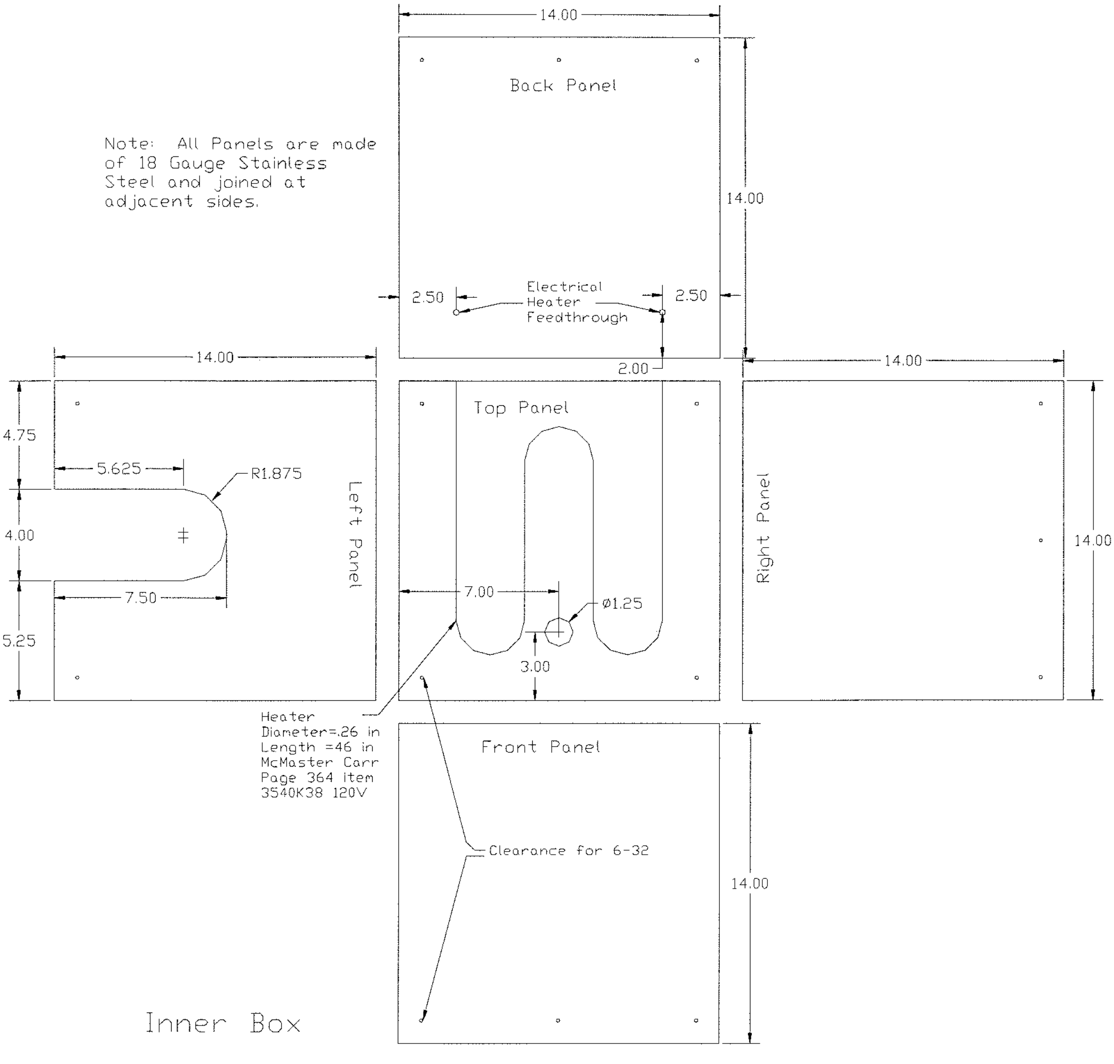

Figure B.1: Showerhead oven, internal box.

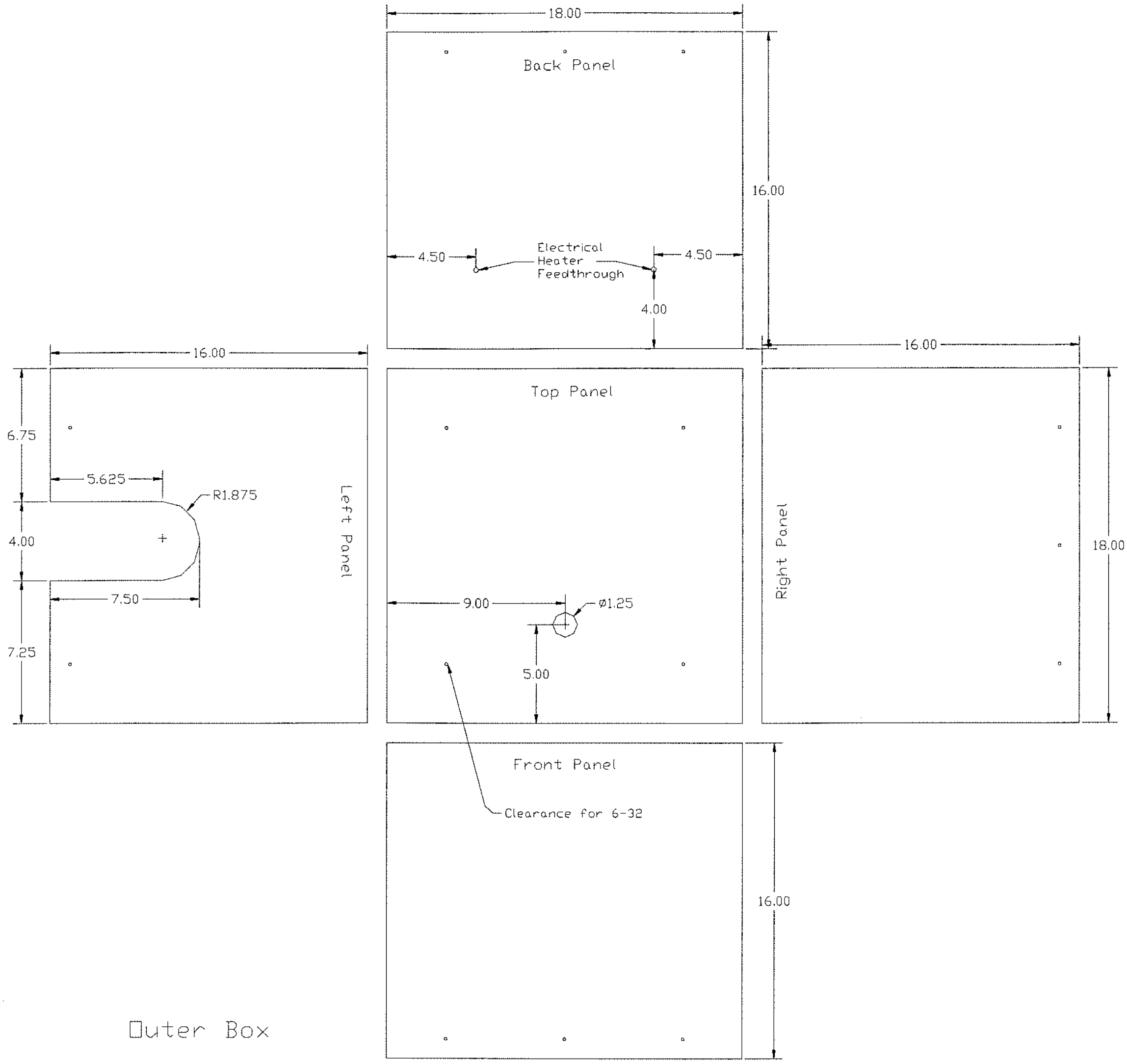

Figure B.2: Showerhead oven, external box.

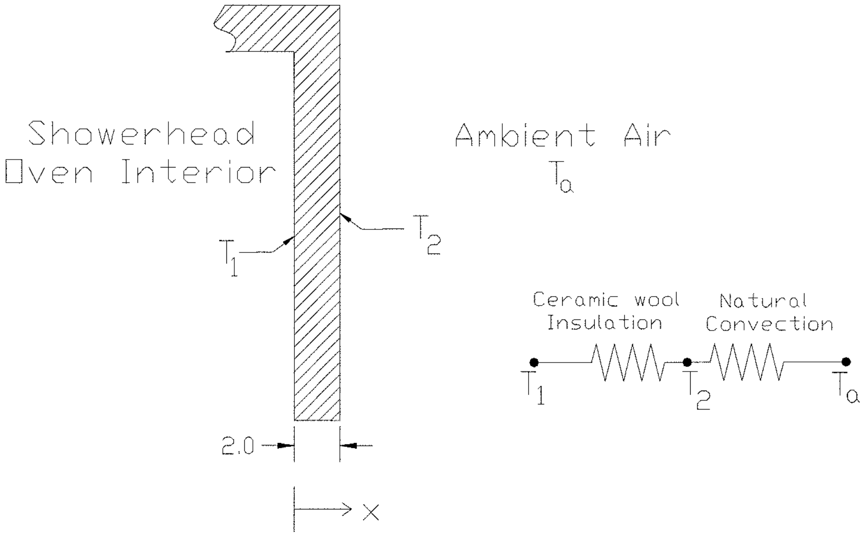

Figure B.3: Heat transfer through the showerhead oven can be modelled by a series of resistors.

Appendix C AutoCAD Drawings

The following figures are full page computer aided design (CAD) illustrations of the showerhead, Figures C.2 and C.3, and the reactor body, Figures C.4, C.5, C.6, and C.1.

In order to visually tie all of the cross-sections together, a top down view of the chamber body is presented in Figure C.1. It is worth noting that in this rendering of the chamber, the top flange (8 inch Conflat) is not present and neither are the coolant ports nor the bottom angled vacuum ports.

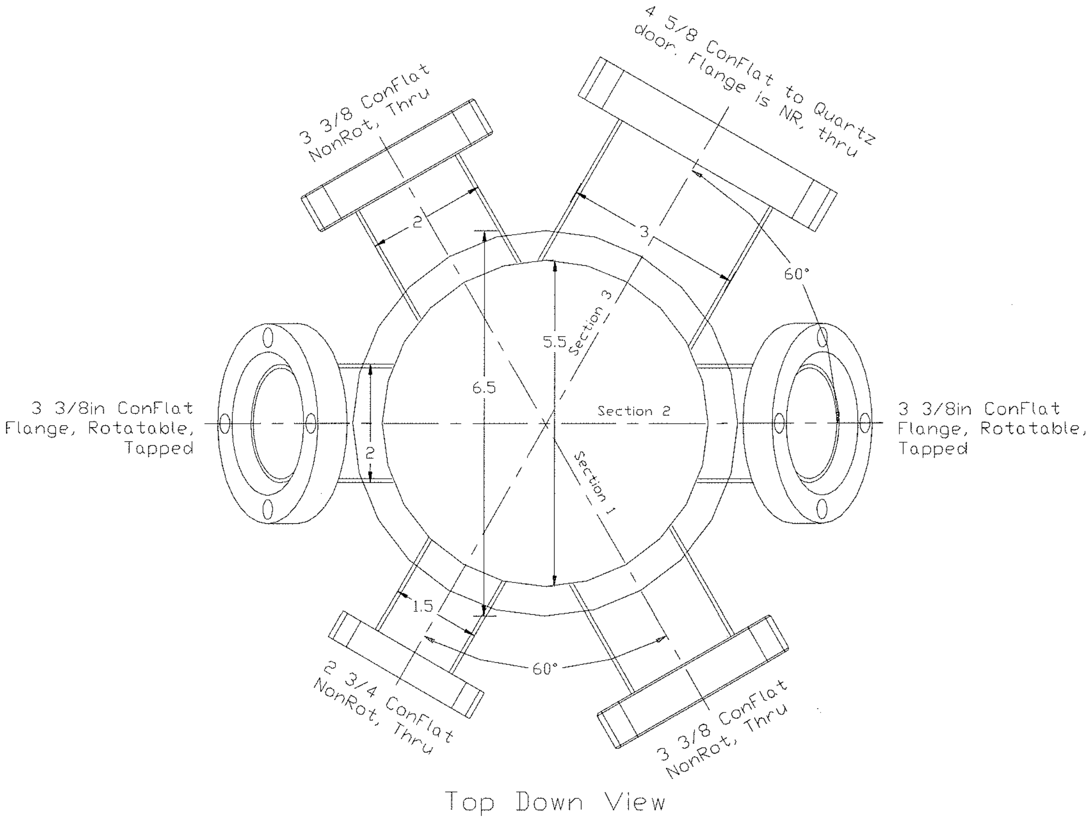

Figure C.1: AutoCAD illustration of the chamber body when viewed from above.

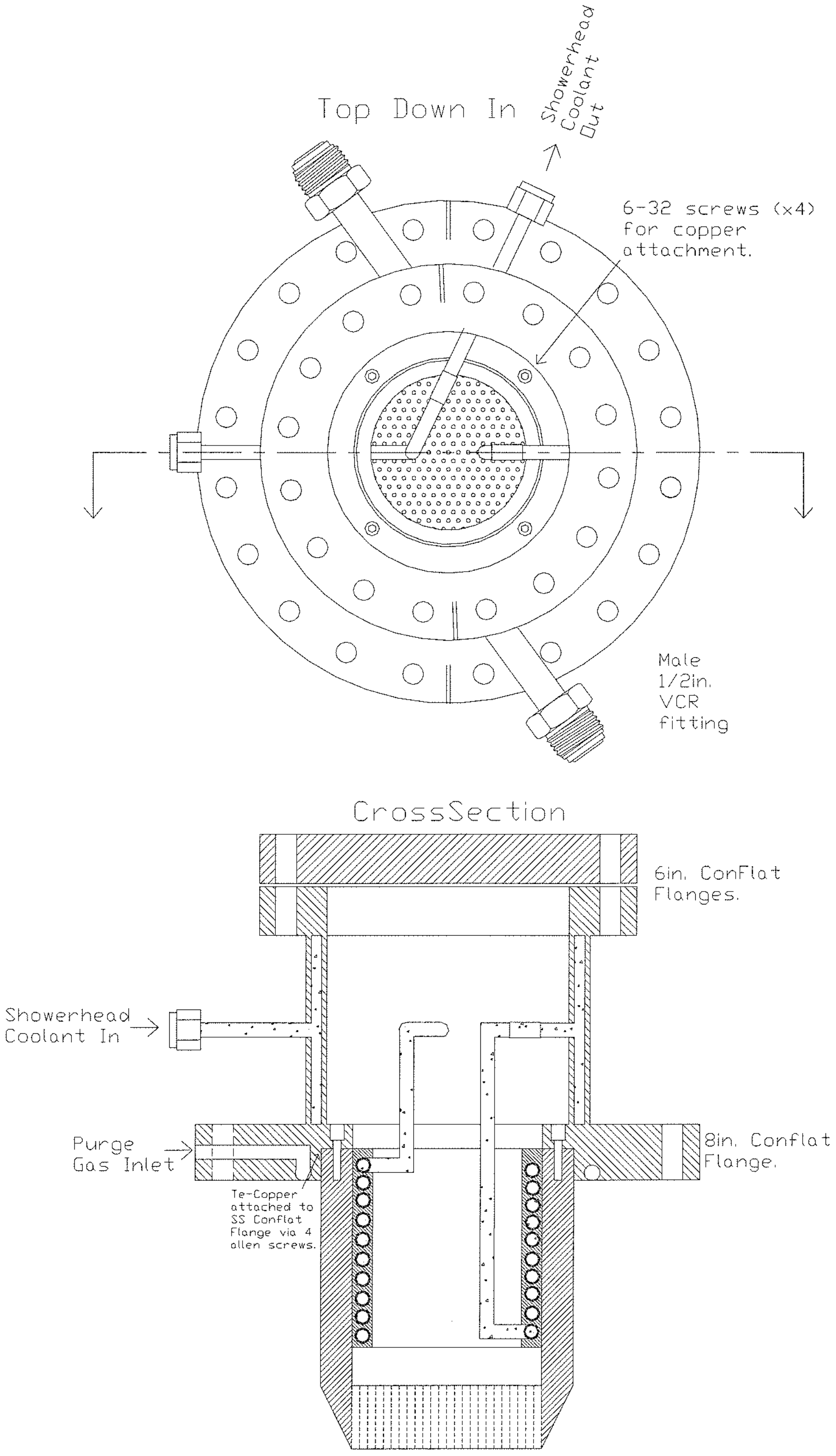

Figure C.2: Top down and cross-sectional views of the final showerhead design.

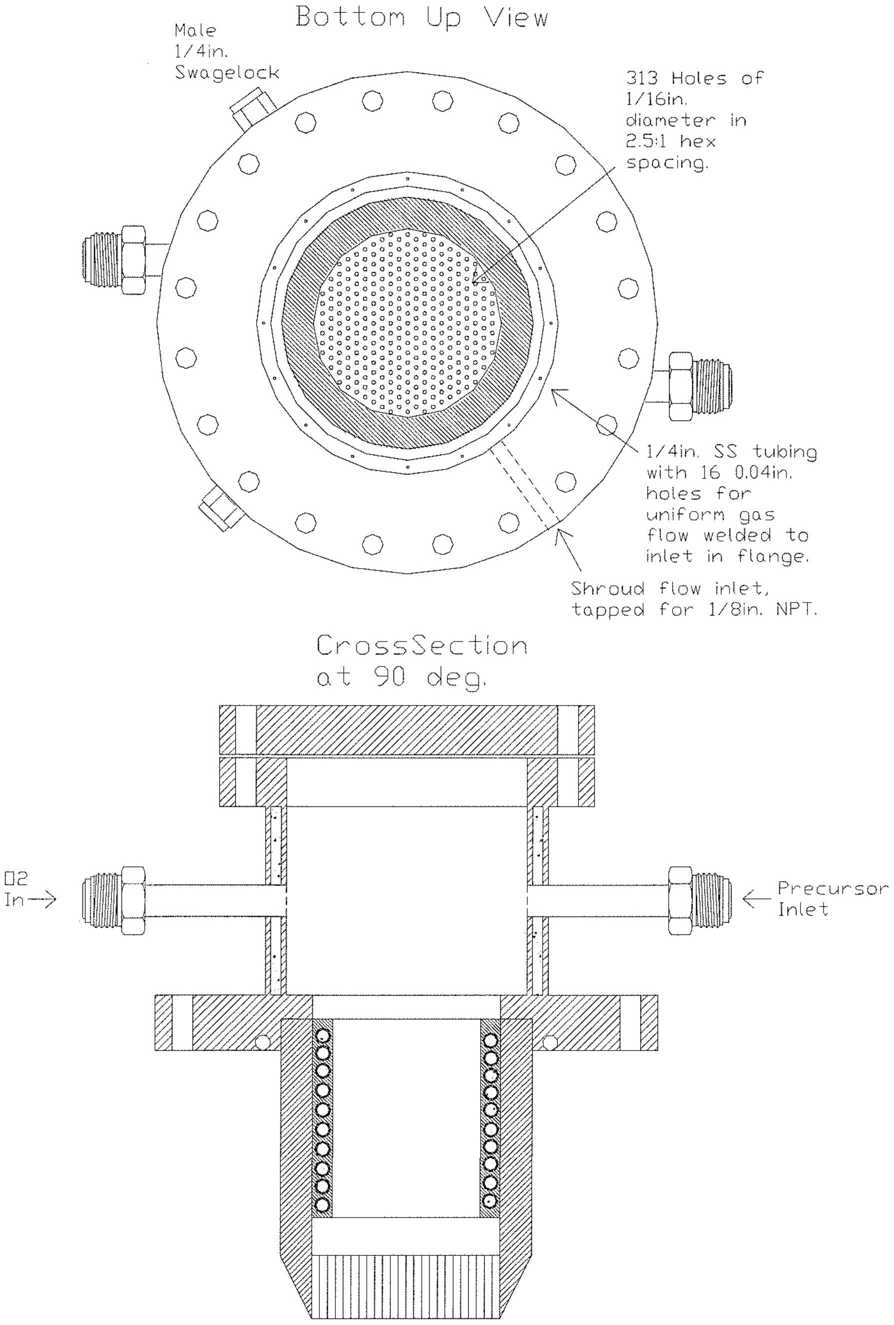

Figure C.3: Bottom up and 90° cross-sectional views of the showerhead final design.

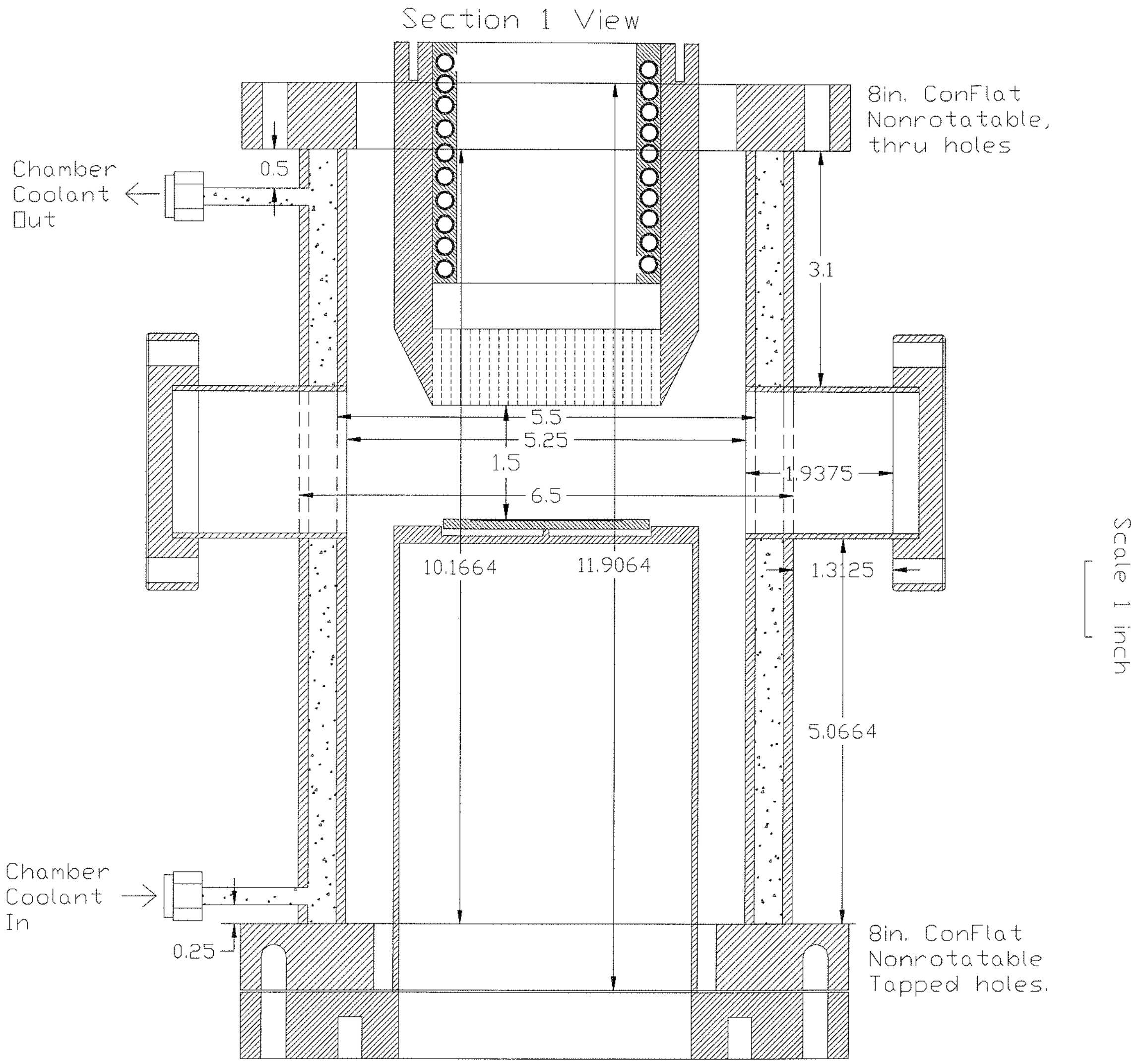

Figure C.4: Cross-sectional view through the straight-through viewports of the chamber body, inconel can, and copper portion of the showerhead.

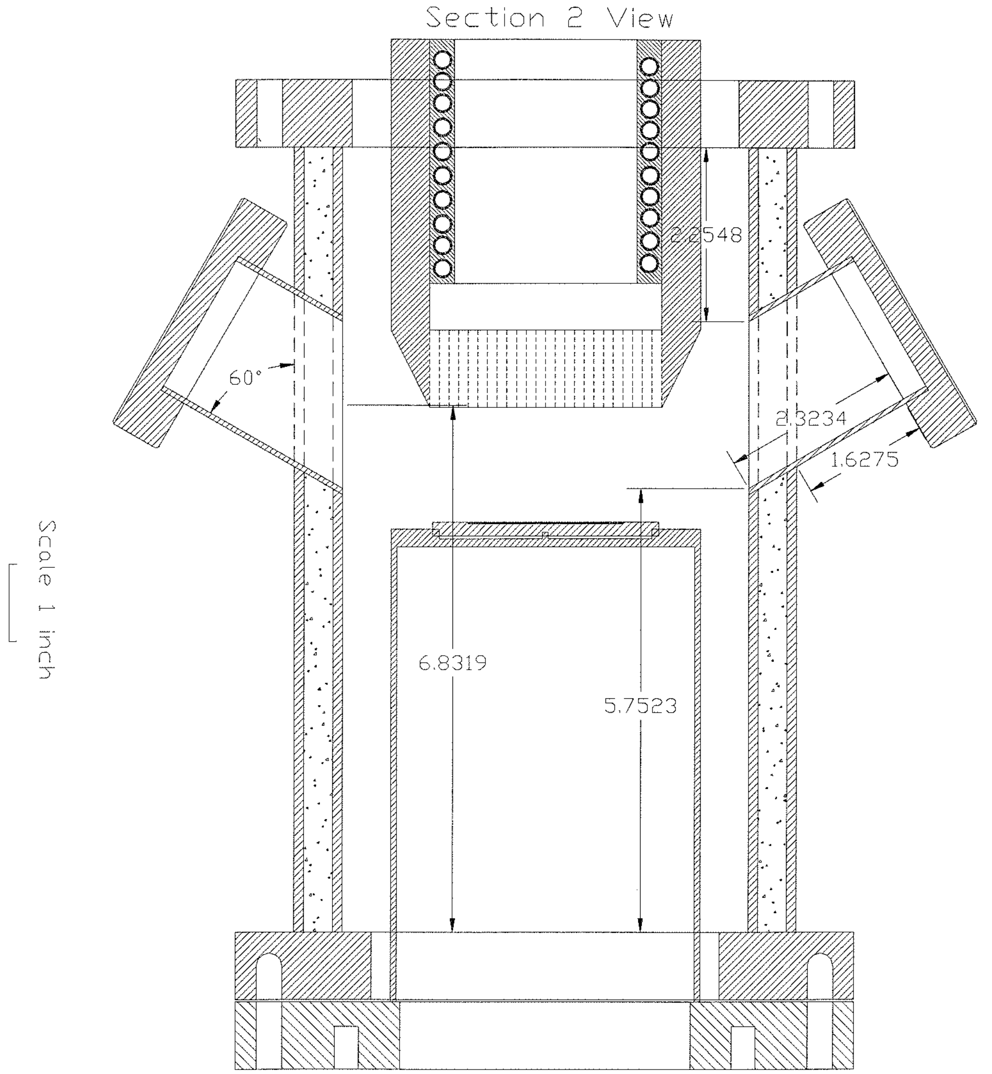

Figure C.5: Cross-sectional view through the angled viewports of the chamber body, inconel can, and copper portion of the showerhead.

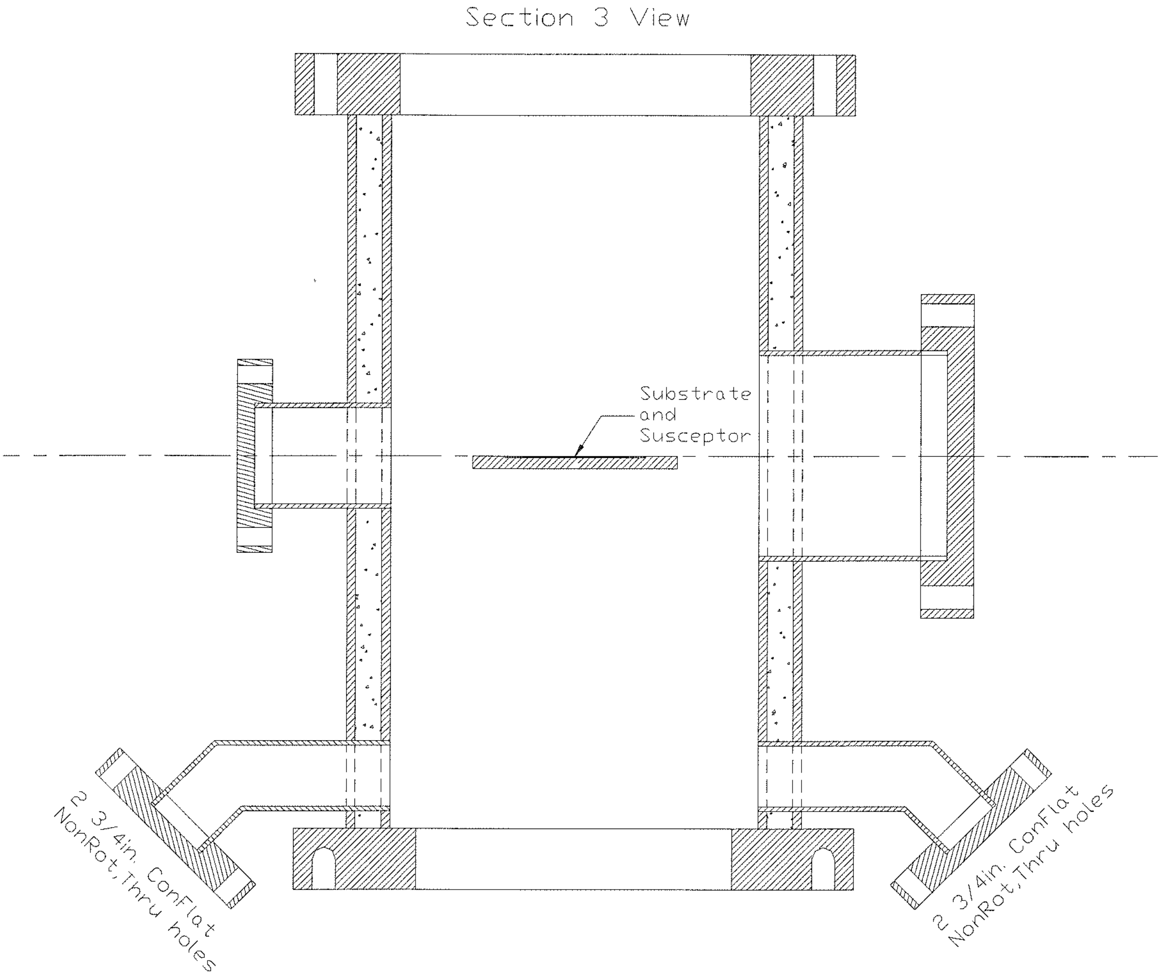

Figure C.6: Cross-section of chamber body illustrating the RHEED viewport and sample loading door. For clarity, both the showerhead and inconel can have been removed, although the substrate and susceptor remain.

Appendix D Raw Diffusion Data

D.1 YBCO Film Thickness = 500 nm

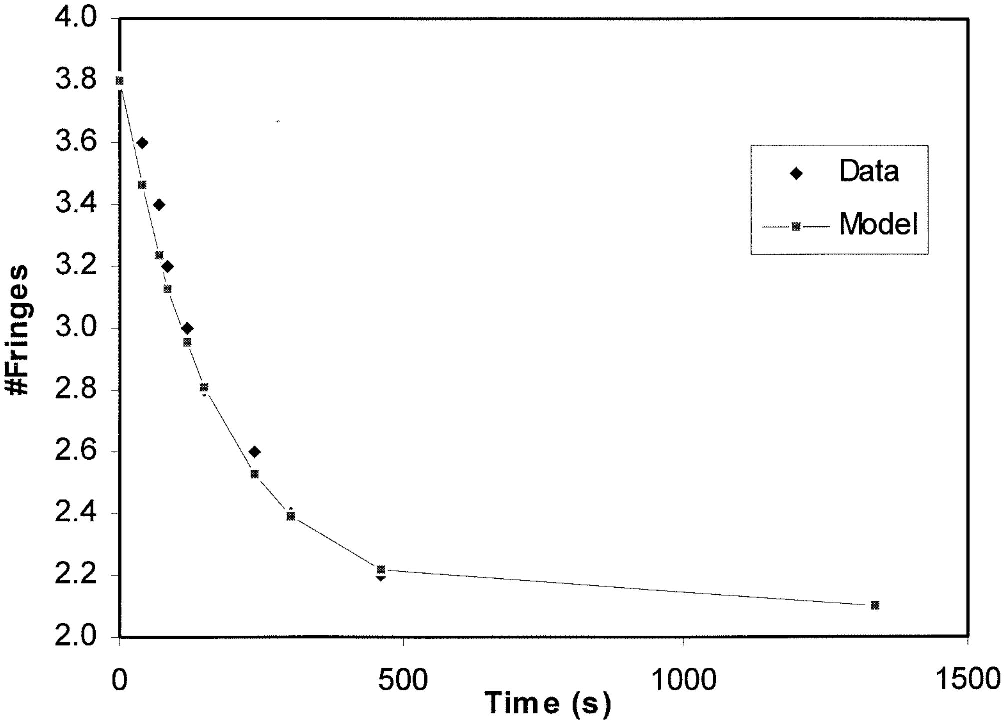

Figure D.1: Initial oxidation of 500nm film at 485°C.

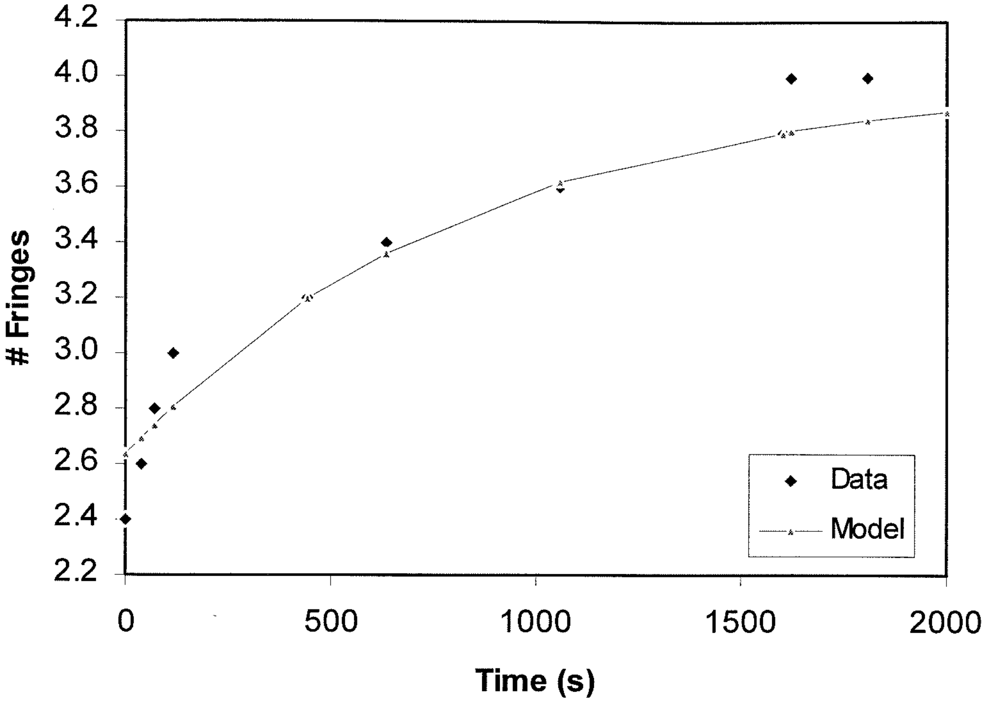

Figure D.2: Initial deoxidation of 500nm film at 485°C.

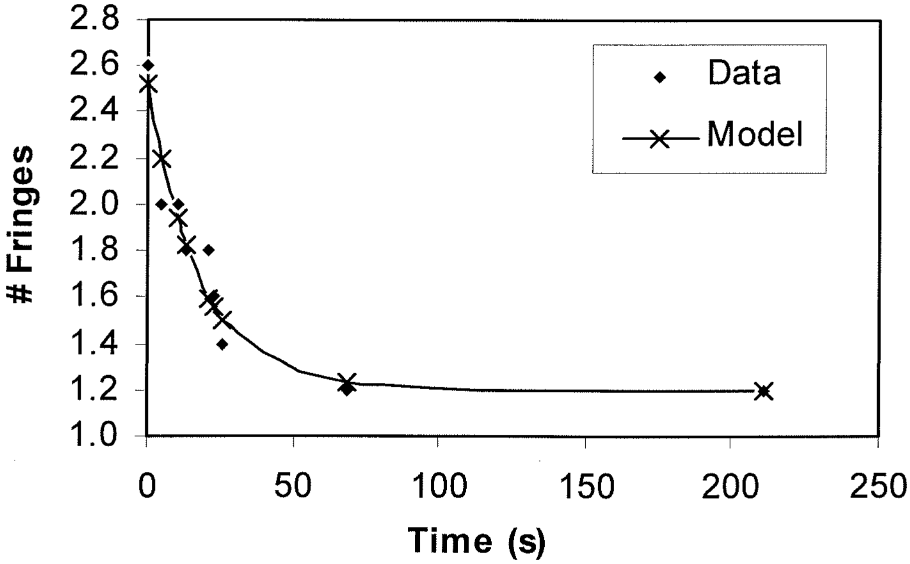

Figure D.3: Initial oxidation of 500nm film at 510°C.

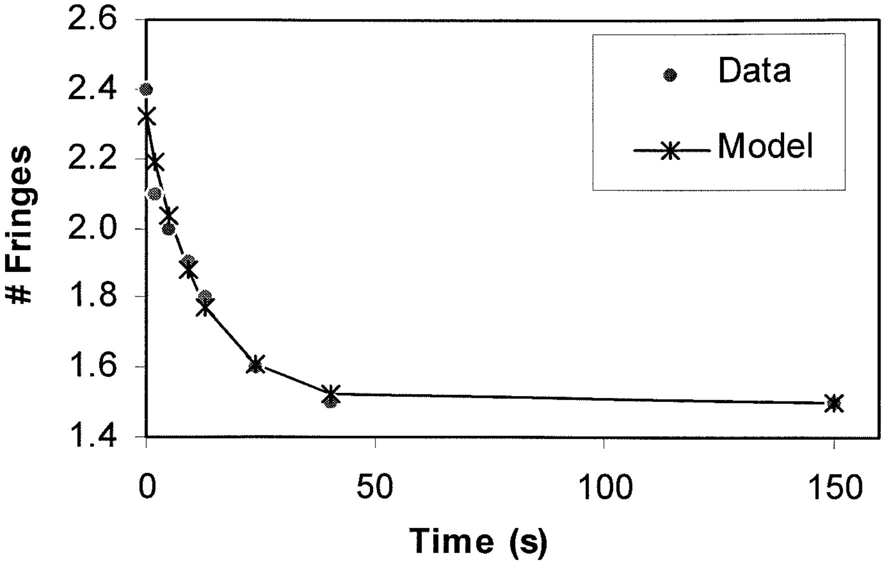

Figure D.4: Second oxidation of 500nm film at 510°C.

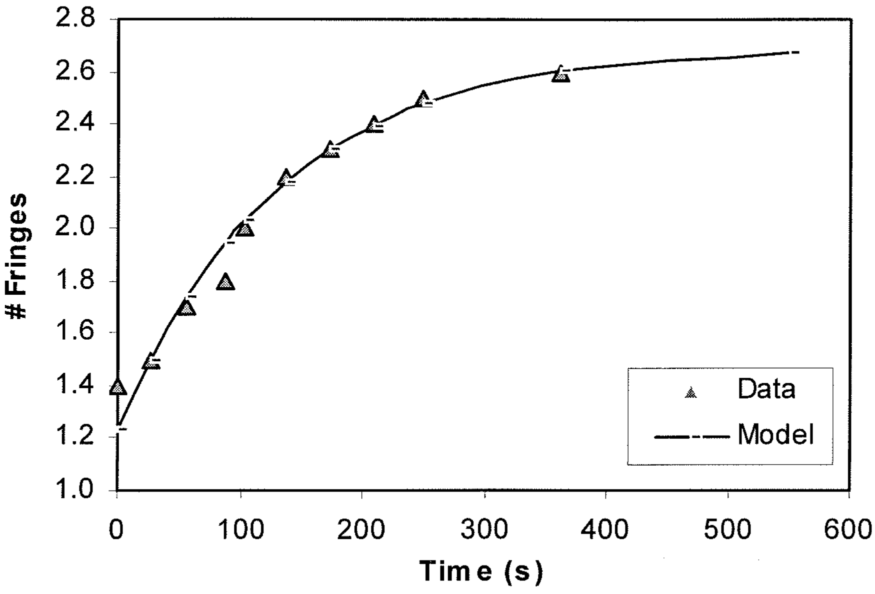

Figure D.5: Third oxidation of 500nm film at 510°C.

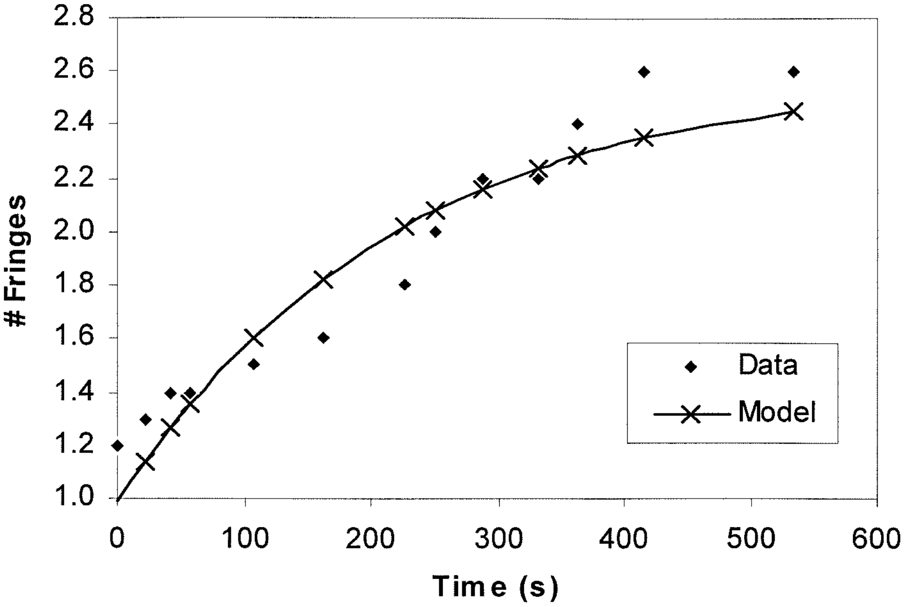

Figure D.6: Initial deoxidation of 500nm film at 510°C.

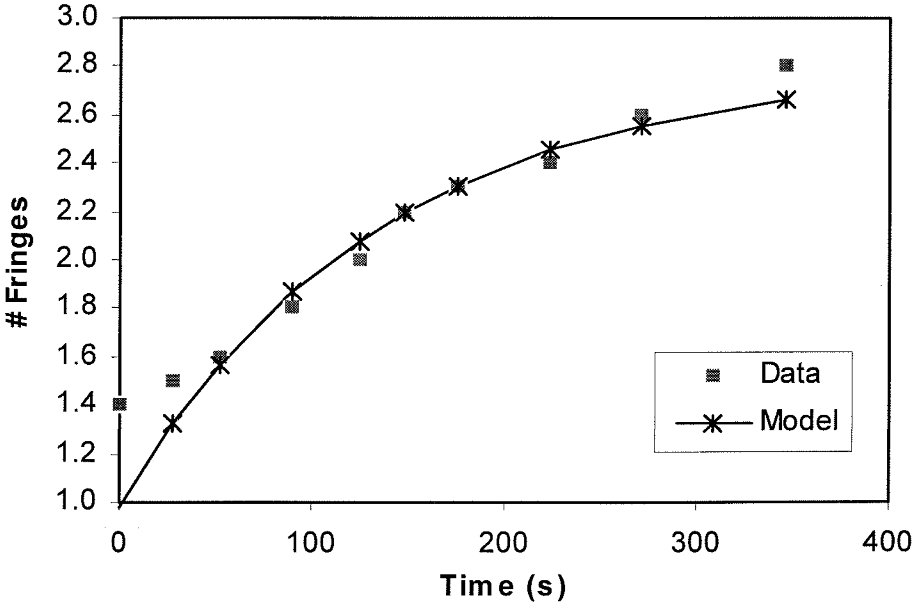

Figure D.7: Second deoxidation of 500nm film at 510°C.

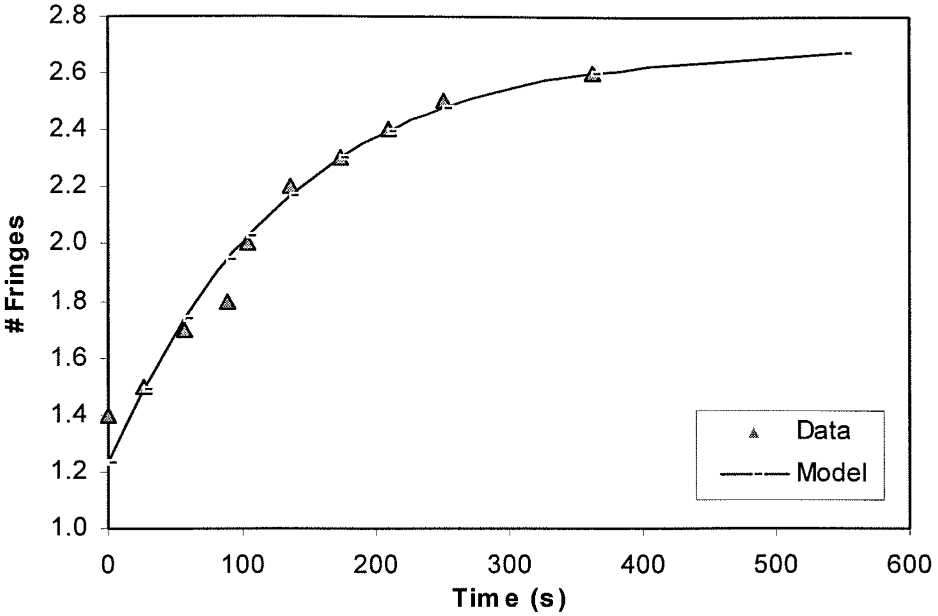

Figure D.8: Third deoxidation of 500nm film at 510°C.

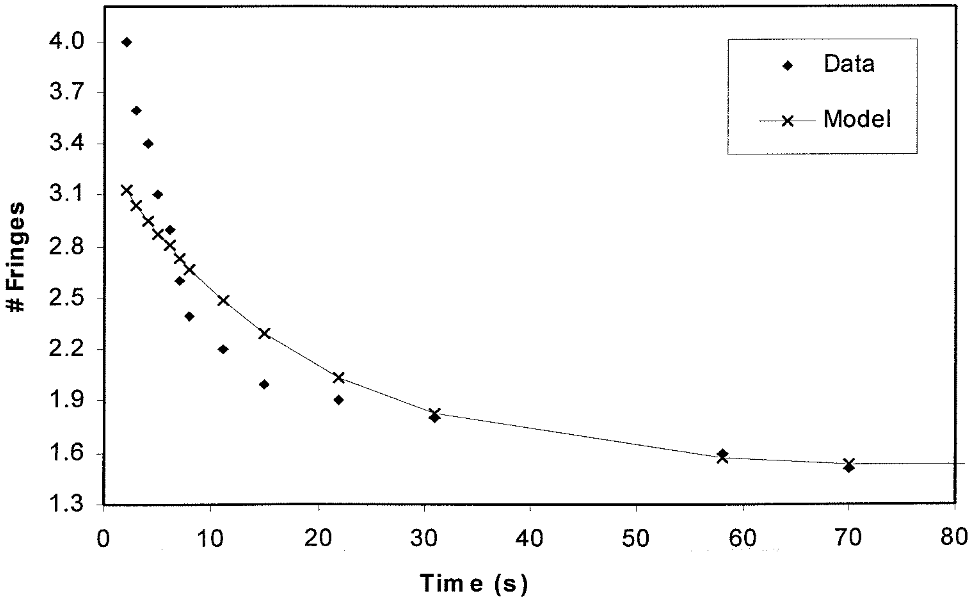

Figure D.9: Initial oxidation of 500nm film at 585°C. The poor exponential fit is due to a two component diffusion process, see Chapter 6.

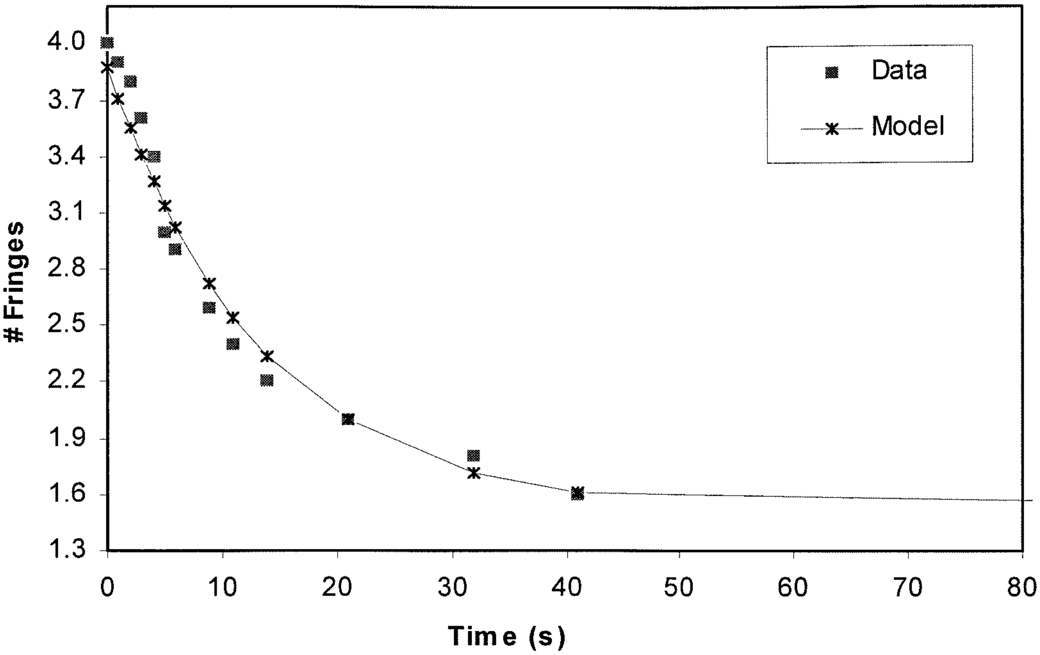

Figure D.10: Second oxidation of 500nm film at 585°C.

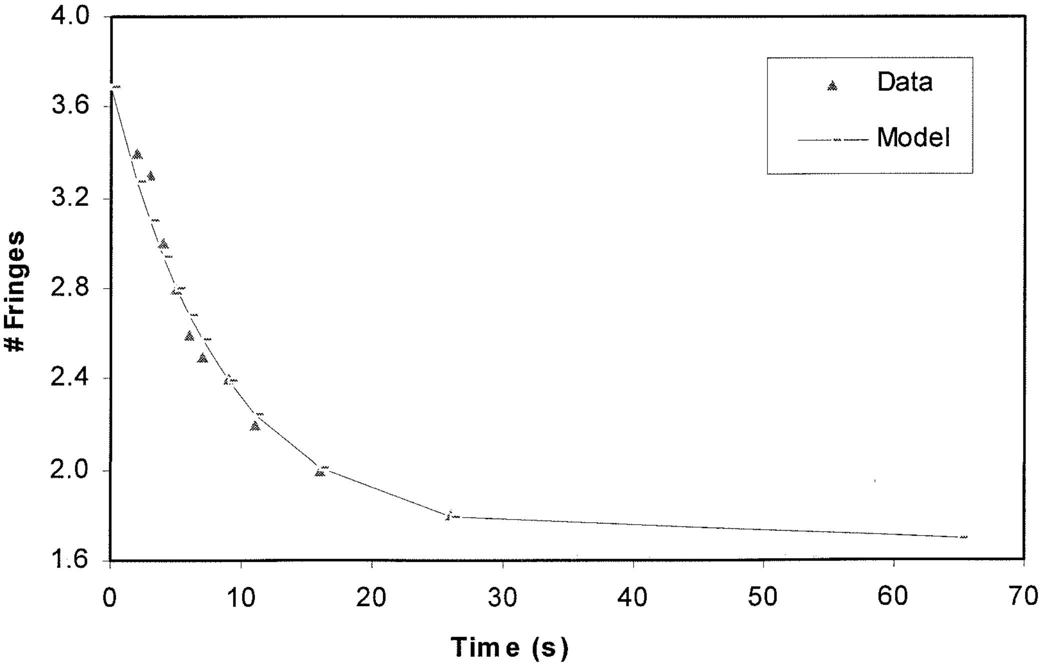

Figure D.11: Third oxidation of 500nm film at 585°C.

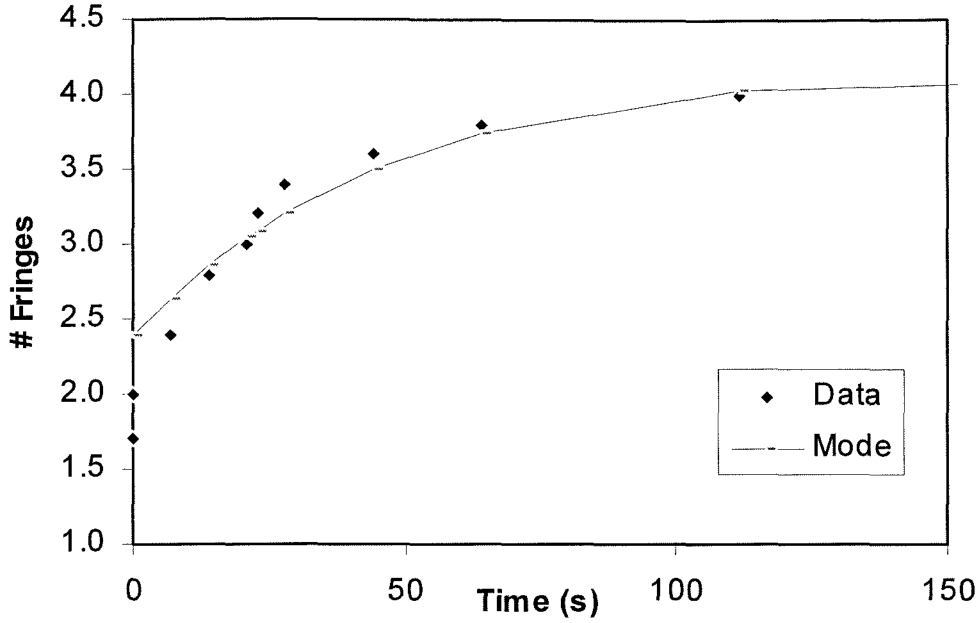

Figure D.12: Initial deoxidation of 500nm film at 585°C.

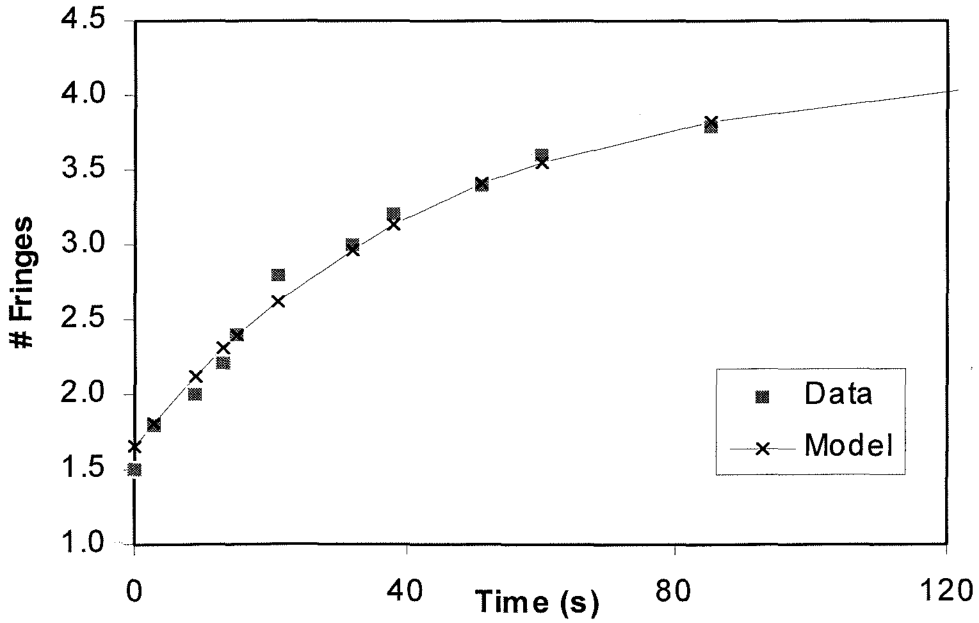

Figure D.13: Second deoxidation of 500nm film at 585°C.

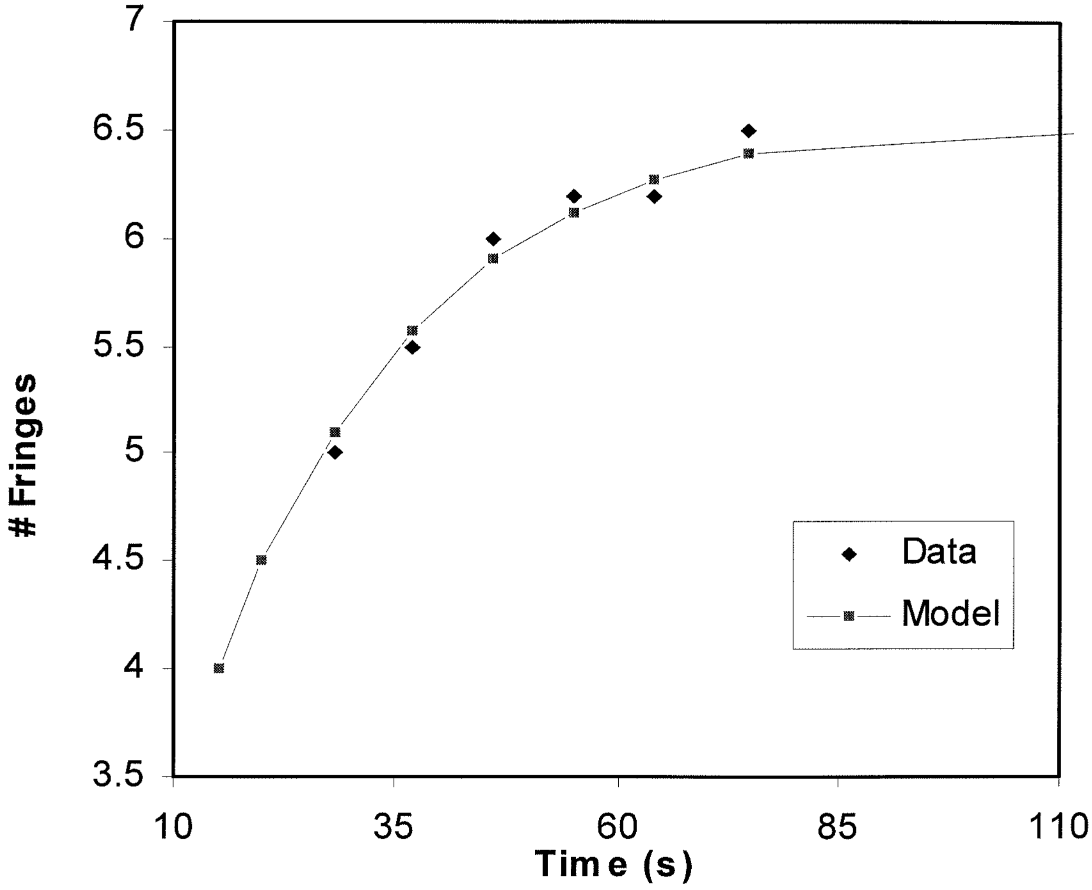

Figure D.14: Fourth deoxidation of 500nm film at 590°C.

D.2 YBCO Film Thickness = 700 nm

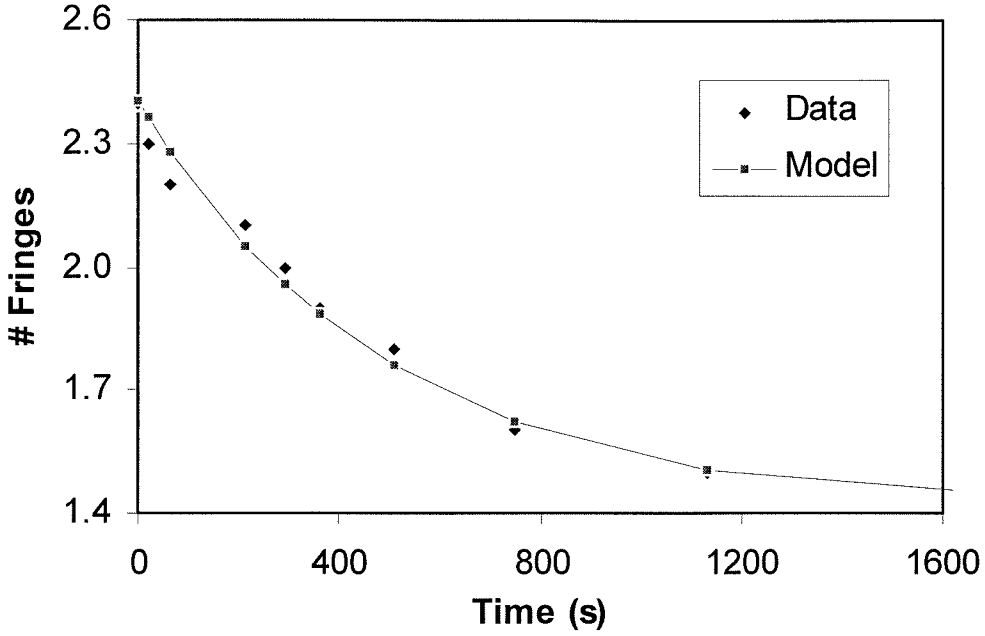

Figure D.15: Initial oxidation of 700nm film at 510°C.

Subsequent to the oxidation of the 700nm film at 510°C on November 17^{th}, 2000, we observed the CGS interferogram for 3000 seconds. The fringe count did not change within this time frame, so we concluded that the activation energy for out-diffusion of oxygen had not been reached, and we proceeded to heat the wafer to a temperature of 590°C. The intervening data at 585°C, was collected on October 16^{th}, 2000.

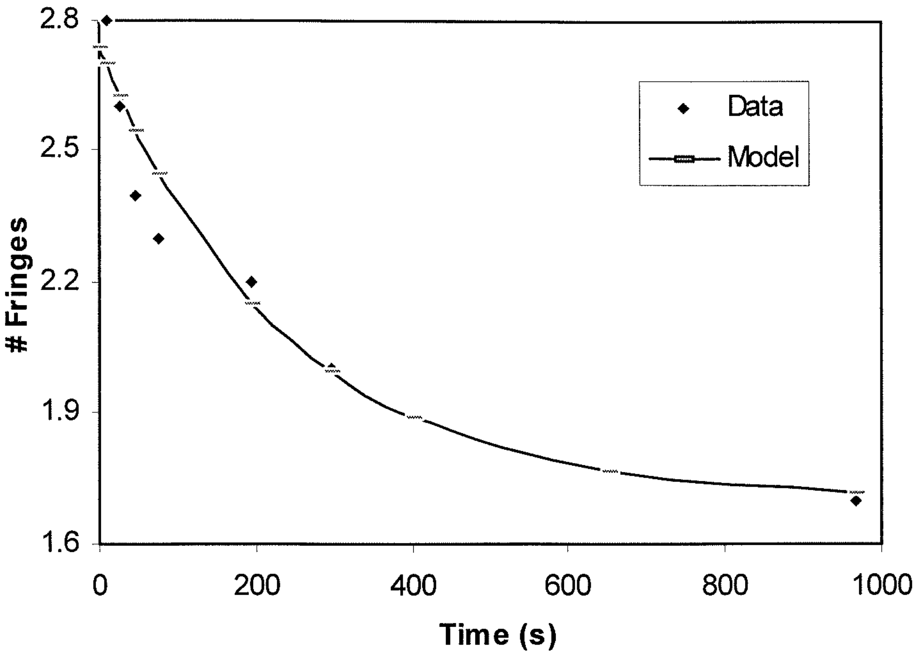

Figure D.16: Initial oxidation of 700nm film at 585°C.

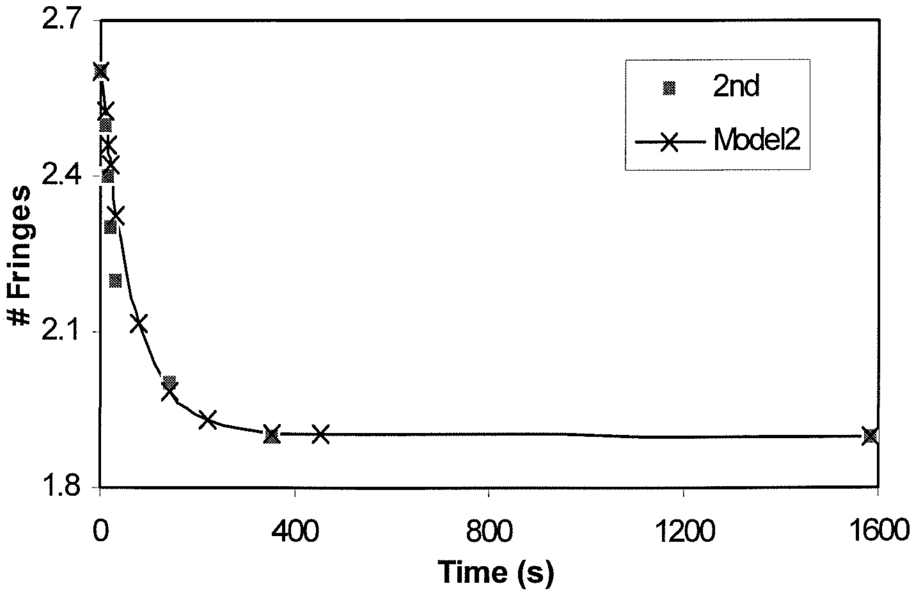

Figure D.17: Second oxidation of 700nm film at 585°C.

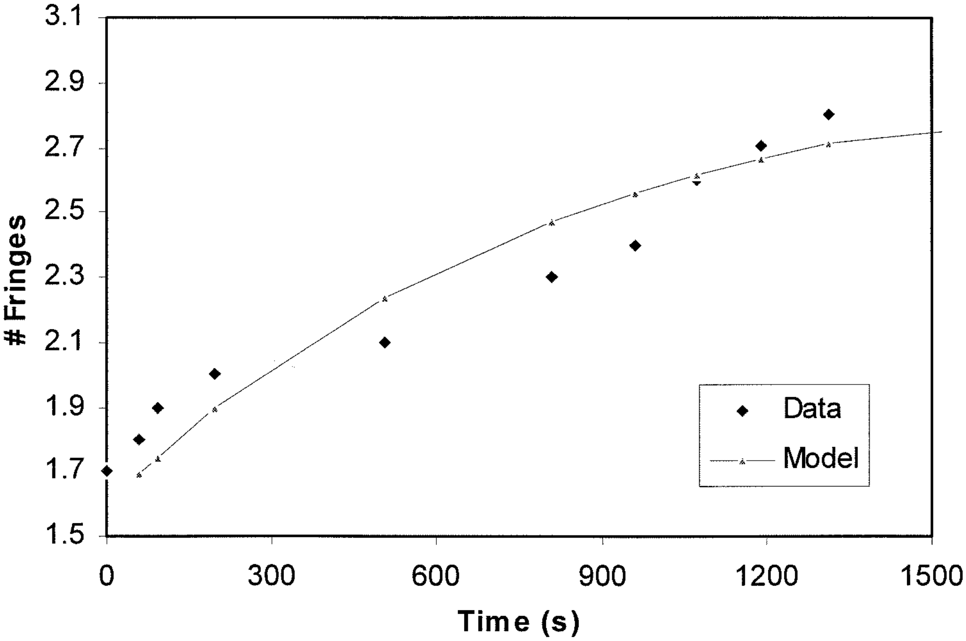

Figure D.18: Initial deoxidation of 700nm film at 585°C.

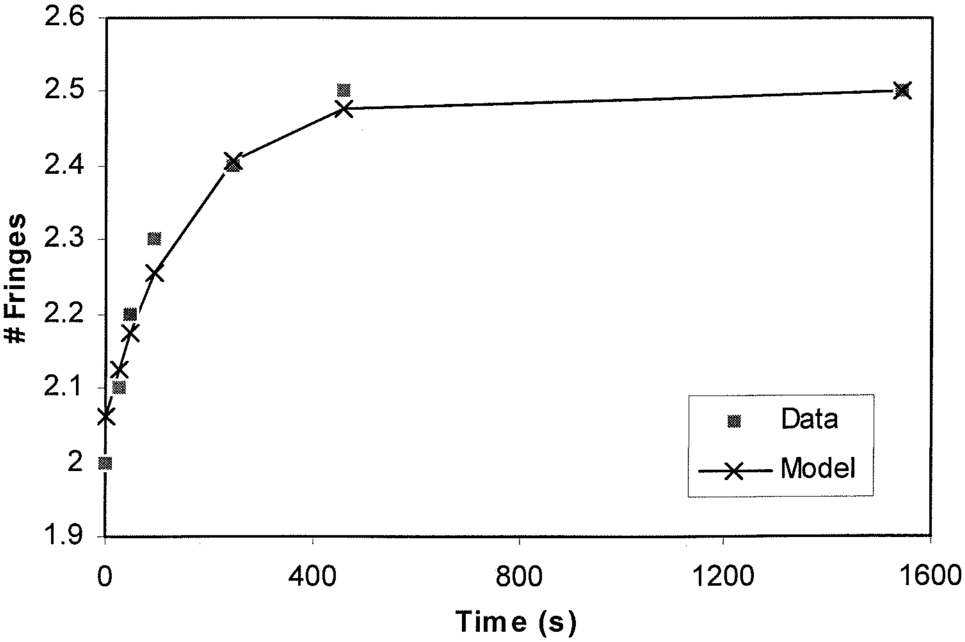

Figure D.19: Second deoxidation of 700nm film at 585°C.

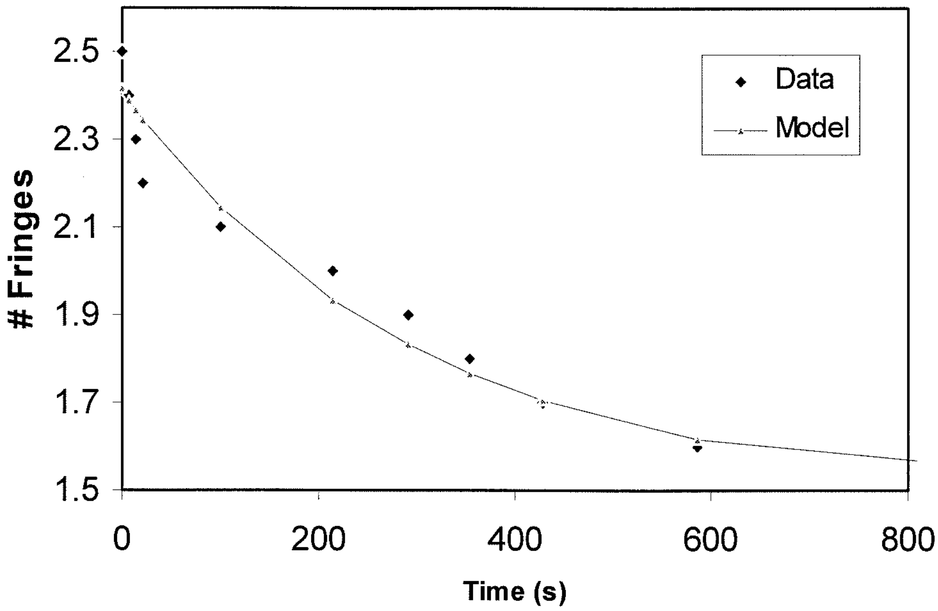

Figure D.20: Initial oxidation of 700nm film at 590°C.

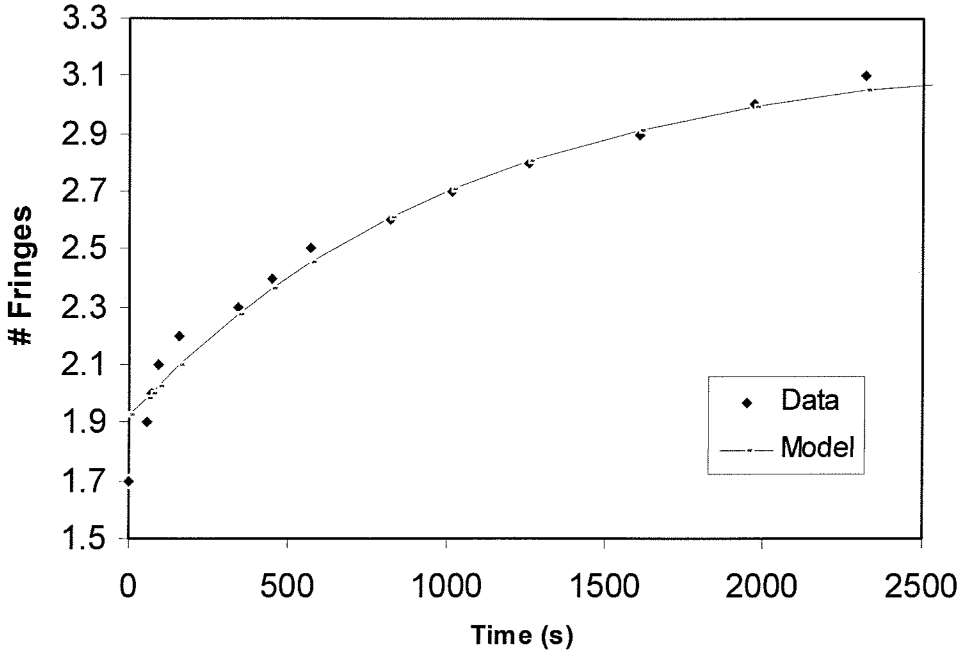

Figure D.21: Initial deoxidation of 700nm film at 590°C.

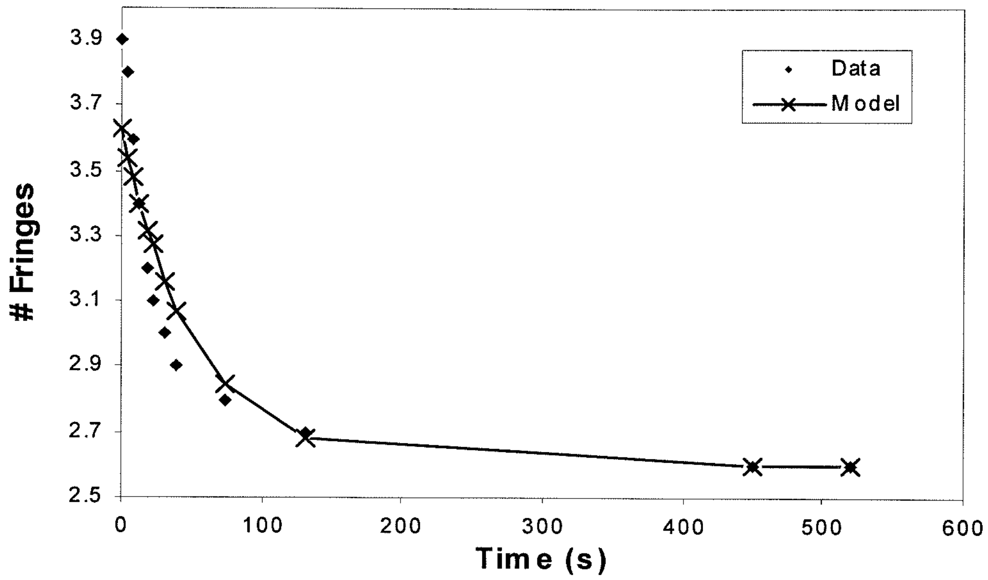

Figure D.22: Initial oxidation of 700nm film at 640°C.

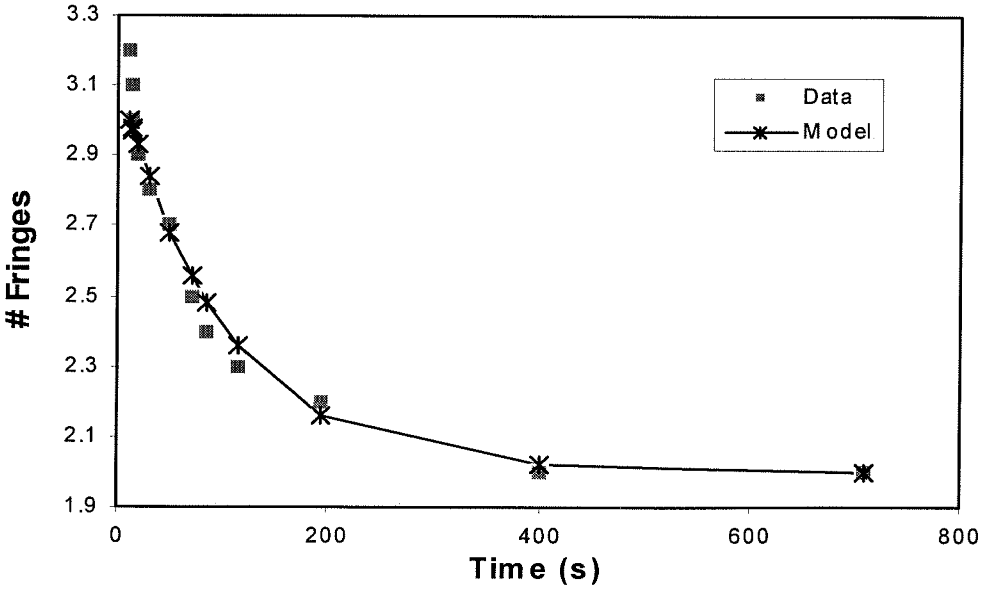

Figure D.23: Second oxidation of 700nm film at 640°C.

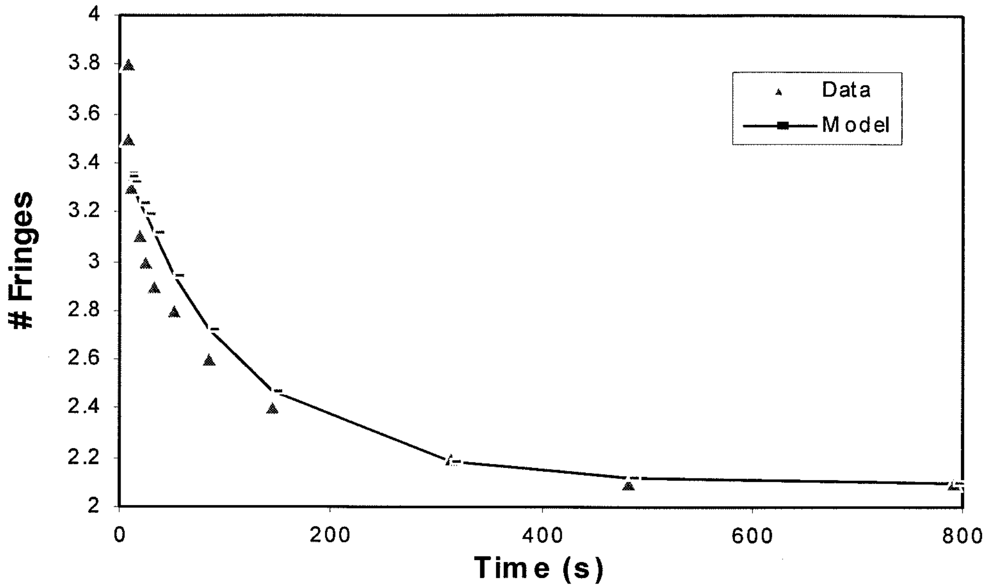

Figure D.24: Third oxidation of 700nm film at 640°C.

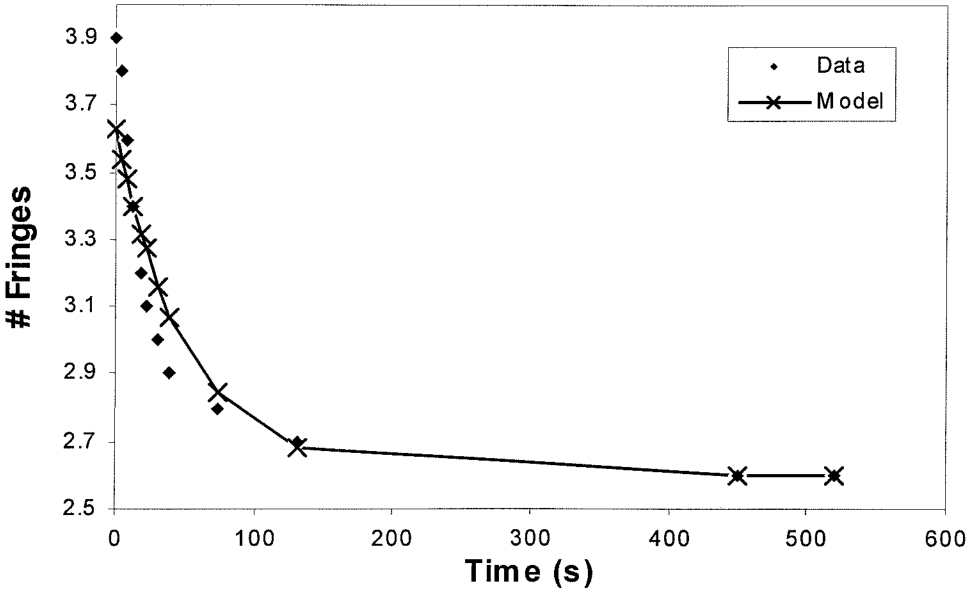

Figure D.25: Initial deoxidation of 700nm film at 640°C.

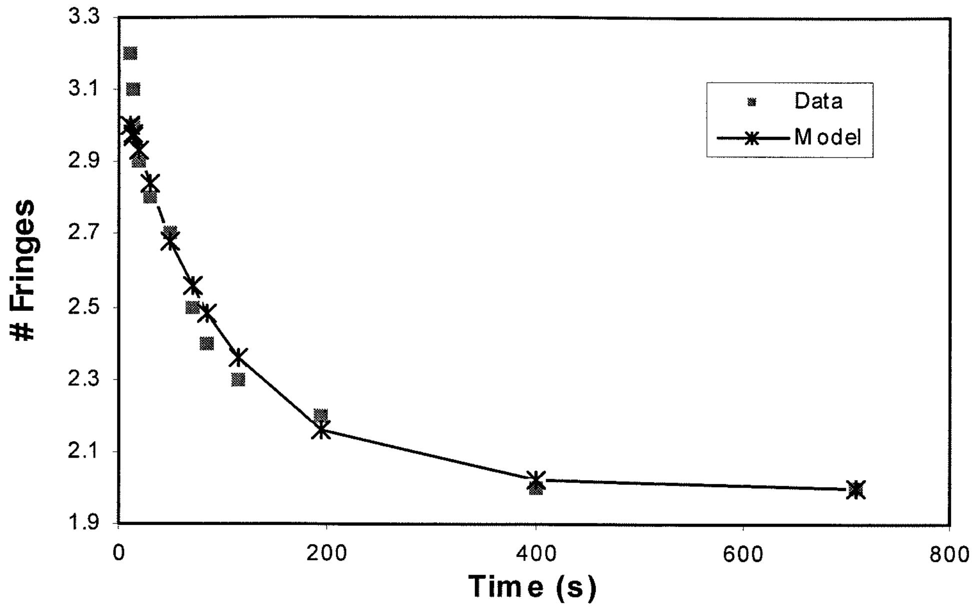

Figure D.26: Second deoxidation of 700nm film at 640°C.

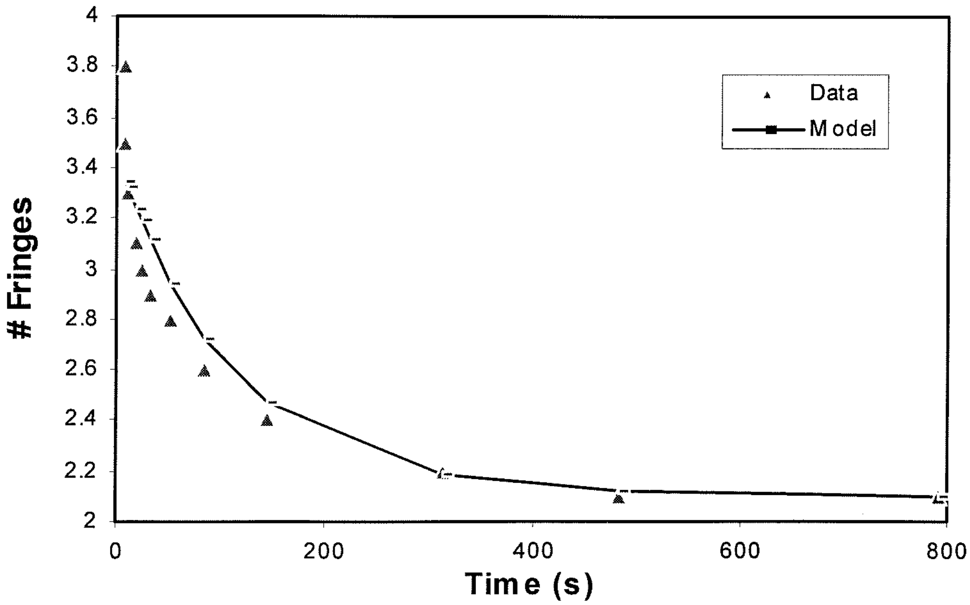

Figure D.27: Third deoxidation of 700nm film at 640°C.